MODELING THE EVOLVING MIXTURE OF H- AND J-AGGREGATES DURING ORGANIC FILM FORMATION

by

MORGAN L. SOSA

A DISSERTATION

Presented to the Department of Chemistry and Biochemistry
and the Graduate School of the University of Oregon
in partial fulfillment of the requirements
for the degree of
Doctor of Philosophy

March 2021

DISSERTATION APPROVAL PAGE

Student: Morgan L. Sosa

Title: Modeling the Evolving Mixture of H- and J-Aggregates During Organic Film Formation

This dissertation has been accepted and approved in partial fulfillment of the requirements for the Doctor of Philosophy degree in the Department of Chemistry and Biochemistry by:

Mark C. Lonergan	Chairperson
Cathy Y. Wong	Advisor
Jeffrey A. Cina	Core Member
Michael G. Raymer	Institutional Representative

and

Kate Mondloch	Interim Vice Provost and Dean of the Graduate School

Original approval signatures are on file with the University of Oregon Graduate School.

Degree awarded March 2021

DISSERTATION ABSTRACT

Morgan L. Sosa

Doctor of Philosophy

Department of Chemistry and Biochemistry

March 2021

Title: Modeling the Evolving Mixture of H- and J-Aggregates During Organic Film Formation

Understanding of aggregation in organic semiconducting (OSC) molecules is crucial to ensure desirable interactions in optoelectronics. Weak intermolecular forces driving aggregation can greatly impact the physical and electronic structures, making these materials useful in many applications. Ex situ techniques allow precursor solutions and complete films to be examined but are often unable to give insight into how structural or electronic properties evolve during aggregation. Theoretical models have often been used to explain how physical and spectral characteristics are linked. This dissertation aims to provide a computationally inexpensive method to model the absorption spectra of a mixture of organic molecular aggregates to provide a better understanding of the process of thin film formation and give insight to the evolving physical and electronic properties.

This method aims to be fast enough that spectra collected during thin film formation can be analyzed using a typical desktop computer and determine possible aggregate structures. Spectral metrics are used to drastically reduce the computational time required to compare simulated and experimental spectra. This is achieved by discarding simulated spectra that have peak intensity ratios that would not model the

experimental spectrum. Spectral metrics also reduces computational time required to compare the experimental and simulated spectra by reducing the total number of energy and intensity comparisons by two orders of magnitude. These two methods reduce the total computational time by over 99% when compared to using a brute force method.

The system investigated to demonstrate this technique is a well-studied OSC, pseudoisocyanine (PIC). Although typically thought to be a J-aggregate, we find that the absorption spectrum of PIC cannot be adequately modelled using solely J-aggregates either during molecular aggregation or in the final dry film. Additionally, this dissertation disputes a common assumption that the Huang-Rhys factor of a monomer can be used in simulations of aggregate absorption spectra. The method introduced here could be adopted to simulate the aggregation of other OSCs and can complement other structural characterization and computational techniques to provide feedback for rational design of structural and photophysical properties of OSC materials.

This dissertation includes previously published material.

CURRICULUM VITAE

NAME OF AUTHOR: Morgan L. Sosa

GRADUATE AND UNDERGRADUATE SCHOOLS ATTENDED:

University of Oregon, Eugene
University of Washington, Seattle

DEGREES AWARDED:

Doctor of Philosophy, Chemistry, 2021, University of Oregon
Bachelor of Science, Chemistry and Physics, 2015, University of Washington

AREAS OF SPECIAL INTEREST:

Molecular Aggregates
Molecular Simulations
Spectroscopy

PROFESSIONAL EXPERIENCE:

Graduate Teaching Assistant, University of Oregon, 2015-present

GRANTS, AWARDS, AND HONORS:

Exploratory Allocation Award, NERSC, 2018-2019

Graduate Student Travel Award for Excellence in the Teaching of Chemistry, University of Oregon, 2016

PUBLICATIONS:

Sosa, M. L.; Wong, C. Y. Revealing the Evolving Mixture of Molecular Aggregates during Organic Film Formation Using Simulations of *in Situ* Absorbance. *J. Chem. Phys.* **2020**, *153* (21), 214902. https://doi.org/10.1063/5.0020788.

Wilson, K. S.; Sosa, M. L.; Scott, M. N.; Wong, C. Y. In Situ Measurement of the Excited State Dynamics of Evolving Materials Systems. In *OSA Advanced*

Photonics Congress (AP) 2019 (IPR, Networks, NOMA, SPPCom, PVLED); OSA: Burlingame, California, 2019; p NoT1B.4. https://doi.org/10.1364/NOMA.2019.NoT1B.4.

Wilson, K. S.; Wong, C. Y.; Sosa, M. L.; Pandit, R. B. Composition of Molecular Aggregates during Film Formation Revealed Using Simulated Absorption Spectra. In *Physical Chemistry of Semiconductor Materials and Interfaces XVII*; Bronstein, H. A., Deschler, F., Eds.; SPIE: San Diego, United States, 2018; p 2. https://doi.org/10.1117/12.2322047.

CONFERENCE PRESENTATIONS:

M. L. Sosa and C. Y. Wong, "Tracking aggregate composition using absorption spectroscopy and a grid-based fitting algorithm," American Chemical Society 74th Northwest Regional Meeting, Portland, OR, 2019. Oral.

M. L. Sosa and C. Y. Wong, "Modeling molecular aggregation during thin film formation via in situ absorbance spectra", American Chemical Society 73rd Northwest Regional Meeting, Richland, WA, 2018. Oral.

M. L. Sosa and C. Y. Wong, "Modeling molecular aggregation during thin film formation via in situ absorbance spectra", 77th annual Oregon Academy of Science meeting, Newberg, OR, 2018. Oral.

M. L. Sosa, K. S. Wilson, and C. Y. Wong, "Development of Single-Shot Transient Absorption Spectroscopy to Measure Exciton Dynamics in Self-Assemble Conjugated Polymers", Energy and Sustainable Materials Symposium, Eugene, OR, 2016.

M. L. Sosa, K. S. Wilson, and C. Y. Wong, "Development of Single-Shot Transient Absorption Spectroscopy to Measure Exciton Dynamics in Self-Assemble Conjugated Polymers", Optical Molecular & Quantum Fall Symposium, Eugene, OR, 2016. Poster.

M. L. Sosa, K. S. Wilson, J. C. Sadighian, S. W. Reul, and C. Y. Wong, "Development of Single-Shot Transient Absorption Spectroscopy to Measure Exciton Dynamics in Self-Assemble Conjugated Polymers", Pacific Northwest Women in Science Retreat, Rockaway Beach, OR, 2016. Poster.

ACKNOWLEDGMENTS

First, I would like to thank my supervisor, Cathy Wong, for her continual encouragement and tough love. Cathy is fully invested in the success of her students, both in the lab and in real life. While I was always suspicious of her encouragement and praise, the reaffirmations reminded me that I did belong here and that I am capable of completing this whole process. Cathy is a genuinely caring person that I believe will continue to be compassionate to her students well into the future.

My lab mates and I had the unique experience of joining Cathy's new lab. They have been a constant in my life over the last 6 years, and I am incredibly grateful for their support and camaraderie. To the graduate student members of the group, Kelly, James, Chad Michael, and Zach, thank you for always providing a fun and welcoming workspace, and for lending an ear when I was getting yet another Matlab error. To all the undergrads and rotation students that have come through the Wong lab, you made a lasting impact on everyone around you. Rima Pandit was indispensable in this work, and her unbridled joy in everything science reminded me of the joy I have had learning about science. I want to especially thank James for being a fountain of encouragement when things would get hard. I would not be here without you.

A large portion of my time in graduate school was spent involved in the graduate student union, the Graduate Teaching Fellow Federation (GTFF AFT 3544). During that time, I served as a member of the bargaining committee when the administration was hellbent on destroying the premium health insurance coverage the GTFF has fought for over the years. I want to thank Mike Magee, Ellen Kress, Youssef Benasser, Trevor Brunnenmeyer, Curtis Dlouhy, Michelle Dreiling, Alexis Kiessling, Andy Labuza, Haley

Laningham, Pearl Lee, Alberto Lioy, Rita Ludwig, Michael Marchman, Adam Morse, Juan Ospina, Hannah Pell, Larissa Petrucci, Kyle Raze, and Sarah Stach. 4/4/4 hail Satan.

Graduate school would not have been possible without the support from my partner, Chris. He moved with me, sight unseen, with our pets Mimi and Mitzi in tow. He has been infinitely patient during the rollercoaster that is graduate school. His encouragement and assurance that everything will work out has made the future seem more exciting than scary. Additionally, I want to thank Dr. Alexis Kiessling for being an amazing friend and roommate. I hope we managed to keep each other sane throughout all this.

Finally, I would like to thank my dad, Chuck, and my sister, Taylor, for always being there for me and believing in me. You are the most kindhearted and caring people I know. I hope that I will be able to support and encourage you as you have with me. This material is based upon work supported by the National Science Foundation under Grant No. 1752129. Acknowledgement is made to the Donors of the American Chemical Society Petroleum Research Fund for partial support of this research.

This work is dedicated to Taylor Sosa, who has always been in my corner.

TABLE OF CONTENTS

LIST OF FIGURES

Figure Page

CHAPTER I

INTRODUCTION

Semiconductors are materials that have a conductivity between that of an insulator (e.g. glass) and a conductor (e.g. many metals). Typically, solid-state inorganic semiconductors are well-structured lattices of atoms, such as silicon or gallium arsenide, which are often intermixed with small amounts of another material to generate additional charged species in the lattice. The excess charges are then moved through the material with the help of an applied voltage, allowing those charges to be used in an electronic process.[1] Unlike their inorganic cousins, semiconducting organic molecules typically owe their semiconducting properties to extended conjugation[2–5] or through substantive overlap between the π-orbitals of adjacent molecules.[5–8] Excess charges can be injected through an applied current[9] or generated through a photoexcitation,[10] a process where an incident photon can generate an electron-hole pair, or exciton. Additionally, OSCs are solution processable and could provide an inexpensive alternative to traditional inorganic semiconductors that require large deposition chambers to grow well-ordered lattices.

Semiconducting materials play an integral role in modern life. The advent of the field-effect transistor (FET) essentially created the field of electronics by allowing solid-state materials to be used to amplify and rectify the current from the movement of electrons.[11] Typically, the semiconducting layer in FETs require high charge carrier mobility (> 1 cm^2/Vs) which has been achieved in both single-crystal and polycrystalline organic molecules.[5,12–15] OSCs have also been studied for use as the active layer in photovoltaic devices. Such active layers require the photogeneration of an exciton that separates into an electron and hole at the interface between an electron- and hole-

conducting material.[16,17] In such applications, the exciton must have a long enough lifetime and be mobile enough to reach an interface before dissipating the excitation through heat or light. Conversely, light-emitting diodes require active layers that encourage radiative recombination of excited electrons and holes through a highly fluorescent molecule or aggregate.[18–20] More exotic applications of OSCs include the developing field of spintronics[21,22] which hopes to take advantage of spin of long-lived charged species to expand on modern electronics, as well as a number of non-linear optical processes.[23–25] Each of these applications require different macroscale properties that are ultimately governed by very weak intermolecular forces. Understanding how aggregates are formed during deposition could inform researchers and engineers to pathways that result in favorable structures for a given application.

One of the major advantages OSCs have over their inorganic counterparts is the ability to be solution processable. Inorganic semiconductors typically use large pressure-controlled chambers with inert gasses and high temperatures to deposit a vapor of precursor materials onto a substrate.[26] More crystalline materials (e.g. crystalline silicon) must be grown as a single large crystal to ensure minimal structural defects.[27] Both of these techniques are difficult and expensive to scale up and require highly-specialized equipment and clean rooms to operate. While OSCs can be deposited through a vaporization process like their inorganic cousins, the more attractive method is solution deposition. In this method, molecules are dissolved in a solvent and that solution is deposited onto a substrate. After the solvent evaporates, the semiconducting molecules are, ideally, usable for a desired application. A variety of solution deposition techniques exist, each with their own advantages and disadvantages. Solution deposition techniques

can be roughly broken down into four categories: dropcasting, spincoating, printing, and meniscus-guided.[28] Dropcasting is the simplest technique, where a solution is dropped onto a substrate and evaporation of the solvent causes the molecules to aggregate together. Unless the molecules are naturally prone to forming highly ordered structures, the results of dropcasting are often amorphous. While this is the simplest deposition technique, dropcast films can be difficult to reproduce. Spincoating is similar to dropcasting, but once the solution has been deposited, the substrate is rapidly spun to remove the majority of the solvent and dissolved molecules. As a result, the film tends to dry quickly and make reproducible amorphous or radially distributed films. While spincoating is often used in research laboratories, it is very wasteful in terms of precursor materials and cannot be scaled up to account for industrial needs. Deposition through printing is analogous to ink or toner printing used on paper. The solution is deposited onto the substrate with a brush, through an inkjet or sprayer, or with a stamp. These methods allow molecules to be deposited with substantively less solvent, and in some cases can encourage directional growth of aggregates.[29] Depending on the deposition method (stamping, ink jet, etc.) a high level of directional control can be achieved. For example, brush painting and stamping have no air-liquid interface and allow for precise control of directionality through sheer forces and patterning.[30,31] Since directional structures are often advantageous in OSC devices, a variety of directional meniscus-guided deposition techniques can also be used. In these techniques, the substrate moves under the deposition device and the solution is deposited across the surface of the substrate, in the same way one might butter a piece of bread.[32] Unlike printing techniques which use some active process of depositing the solution, meniscus-guided deposition

uses capillary action to passively draw out the solution. Additionally, the thickness and concentration of the resulting film can be controlled simply by increasing or decreasing the speed at which the substrate or deposition device moves. Despite the advantages and scalability of printing and meniscus-assisted deposition methods, a large amount of optimization must be done to achieve high-performing devices, such as finding ideal solvent systems and accounting for fluid dynamics on the substrate.[33,34] While some directional methods do exist for depositing OSCs, the resulting structures can be quite heterogeneous, resulting in poor device performance. As a result, it is important to understand how mixtures of aggregates form during deposition to potentially control against unfavorable structures.

Understanding the evolving physical structures present during thin film formation will also give insight to the evolving electronic structure and, as a result, possible device properties. One of the earliest theories for explaining how electronic and spectral characteristics are impacted by physical structure was introduced by Kasha[35–37] in the 1950s. In Kasha's work, molecules are described relative to their transition dipole moments (TDM). When two molecules couple together energy splitting can occur, as shown in Eq. 1.1, where J_{12} is the dipole-dipole coupling due to the interactions between molecules 1 and 2, $\vec{\mu}$ is the TDM of a given molecule, $\hat{r}_{12}$ is the unit vector going from molecule 1 to molecule 2, and r_{12} is the distance between the two molecules.

$$J_{12} = C\frac{\vec{\mu}_1 \cdot \vec{\mu}_2 - 3(\vec{\mu}_1 \cdot \hat{r}_{12})(\vec{\mu}_2 \cdot \hat{r}_{12})}{r_{12}^3} \tag{1.1}$$

The presence of this coupling results in a splitting of the energy states, with one state higher in energy than each molecule alone and one state lower in energy. The

magnitude and sign of the coupling and the magnitude of the splitting depend on the orientation of the two TDMs, with parallel TDMs resulting in maximal splitting. The higher energy state corresponds to when the TDMs are out-of-phase, while the lower energy state corresponds to the TDMs being in-phase. If the TDMs are parallel and colinear the coupling is negative and the in-phase state is bright, due to having a non-zero net dipole, whereas the out-of-phase state has a net-zero dipole and is dark. As a result, such aggregates will have a red-shifted absorption peak and will be highly fluorescent. Conversely, if the TDMs are parallel but both perpendicular to the intermolecular separation vector, the coupling is positive and the in-phase state has a net-zero dipole and is dark, whereas the out-of-phase state has a non-zero net dipole and is bright. The spectral features of these aggregates are essentially opposite of the parallel and colinear aggregates, as the higher energy bright state result in a blue-shifted absorption peak compared to the monomer. As fluorescence often occurs from the lowest energy state,[38] these aggregates have suppressed fluorescence. The two types of aggregates are referred to as J- and H-aggregates, respectively. This theory has since been expanded to include nuances such as vibrational coupling,[39–41] charge transfer,[42–45] and aggregation in multiple direction,[46–48] further complicating the relationship between physical and electronic structure. While there is robust literature addressing the correlation between physical and electronic properties, the evolution of these properties during film formation is poorly understood. This dissertation aims to provide a computational method for studying the process of aggregation that allows mixtures of aggregates to be considered.

Several techniques exist that can either directly or indirectly probe aggregate structure. One of the most ubiquitous techniques for directly determining structure is

microscopy. By using electrons instead of photons, scanning electron microscopy[49] (SEM) and tunneling electron microscopy[50] (TEM) can bypass the diffraction limit of light and resolve structures that are on the scale of nanometers and picometers. While SEM can only provide information about the surface of a sample, TEM measures transmitted electrons and can give information about the internal structure of aggregates. Additionally, TEM can obtain a higher resolution than SEM, on the order of 0.5 nm compared to 10s of pm in SEM. Even though these are very precise techniques for determining structure, each of these microscopies have their own requirements with regards to sample preparation and conditions needed for measurements. In SEM, measurements are typically performed under vacuum which require the sample to be completely dry. Samples in TEM must be very thin, to allow the electrons to travel through the material. Both SEM and TEM collect a single image on the order of minutes. SEM and TEM are often used to characterize molecular aggregates, such as those seen in cyanine dyes.[51,52] Both of these techniques have been used for in situ measurements,[53–55] though these typically require highly specialized sample preparation.

Atomic force microscopy[56,57] (AFM) can also bypass the diffraction limit of light by scanning an atomically sharp tip over a surface and using a laser to measure its deflection. This can be used to measure aggregate structures. AFM can resolve lateral structures on the order of 10s of nm and vertical structures on the order of 0.1 nm. Single strands and semicrystalline domains of a prototypical semiconducting polymer, P3HT, deposited on a hexagonal lattice have been resolved with AFM.[58] A typical AFM image takes 5-10 minutes to collect, though a typical experiment that collects several images can take 1-2 hours.

X-ray diffraction[2,59,60] (XRD) is a technique that uses x-rays to probe structure, though in a less direct way than TEM, SEM, or AFM. X-rays are shot at an angle towards a sample, at which point the x-rays can collide with atoms or molecules and the resulting diffraction can give information about the spacing and orientation of well-ordered structures in the sample. Powder XRD is often used to characterize crystalline organic materials, though thin film geometries typically require a grazing-incident geometry.[59] In grazing-incident x-ray scattering (GIXS), x-rays are incident to the sample at shallow angles (< 1°) and is typically used for thin film geometries. This technique measures the scatter due to molecular packing, and is characterized by whether the probed diffraction angle is small (< 1°) as in the case in grazing-incident small-angle x-ray scattering (GISAXS), or wide (~1° - 45°) as in the case in grazing-incident wide-angle x-ray scattering (GIWAXS). Both techniques can also be performed during deposition of a thin film.[61] For example, in situ GISAXS has been used to measure the change in crystallinity during zone casting of block co-polymers,[62] and in situ GIWAXS measurements have helped reveal multiple crystallization pathways in the polymer PTB7.[63] In order to achieve good signal to noise in thin film samples, specialized x-ray beam lines are required. The high intensity also allows for data collection on the order of seconds.[64] As a result, these instruments are often expensive or require travel and scheduling time at a beam line facility.

Visible light can also be used, indirectly, to probe structure. As mentioned above, the electronic structure of aggregates is different than that of a single molecule. Linear absorption and fluorescence spectroscopy probe the long-lived excited states of a sample and can often provide information that is dependent on structure, such as electronic

coupling and relative orientation of molecules in aggregates. Additionally, both techniques are relatively inexpensive and can be performed during solution deposition using typical conditions. Depending on the molecule, aggregation can occur on the time scale of seconds to hours. In order to collect in situ measurements during aggregation, measurements should be completed fast enough to resolve the changing structure.

A well-studied small organic molecule, TIPS-pentacene, has exhibited a change in the absorption spectrum upon aggregation during spincoating deposition, as well as an aggregate dependent photoluminescence.[65] Time-resolved spectroscopic techniques, such as transient absorption (TA) and time-resolved photoluminescence (TRPL), can be used to measure changes in excited state populations. Both techniques provide signals as a function of time after excitation and give information about excitation and relaxation pathways. These techniques can be incredibly useful for measuring charge transfer and charge recombination, and can be used to infer aggregate structure.[66,67] For example, different aggregate forms of perylene were investigated using TA, and it was shown that relaxation pathways depend on the structure of the aggregates.[66] While TA and TRPL are incredibly useful for steady-state samples, such as a solution or a formed thin film, the time required to perform these measurements have made in situ measurements impossible. Single-shot transient absorption could be used to overcome this barrier, though these instruments are custom built by researchers and highly specialized.[68] Computational methods can give theoretical insight into how molecules behave during aggregation. Atomistic molecular dynamics (MD) simulations can give information about stability of aggregates but cannot give real-time information on the scale of seconds, when aggregation often occurs.[69] Behavior at longer time scales can be probed by using

coarse-grained MD simulations, which approximates molecules or sections of molecules as a single bead. Doing this allows simulations to be run for longer, but fine atomistic detail is lost.[70,71] Calculations using quantum mechanical formalism can be used to approximate physical characteristics of molecules and aggregates, such as vibrational structure, electronic structure, and electronic spectra. Depending on the level of theory and the kind of approximations made, these kinds of calculations can be prohibitively computationally expensive and may require the use of expensive computing clusters. In the next couple of sections, I will provide an introduction to the computationally inexpensive method used to model absorption spectra. Additionally, I will introduce the molecule used to demonstrate this method, pseudoisocyanine.

The Holstein Hamiltonian often used to calculate spectra of aggregates was initially developed by Holstein to explain polarons (lattice distortions caused by the presence of a charge).[72] While Holstein's theory was specifically for 1-D molecular crystals, it was quickly expanded upon to account for excitations in molecular dimers,[40,73,74] and then to arbitrarily large aggregates.[75] During this time, researchers also developed theoretical frameworks to explain how intermolecular charge transfer impacted photophysical behavior and electronic spectra.[42] The use of a multiparticle basis set was later introduced, which limits the number of interactions that need to be considered in a Hamiltonian, when compared to considering excitations on every chromophore and interactions between every pair of chromophores. For example, the two-particle approximation assumes that the excited state of the aggregate can be approximated as a linear combination of basis states where only two of the chromophores are excited. Out of all the chromophores in the aggregate, one chromophore can be both

electronically and vibrationally excited and another chromophore can carry additional vibrational excitations. These two excited chromophores are "particles" in the two-particle approximation. Considering basis states where additional vibrational excitation can exist on only one other chromophore decreases the total number of basis states that need to be considered, and yet it has been shown to accurately model the spectra of molecules with electronic couplings typical of organic systems.[39] Several aggregate geometries have been considered using a Holstein-like Hamiltonian, and this type of model has been used to explain the experimental spectra of small molecule,[46,76–79] polymer,[47,80] and oligomer[81,82] aggregates. The primary way this dissertation expands on previous work is by presenting a new methodology for quickly simulating the absorption spectra of aggregates. Only key vibronic peaks and their relative intensities and positions are considered, which reduces the time needed to compare simulated and experimental spectra. This kind of analysis could work especially well for molecules that have distinct vibronic peaks, such as cyanine dyes, phthalocyanines,[83] rubrene,[84] distyrylbenzenes,[85] pentacenes,[86] and perylene diimides.[87–89] While not addressed in this dissertation, a similar analysis could be performed using photoluminescence spectra, which typically have well-defined peaks.

Cyanines are a group of molecules that have a conjugated backbone with nitrogen containing groups on both ends of the backbone. They can be further classified based on if the nitrogen containing group is cyclic or not.[90] These molecules have historically been used in photography,[91] but current interest has shifted to using cyanines as fluorescent probes in biological systems,[92] as efficient light absorbers for use in dye-sensitized solar cells,[93] and as photoswitches.[94] Like other conjugated molecules, the energy of absorption

and emission of cyanines can be tuned by increasing the length of the backbone with vinylene groups, with a longer backbone corresponding to redder spectral features. Due to their rigid backbone, cyanines have been shown to form a large number of different well-ordered structures,[95–97] some of which are dependent on solution conditions.[98] Additionally, their high absorptivity and tunable absorption and emission wavelength makes cyanines useful in Förster resonance energy transfer (FRET) applications as either absorbers[99] or emitters.[100]

The specific cyanine dye used in this dissertation, pseudoisocyanine (PIC), has had a large impact on the study of molecular aggregation. PIC exhibits a substantial red-shift in the main absorption peak and an increase in fluorescence intensity upon aggregation, first shown by Jelley.[101] The aggregates that cause these spectral changes are referred to as J-aggregates . As a result of these spectral observations, researchers sought to explain the effects aggregation has on electronic structure and energy transfer. Several methods have been used to examine the structure of aggregates of PIC, though there is currently no consensus. Theoretical work by Kopainsky[102,103] suggests dimers are the first species to form during aggregation, with the two molecules stacked face-to-face with an offset between them. Experimental work using transient absorption spectroscopy by Kopainsky[103] was performed on larger aggregates as well, and showed that when aggregates were excited in the blue-region of the absorption spectrum, emission was measured at energies attributed to the J-aggregate. Absorption in the blue-region is thought to be attributed to H-aggregates, which suggests there are multiple aggregate species present. Theoretical work done by Scherer and Fischer[104] suggests that the experimental spectrum of PIC can be explained if one were to consider an aggregate that

had two molecules per unit cell. Using a Holstein-like Hamiltonian, they were able to reproduce the spectral features seen in PIC aggregates, as well as the polarization dependence of the spectrum. Physical observations of PIC aggregates were later done using TEM, [105] suggesting tubular aggregates that were ~3000 molecules long. Based on the width of the aggregate fibers, it was suggested that the fibers were composed of six bundles of dimers with a structure similar to that proposed by Kopainsky. Distinct aggregates of PIC have also been formed using concentrated solutions and temperatures below freezing.[106] Using fluorescence excitation measurements, Fidder observed two different aggregates species, referred to as the red site and the blue site. The red site resulted in two peaks in the fluorescence excitation spectrum, with the redder peak being more intense. The same two peaks were also seen in the blue site, though the bluer peak was more intense. The presence of both peaks in both sites and the change in relative intensity suggests there are two different aggregate species that could be present in a single larger aggregate. Fidder suggests an aggregate structure with four molecules per unit cell, contrary to the structure suggested by Scherer and Fischer which has two molecules per unit cell. Molecular dynamics simulations and density functional theory (DFT) calculations have also been used to probe the structure of PIC. The stability of several dimer structures were simulated[69] and found to be unstable under simulation conditions. Instead of the manifestation of a J-aggregate, simulations suggested a "stack of coins" aggregation. Self-assembly was also investigated, with molecules often forming micelles or nanotubes, with the hydrophobic chains on the inside of the structures.[107] The absorption spectra of many linear, chiral tubes, and crystal structures have been calculated using DFT,[108] though like the molecular dynamics simulations, the structures

investigated were unable to reproduce the experimental spectrum. With advances in computation power, it is becoming apparent that more research needs to be done to determine the pathways by which aggregates can form and the types of aggregates that can result from different aggregation conditions.

This dissertation will present my work developing and implementing a computationally inexpensive method for modeling in situ experimental absorption spectra as a mixture of aggregates. In Chapter 2, the mathematical theory for simulating absorption spectra will be presented. This chapter includes published co-authored material with Cathy Y. Wong. Chapter 3 outlines how the parameter space for simulated spectra can be thoroughly sampled with minimal computational costs. This technique is verified using PIC, which, while well-studied, has an unclear aggregate structure. Analysis of the modeling of these spectra shows that the Huang-Rhys factor of a monomer should not be used when modeling molecular aggregation, as is common practice in the literature. This chapter includes published co-authored material with Cathy Y. Wong.

CHAPTER II

IMPLEMENTATION OF HOLSTEIN HAMILTONIAN AND CALCULATION OF ABSORPTION SPECTRA

Typically, scientific literature describes quantum mechanical calculations using general equations that can be difficult to parse for the reader. The goal of this chapter is to introduce the general method used to simulate spectra and to give more detail behind the specific calculations so they can easily be implemented using a variety of programming languages. First, I will introduce the Hamiltonian, basis states, and the approximations used in these calculations. Next, several examples will be given of how to generate the matrix elements of the Hamiltonian and of what a constructed Hamiltonian looks like. Some examples of the effect of each parameter in the Hamiltonian on the simulated spectra will also be shown. Finally, a procedure for quickly comparing the experimental and simulated spectra that can be used for fitting will be outlined. Overall, this chapter aims to walk through the more technical details of implementing a Hamiltonian and generating spectra.

2.1 – Holstein Hamiltonian

The Hamiltonian for a single chromophore can be described by the energy of the electronic transition (ε_0), the energy of the main vibrational mode (ω_0), and the Huang-Rhys factor (λ^2) which is related to the nuclear reorganization energy, as shown in Eq. 2.1. The operators a and $a^\dagger$ (b and $b^\dagger$) are the annihilation and creation operators for electronic (vibrational) quantum.

$$\hat{H} = \varepsilon_0 a^\dagger a + \omega_0 b^\dagger b + \omega_0 a^\dagger a \left[\lambda (b^\dagger + b) + \lambda^2 \right] \tag{2.1}$$

The basis states for the monomer, $\left|\psi^{(\alpha)}\right\rangle$, are defined by having n electronic quanta and v vibrational quanta, as shown in Eq. 2.2. In the following three equations, $c^{(\alpha)}$ is a normalization factor, and the basis states form a complete and orthonormal set.

$$\left|\psi^{(\alpha)}\right\rangle = \sum_{n,v} c_{n,v}^{(\alpha)} \left|n, v\right\rangle \tag{2.2}$$

For an arbitrarily long aggregate, the basis states can be expanded to potentially account for electronic and vibrational excitations on each molecule, as shown in Eq. 2.3. Here, n_q electronic quanta and v_q vibrational quanta can exist on molecule q.

$$\left|\psi^{(\alpha)}\right\rangle = \sum c_{n_1,v_1;\ldots n_q,v_q}^{(\alpha)} \left|n_1, v_1; n_2, v_2; \ldots; n_q, v_q\right\rangle \tag{2.3}$$

As will be shown in Section 2.2, the number of basis states substantially grow when accounting for excitations on additional molecules. To decrease computational time, basis states are limited in three ways. First, only a single electronic quantum can exist. Second, vibrational quanta are only allowed on two molecules. Third, the total number of vibrational quanta in the state must be less than or equal to v_{max}. The basis states therefore are defined by the location (n) and number of electronic and vibrational quanta (e,v) on one molecule and by the location (n') and number of vibrational quanta (v') on a second molecule, as shown in Eq. 2.4.

$$\left|\psi^{(\alpha)}\right\rangle = \sum_{n,e,v} \sum_{n',v'} c_{n,e,v;n',v'}^{(\alpha)} \left|n, e, v; n', v'\right\rangle \tag{2.4}$$

The Hamiltonian for an aggregate is similar to a monomer, but additionally accounts for electronic coupling between two molecules, shown in Eq. 2.5 as $J_{m,n}$. All other terms are as described for the monomer.

$$\hat{H} = \varepsilon_0 \sum_{n=1}^{N} a_n^\dagger a_n + \omega_0 \sum_{n=1}^{N} b_n^\dagger b_n + \sum_{n=1}^{N}\sum_{m\neq n}^{N} J_{m,n}(a_m^\dagger a_n + a_m a_n^\dagger) + \omega_0 \sum_{n=1}^{N} a_n^\dagger a_n \left[\lambda(b_n^\dagger + b_n) + \lambda^2\right] \tag{2.5}$$

2.2 – Populating Matrix Elements of the Hamiltonian

For a general operator $\hat{O}$, the matrix elements are defined based on the operator's interaction with a set of complete basis states, as shown in Eq. 2.6.

$$\hat{O}_{n,m} \equiv \langle \psi_n | \hat{O} | \psi_m \rangle \tag{2.6}$$

This definition allows the generation of a Hamiltonian that can be used computationally. The Hamiltonian for the monomer (Eq. 2.1) can be broken up into an electronic term ($\hat{H}_{el}$), a vibrational term ($\hat{H}_{vib}$), and a vibronic term ($\hat{H}_{el-vib}$). Below, we will consider each of these three components of the Hamiltonian in turn, using the basis states for the monomer. We will consider the electronic and vibrational ground state, and states with one electronic quantum and up to 2 vibrational quanta. All of the basis states are shown in Eq. 2.7, where $|\psi_1\rangle$ is the collection of all basis states for one molecule. The electronic term of the Hamiltonian is then represented by Eq. 2.8.

$$|\psi_1\rangle = \begin{bmatrix} |0,0\rangle \\ |1,0\rangle \\ |1,1\rangle \\ |1,2\rangle \end{bmatrix} \tag{2.7}$$

$$\langle \psi_1 | \hat{H}_{el} | \psi_1 \rangle = \varepsilon_0 \begin{bmatrix} \langle 0,0|a^\dagger a|0,0\rangle & \langle 0,0|a^\dagger a|1,0\rangle & \langle 0,0|a^\dagger a|1,1\rangle & \langle 0,0|a^\dagger a|1,2\rangle \\ \langle 1,0|a^\dagger a|0,0\rangle & \langle 1,0|a^\dagger a|1,0\rangle & \langle 1,0|a^\dagger a|1,1\rangle & \langle 1,0|a^\dagger a|1,2\rangle \\ \langle 1,1|a^\dagger a|0,0\rangle & \langle 1,1|a^\dagger a|1,0\rangle & \langle 1,1|a^\dagger a|1,1\rangle & \langle 1,1|a^\dagger a|1,2\rangle \\ \langle 1,2|a^\dagger a|0,0\rangle & \langle 1,2|a^\dagger a|1,0\rangle & \langle 1,2|a^\dagger a|1,1\rangle & \langle 1,2|a^\dagger a|1,2\rangle \end{bmatrix} \tag{2.8}$$

Individually, the creation and annihilation operators increase or decrease the number of quanta in each state, and shown in Eq. 2.9, where $\hat{o}^{\dagger}(\hat{o})$ is the creation (annihilation) operator and n is the number of quanta.

$$\begin{gathered} o^{\dagger}\left|n\right\rangle = \sqrt{n+1}\left|n+1\right\rangle \\ o\left|n\right\rangle = \sqrt{n}\left|n-1\right\rangle \\ o^{\dagger}o\left|n\right\rangle = n\left|n\right\rangle \end{gathered} \tag{2.9}$$

Applying the lowering operator to the ground state is 0. Using this relationship, the first two terms of the Hamiltonian, $\hat{H}_{el}$ and $\hat{H}_{vib}$, can be easily determined. Since the basis set is orthonormal and the operators $a^{\dagger}a$ and $b^{\dagger}b$ do not change the state they acted on, only diagonal terms have a possibility of being non-zero. Additionally, $a^{\dagger}a$ and $b^{\dagger}b$ only act on the electronic and vibrational quanta, respectively. The evaluation of each term in Eq. 2.8 is shown in Eq. 2.10.

$$\left\langle \psi_1 \middle| \hat{H}_{el} \middle| \psi_1 \right\rangle = \varepsilon_0 \begin{bmatrix} 0 & 0 & 0 & 0 \\ 0 & 1 & 0 & 0 \\ 0 & 0 & 1 & 0 \\ 0 & 0 & 0 & 1 \end{bmatrix} \tag{2.10}$$

The vibrational term of the Hamiltonian can be determined the same way, but now $b^{\dagger}b$ results in the number of vibrational quanta on each state (Eq. 2.11, Eq. 2.12).

$$\left\langle \psi_1 \middle| \hat{H}_{vib} \middle| \psi_1 \right\rangle = \omega_0 \begin{bmatrix} \left\langle 0,0 \middle| b^{\dagger}b \middle| 0,0 \right\rangle & \left\langle 0,0 \middle| b^{\dagger}b \middle| 1,0 \right\rangle & \left\langle 0,0 \middle| b^{\dagger}b \middle| 1,1 \right\rangle & \left\langle 0,0 \middle| b^{\dagger}b \middle| 1,2 \right\rangle \\ \left\langle 1,0 \middle| b^{\dagger}b \middle| 0,0 \right\rangle & \left\langle 1,0 \middle| b^{\dagger}b \middle| 1,0 \right\rangle & \left\langle 1,0 \middle| b^{\dagger}b \middle| 1,1 \right\rangle & \left\langle 1,0 \middle| b^{\dagger}b \middle| 1,2 \right\rangle \\ \left\langle 1,1 \middle| b^{\dagger}b \middle| 0,0 \right\rangle & \left\langle 1,1 \middle| b^{\dagger}b \middle| 1,0 \right\rangle & \left\langle 1,1 \middle| b^{\dagger}b \middle| 1,1 \right\rangle & \left\langle 1,1 \middle| b^{\dagger}b \middle| 1,2 \right\rangle \\ \left\langle 1,2 \middle| b^{\dagger}b \middle| 0,0 \right\rangle & \left\langle 1,2 \middle| b^{\dagger}b \middle| 1,0 \right\rangle & \left\langle 1,2 \middle| b^{\dagger}b \middle| 1,1 \right\rangle & \left\langle 1,2 \middle| b^{\dagger}b \middle| 1,2 \right\rangle \end{bmatrix} \tag{2.11}$$

$$\left\langle \psi_1 \middle| \hat{H}_{vib} \middle| \psi_1 \right\rangle = \omega_0 \begin{bmatrix} 0 & 0 & 0 & 0 \\ 0 & 0 & 0 & 0 \\ 0 & 0 & 1 & 0 \\ 0 & 0 & 0 & 2 \end{bmatrix} \tag{2.12}$$

The single creation and annihilation operators in the vibronic term of the Hamiltonian allow different states to be coupled together. A given matrix element for the vibronic term is given by Eq. 2.13, where $\langle m|$ and $|n\rangle$ are arbitrary basis states.

$$\begin{aligned}\langle m|\hat{H}_{el-vib}|n\rangle &= \langle m|\omega_0 a^\dagger a\left[\lambda\left(b^\dagger+b\right)+\lambda^2\right]|n\rangle \\ &= \langle m|\omega_0 a^\dagger a\lambda b^\dagger + \omega_0 a^\dagger a\lambda b + \omega_0 a^\dagger a\lambda^2|n\rangle\end{aligned} \tag{2.13}$$

The three terms can be further distributed for clarity. We can separately consider the term with the creation operator for vibrational quanta, ($\hat{H}_{el-vib-upper}$), annihilation operator for vibrational quanta, ($\hat{H}_{el-vib-lower}$), and a constant factor of λ^2, ($\hat{H}_{el-vib-con}$), as shown in Eq. 2.14-2.16.

$$\langle\psi_1|\hat{H}_{el-vib-upper}|\psi_1\rangle = \omega_0\begin{bmatrix}\langle 0,0|a^\dagger a\lambda b^\dagger|0,0\rangle & \langle 0,0|a^\dagger a\lambda b^\dagger|1,0\rangle & \langle 0,0|a^\dagger a\lambda b^\dagger|1,1\rangle & \langle 0,0|a^\dagger a\lambda b^\dagger|1,2\rangle \\ \langle 1,0|a^\dagger a\lambda b^\dagger|0,0\rangle & \langle 1,0|a^\dagger a\lambda b^\dagger|1,0\rangle & \langle 1,0|a^\dagger a\lambda b^\dagger|1,1\rangle & \langle 1,0|a^\dagger a\lambda b^\dagger|1,2\rangle \\ \langle 1,1|a^\dagger a\lambda b^\dagger|0,0\rangle & \langle 1,1|a^\dagger a\lambda b^\dagger|1,0\rangle & \langle 1,1|a^\dagger a\lambda b^\dagger|1,1\rangle & \langle 1,1|a^\dagger a\lambda b^\dagger|1,2\rangle \\ \langle 1,2|a^\dagger a\lambda b^\dagger|0,0\rangle & \langle 1,2|a^\dagger a\lambda b^\dagger|1,0\rangle & \langle 1,2|a^\dagger a\lambda b^\dagger|1,1\rangle & \langle 1,2|a^\dagger a\lambda b^\dagger|1,2\rangle\end{bmatrix} \tag{2.14}$$

$$\langle\psi_1|\hat{H}_{el-vib-lower}|\psi_1\rangle = \omega_0\begin{bmatrix}\langle 0,0|a^\dagger a\lambda b|0,0\rangle & \langle 0,0|a^\dagger a\lambda b|1,0\rangle & \langle 0,0|a^\dagger a\lambda b|1,1\rangle & \langle 0,0|a^\dagger a\lambda b|1,2\rangle \\ \langle 1,0|a^\dagger a\lambda b|0,0\rangle & \langle 1,0|a^\dagger a\lambda b|1,0\rangle & \langle 1,0|a^\dagger a\lambda b|1,1\rangle & \langle 1,0|a^\dagger a\lambda b|1,2\rangle \\ \langle 1,1|a^\dagger a\lambda b|0,0\rangle & \langle 1,1|a^\dagger a\lambda b|1,0\rangle & \langle 1,1|a^\dagger a\lambda b|1,1\rangle & \langle 1,1|a^\dagger a\lambda b|1,2\rangle \\ \langle 1,2|a^\dagger a\lambda b|0,0\rangle & \langle 1,2|a^\dagger a\lambda b|1,0\rangle & \langle 1,2|a^\dagger a\lambda b|1,1\rangle & \langle 1,2|a^\dagger a\lambda b|1,2\rangle\end{bmatrix} \tag{2.15}$$

$$\langle\psi_1|\hat{H}_{el-vib-con}|\psi_1\rangle = \omega_0\begin{bmatrix}\langle 0,0|a^\dagger a\lambda^2|0,0\rangle & \langle 0,0|a^\dagger a\lambda^2|1,0\rangle & \langle 0,0|a^\dagger a\lambda^2|1,1\rangle & \langle 0,0|a^\dagger a\lambda^2|1,2\rangle \\ \langle 1,0|a^\dagger a\lambda^2|0,0\rangle & \langle 1,0|a^\dagger a\lambda^2|1,0\rangle & \langle 1,0|a^\dagger a\lambda^2|1,1\rangle & \langle 1,0|a^\dagger a\lambda^2|1,2\rangle \\ \langle 1,1|a^\dagger a\lambda^2|0,0\rangle & \langle 1,1|a^\dagger a\lambda^2|1,0\rangle & \langle 1,1|a^\dagger a\lambda^2|1,1\rangle & \langle 1,1|a^\dagger a\lambda^2|1,2\rangle \\ \langle 1,2|a^\dagger a\lambda^2|0,0\rangle & \langle 1,2|a^\dagger a\lambda^2|1,0\rangle & \langle 1,2|a^\dagger a\lambda^2|1,1\rangle & \langle 1,2|a^\dagger a\lambda^2|1,2\rangle\end{bmatrix} \tag{2.16}$$

As shown in Eq. 2.9, $a^\dagger a$ results in the number of electronic quanta on a given state, while b and $b^\dagger$ result in a state with one fewer or one greater number of vibrational

quanta, as well as a scaling factor based on the number of quanta. The term λ^2 is simply a scalar. Applying the operators in Eq. 2.14-2.16 results in Eq. 2.17-2.19.

$$\langle\psi_1|\hat{H}_{el-vib-upper}|\psi_1\rangle = \omega_0\lambda\begin{bmatrix} \langle 0,0|0\times 1|0,1\rangle & \langle 0,0|1\times 1|1,1\rangle & \langle 0,0|1\times\sqrt{2}|1,2\rangle & \langle 0,0|1\times\sqrt{3}|1,3\rangle \\ \langle 1,0|0\times 1|0,1\rangle & \langle 1,0|1\times 1|1,1\rangle & \langle 1,0|1\times\sqrt{2}|1,2\rangle & \langle 1,0|1\times\sqrt{3}|1,3\rangle \\ \langle 1,1|0\times 1|0,1\rangle & \langle 1,1|1\times 1|1,1\rangle & \langle 1,1|1\times\sqrt{2}|1,2\rangle & \langle 1,1|1\times\sqrt{3}|1,3\rangle \\ \langle 1,2|0\times 1|0,1\rangle & \langle 1,2|1\times 1|1,1\rangle & \langle 1,2|1\times\sqrt{2}|1,2\rangle & \langle 1,2|1\times\sqrt{3}|1,3\rangle \end{bmatrix} \tag{2.17}$$

$$\langle\psi_1|\hat{H}_{el-vib-lower}|\psi_1\rangle = \omega_0\lambda\begin{bmatrix} 0 & 0 & \langle 0,0|1\times 1|1,0\rangle & \langle 0,0|1\times\sqrt{2}|1,1\rangle \\ 0 & 0 & \langle 1,0|1\times 1|1,0\rangle & \langle 1,0|1\times\sqrt{2}|1,1\rangle \\ 0 & 0 & \langle 1,1|1\times 1|1,0\rangle & \langle 1,1|1\times\sqrt{2}|1,1\rangle \\ 0 & 0 & \langle 1,2|1\times 1|1,0\rangle & \langle 1,2|1\times\sqrt{2}|1,1\rangle \end{bmatrix} \tag{2.18}$$

$$\langle\psi_1|\hat{H}_{el-vib-con}|\psi_1\rangle = \omega_0\lambda^2\begin{bmatrix} \langle 0,0|0|0,0\rangle & \langle 0,0|1|1,0\rangle & \langle 0,0|1|1,1\rangle & \langle 0,0|1|1,2\rangle \\ \langle 1,0|0|0,0\rangle & \langle 1,0|1|1,0\rangle & \langle 1,0|1|1,1\rangle & \langle 1,0|1|1,2\rangle \\ \langle 1,1|0|0,0\rangle & \langle 1,1|1|1,0\rangle & \langle 1,1|1|1,1\rangle & \langle 1,1|1|1,2\rangle \\ \langle 1,2|0|0,0\rangle & \langle 1,2|1|1,0\rangle & \langle 1,2|1|1,1\rangle & \langle 1,2|1|1,2\rangle \end{bmatrix} \tag{2.19}$$

As before, the orthogonality of the basis states results in most of the matrix elements being 0, as shown in Eq. 2.20-2.22.

$$\langle\psi_1|\hat{H}_{el-vib-upper}|\psi_1\rangle = \omega_0\lambda\begin{bmatrix} 0 & 0 & 0 & 0 \\ 0 & 0 & 0 & 0 \\ 0 & 1 & 0 & 0 \\ 0 & 0 & \sqrt{2} & 0 \end{bmatrix} \tag{2.20}$$

$$\langle\psi_1|\hat{H}_{el-vib-lower}|\psi_1\rangle = \omega_0\lambda\begin{bmatrix} 0 & 0 & 0 & 0 \\ 0 & 0 & 1 & 0 \\ 0 & 0 & 0 & \sqrt{2} \\ 0 & 0 & 0 & 0 \end{bmatrix} \tag{2.21}$$

$$\langle\psi_1|\hat{H}_{el-vib-con}|\psi_1\rangle = \omega_0\lambda^2\begin{bmatrix} 0 & 0 & 0 & 0 \\ 0 & 1 & 0 & 0 \\ 0 & 0 & 1 & 0 \\ 0 & 0 & 0 & 1 \end{bmatrix} \tag{2.22}$$

This example gives a sense of what kinds of states can couple together. When a single creation or annihilation operator is used, states with ±1 quantum couple together.

Summing Eq. 2.10, 2.12, 2.20-2.22 together results in the Hamiltonian shown in Eq. 2.23. The colors denote what kind of interaction each term is from. Blue is electronic, red is vibrational, and purple is vibronic.

$$\langle \psi_1 | \hat{H} | \psi_1 \rangle = \begin{bmatrix} 0 & 0 & 0 & 0 \\ 0 & \varepsilon_0 & \omega_0\lambda & 0 \\ 0 & \omega_0\lambda & \varepsilon_0 + \omega_0 + \omega_0\lambda^2 & \sqrt{2}\omega_0\lambda \\ 0 & 0 & \sqrt{2}\omega_0\lambda & \varepsilon_0 + 2\omega_0 + \omega_0\lambda^2 \end{bmatrix} \tag{2.23}$$

A similar exercise can be done for a dimer using the two-particle approximation (Eq. 2.4) and the Hamiltonian shown in Eq. 2.5, which has electronic coupling between molecules. Like the monomer, we will consider states with up to one electronic quantum and up to two vibrational quanta, though now the states considered can have vibrational quanta on up to two different molecules. The Hamiltonian has an electronic term ($\hat{H}_{el}$), a vibrational term ($\hat{H}_{vib}$), a vibronic term ($\hat{H}_{el-vib}$), and an electronic coupling term ($\hat{H}_J$). Given the basis states shown in Eq. 2.24 and applying the electronic term of the Hamiltonian to those states, we can see which terms will be non-zero, shown in Eq. 2.25.

$$|\psi_2\rangle = \begin{bmatrix} |0,0,0;0,0\rangle \\ |1,1,0;0,0\rangle \\ |1,1,1;0,0\rangle \\ |1,1,2;0,0\rangle \\ |1,1,0;2,1\rangle \\ |1,1,0;2,2\rangle \\ |1,1,1;2,1\rangle \\ |2,1,0;0,0\rangle \\ |2,1,1;0,0\rangle \\ |2,1,2;0,0\rangle \\ |2,1,0;1,1\rangle \\ |2,1,0;1,2\rangle \\ |2,1,1;1,1\rangle \end{bmatrix} \tag{2.24}$$

$$\hat{H}_{el}\left|\psi_2\right\rangle = \varepsilon_0 \begin{bmatrix} a^\dagger a\left|0,0,0;0,0\right\rangle \\ a^\dagger a\left|1,1,0;0,0\right\rangle \\ a^\dagger a\left|1,1,1;0,0\right\rangle \\ a^\dagger a\left|1,1,2;0,0\right\rangle \\ a^\dagger a\left|1,1,0;2,1\right\rangle \\ a^\dagger a\left|1,1,0;2,2\right\rangle \\ a^\dagger a\left|1,1,1;2,1\right\rangle \\ a^\dagger a\left|2,1,0;0,0\right\rangle \\ a^\dagger a\left|2,1,1;0,0\right\rangle \\ a^\dagger a\left|2,1,2;0,0\right\rangle \\ a^\dagger a\left|2,1,0;1,1\right\rangle \\ a^\dagger a\left|2,1,0;1,2\right\rangle \\ a^\dagger a\left|2,1,1;1,1\right\rangle \end{bmatrix} = \varepsilon_0 \begin{bmatrix} 0\times\left|0,0,0;0,0\right\rangle \\ 1\times\left|1,1,0;0,0\right\rangle \\ 1\times\left|1,1,1;0,0\right\rangle \\ 1\times\left|1,1,2;0,0\right\rangle \\ 1\times\left|1,1,0;2,1\right\rangle \\ 1\times\left|1,1,0;2,2\right\rangle \\ 1\times\left|1,1,1;2,1\right\rangle \\ 1\times\left|2,1,0;0,0\right\rangle \\ 1\times\left|2,1,1;0,0\right\rangle \\ 1\times\left|2,1,2;0,0\right\rangle \\ 1\times\left|2,1,0;1,1\right\rangle \\ 1\times\left|2,1,0;1,2\right\rangle \\ 1\times\left|2,1,1;1,1\right\rangle \end{bmatrix} \tag{2.25}$$

As with the monomer, the $a^\dagger a$ term does not change the state it is acting on. Because of this, the only terms that will have non-zero results will be those along the diagonal, except for the term $\left\langle 0,0,0;0,0\right|a^\dagger a\left|0,0,0;0,0\right\rangle$ which results in 0. The completed electronic section of the Hamiltonian is shown in Eq. 2.26.

$$\left\langle\psi_2\right|\hat{H}_{el}\left|\psi_2\right\rangle = \varepsilon_0 \begin{bmatrix} 0 & 0 & 0 & 0 & 0 & 0 & 0 & 0 & 0 & 0 & 0 & 0 & 0 \\ 0 & 1 & 0 & 0 & 0 & 0 & 0 & 0 & 0 & 0 & 0 & 0 & 0 \\ 0 & 0 & 1 & 0 & 0 & 0 & 0 & 0 & 0 & 0 & 0 & 0 & 0 \\ 0 & 0 & 0 & 1 & 0 & 0 & 0 & 0 & 0 & 0 & 0 & 0 & 0 \\ 0 & 0 & 0 & 0 & 1 & 0 & 0 & 0 & 0 & 0 & 0 & 0 & 0 \\ 0 & 0 & 0 & 0 & 0 & 1 & 0 & 0 & 0 & 0 & 0 & 0 & 0 \\ 0 & 0 & 0 & 0 & 0 & 0 & 1 & 0 & 0 & 0 & 0 & 0 & 0 \\ 0 & 0 & 0 & 0 & 0 & 0 & 0 & 1 & 0 & 0 & 0 & 0 & 0 \\ 0 & 0 & 0 & 0 & 0 & 0 & 0 & 0 & 1 & 0 & 0 & 0 & 0 \\ 0 & 0 & 0 & 0 & 0 & 0 & 0 & 0 & 0 & 1 & 0 & 0 & 0 \\ 0 & 0 & 0 & 0 & 0 & 0 & 0 & 0 & 0 & 0 & 1 & 0 & 0 \\ 0 & 0 & 0 & 0 & 0 & 0 & 0 & 0 & 0 & 0 & 0 & 1 & 0 \\ 0 & 0 & 0 & 0 & 0 & 0 & 0 & 0 & 0 & 0 & 0 & 0 & 1 \end{bmatrix} \tag{2.26}$$

The vibrational term of the Hamiltonian also results in non-zero terms only along the diagonal of the Hamiltonian. The value of these terms depends on the total number of vibrational quanta in that state. Applying the vibrational portion of the Hamiltonian to the basis states is shown in Eq. 2.27. The matrix elements of the vibrational portion of the Hamiltonian are shown in Eq. 2.28.

$$\hat{H}_{vib}\left|\psi_2\right\rangle = \omega_0 \begin{bmatrix} b^\dagger b\left|0,0,0;0,0\right\rangle \\ b^\dagger b\left|1,1,0;0,0\right\rangle \\ b^\dagger b\left|1,1,1;0,0\right\rangle \\ b^\dagger b\left|1,1,2;0,0\right\rangle \\ b^\dagger b\left|1,1,0;2,1\right\rangle \\ b^\dagger b\left|1,1,0;2,2\right\rangle \\ b^\dagger b\left|1,1,1;2,1\right\rangle \\ b^\dagger b\left|2,1,0;0,0\right\rangle \\ b^\dagger b\left|2,1,1;0,0\right\rangle \\ b^\dagger b\left|2,1,2;0,0\right\rangle \\ b^\dagger b\left|2,1,0;1,1\right\rangle \\ b^\dagger b\left|2,1,0;1,2\right\rangle \\ b^\dagger b\left|2,1,1;1,1\right\rangle \end{bmatrix} = \omega_0 \begin{bmatrix} 0\times\left|0,0,0;0,0\right\rangle \\ 0\times\left|1,1,0;0,0\right\rangle \\ 1\times\left|1,1,1;0,0\right\rangle \\ 2\times\left|1,1,2;0,0\right\rangle \\ 1\times\left|1,1,0;2,1\right\rangle \\ 2\times\left|1,1,0;2,2\right\rangle \\ 2\times\left|1,1,1;2,1\right\rangle \\ 0\times\left|2,1,0;0,0\right\rangle \\ 1\times\left|2,1,1;0,0\right\rangle \\ 2\times\left|2,1,2;0,0\right\rangle \\ 1\times\left|2,1,0;1,1\right\rangle \\ 2\times\left|2,1,0;1,2\right\rangle \\ 2\times\left|2,1,1;1,1\right\rangle \end{bmatrix} \tag{2.27}$$

$$\left\langle\psi_2\right|\hat{H}_{vib}\left|\psi_2\right\rangle = \omega_0 \begin{bmatrix} 0 & 0 & 0 & 0 & 0 & 0 & 0 & 0 & 0 & 0 & 0 & 0 & 0 \\ 0 & 0 & 0 & 0 & 0 & 0 & 0 & 0 & 0 & 0 & 0 & 0 & 0 \\ 0 & 0 & 1 & 0 & 0 & 0 & 0 & 0 & 0 & 0 & 0 & 0 & 0 \\ 0 & 0 & 0 & 2 & 0 & 0 & 0 & 0 & 0 & 0 & 0 & 0 & 0 \\ 0 & 0 & 0 & 0 & 1 & 0 & 0 & 0 & 0 & 0 & 0 & 0 & 0 \\ 0 & 0 & 0 & 0 & 0 & 2 & 0 & 0 & 0 & 0 & 0 & 0 & 0 \\ 0 & 0 & 0 & 0 & 0 & 0 & 2 & 0 & 0 & 0 & 0 & 0 & 0 \\ 0 & 0 & 0 & 0 & 0 & 0 & 0 & 0 & 0 & 0 & 0 & 0 & 0 \\ 0 & 0 & 0 & 0 & 0 & 0 & 0 & 0 & 1 & 0 & 0 & 0 & 0 \\ 0 & 0 & 0 & 0 & 0 & 0 & 0 & 0 & 0 & 2 & 0 & 0 & 0 \\ 0 & 0 & 0 & 0 & 0 & 0 & 0 & 0 & 0 & 0 & 1 & 0 & 0 \\ 0 & 0 & 0 & 0 & 0 & 0 & 0 & 0 & 0 & 0 & 0 & 2 & 0 \\ 0 & 0 & 0 & 0 & 0 & 0 & 0 & 0 & 0 & 0 & 0 & 0 & 2 \end{bmatrix} \tag{2.28}$$

To show how the vibronic term of the Hamiltonian, $\hat{H}_{el-vib}$, allows vibrational states to couple together, $\hat{H}_{el-vib}$ will again be broken up into three terms $\hat{H}_{el-vib-upper}$, $\hat{H}_{el-vib-lower}$, and $\hat{H}_{el-vib-con}$, as shown in Eq. 2.29.

$$\begin{aligned} \hat{H}_{el-vib-upper} &= \omega_0 a^\dagger a \lambda b^\dagger \\ \hat{H}_{el-vib-lower} &= \omega_0 a^\dagger a \lambda b \\ \hat{H}_{el-vib-con} &= \omega_0 a^\dagger a \lambda^2 \end{aligned} \tag{2.29}$$

Applying each of these terms to the basis states shown in Eq. 2.24 is shown in Eq. 2.30-2.32. The states in red are not basis states of this model and will not couple with any basis states.

$$\hat{H}_{el-vib-upper}\left|\psi_2\right\rangle=\omega_0\begin{bmatrix}a^\dagger a\lambda b^\dagger\left|0,0,0;0,0\right\rangle\\ a^\dagger a\lambda b^\dagger\left|1,1,0;0,0\right\rangle\\ a^\dagger a\lambda b^\dagger\left|1,1,1;0,0\right\rangle\\ a^\dagger a\lambda b^\dagger\left|1,1,2;0,0\right\rangle\\ a^\dagger a\lambda b^\dagger\left|1,1,0;2,1\right\rangle\\ a^\dagger a\lambda b^\dagger\left|1,1,0;2,2\right\rangle\\ a^\dagger a\lambda b^\dagger\left|1,1,1;2,1\right\rangle\\ a^\dagger a\lambda b^\dagger\left|2,1,0;0,0\right\rangle\\ a^\dagger a\lambda b^\dagger\left|2,1,1;0,0\right\rangle\\ a^\dagger a\lambda b^\dagger\left|2,1,2;0,0\right\rangle\\ a^\dagger a\lambda b^\dagger\left|2,1,0;1,1\right\rangle\\ a^\dagger a\lambda b^\dagger\left|2,1,0;1,2\right\rangle\\ a^\dagger a\lambda b^\dagger\left|2,1,1;1,1\right\rangle\end{bmatrix}=\omega_0\begin{bmatrix}0\times\lambda\times1\left|1,0,1;0,0\right\rangle\\ 1\times\lambda\times1\left|1,1,1;0,0\right\rangle\\ 1\times\lambda\times\sqrt{2}\left|1,1,2;0,0\right\rangle\\ 1\times\lambda\times\sqrt{3}\left|1,1,3;0,0\right\rangle\\ 1\times\lambda\times1\left|1,1,1;2,1\right\rangle\\ 1\times\lambda\times1\left|1,1,1;2,2\right\rangle\\ 1\times\lambda\times\sqrt{2}\left|1,1,2;2,1\right\rangle\\ 1\times\lambda\times1\left|2,1,1;0,0\right\rangle\\ 1\times\lambda\times\sqrt{2}\left|2,1,2;0,0\right\rangle\\ 1\times\lambda\times\sqrt{3}\left|2,1,3;0,0\right\rangle\\ 1\times\lambda\times1\left|2,1,1;1,1\right\rangle\\ 1\times\lambda\times1\left|2,1,1;1,2\right\rangle\\ 1\times\lambda\times\sqrt{2}\left|2,1,2;1,1\right\rangle\end{bmatrix}\tag{2.30}$$

$$\hat{H}_{el-vib-lower}\left|\psi_2\right\rangle=\omega_0\begin{bmatrix}a^\dagger a\lambda b\left|0,0,0;0,0\right\rangle\\ a^\dagger a\lambda b\left|1,1,0;0,0\right\rangle\\ a^\dagger a\lambda b\left|1,1,1;0,0\right\rangle\\ a^\dagger a\lambda b\left|1,1,2;0,0\right\rangle\\ a^\dagger a\lambda b\left|1,1,0;2,1\right\rangle\\ a^\dagger a\lambda b\left|1,1,0;2,2\right\rangle\\ a^\dagger a\lambda b\left|1,1,1;2,1\right\rangle\\ a^\dagger a\lambda b\left|2,1,0;0,0\right\rangle\\ a^\dagger a\lambda b\left|2,1,1;0,0\right\rangle\\ a^\dagger a\lambda b\left|2,1,2;0,0\right\rangle\\ a^\dagger a\lambda b\left|2,1,0;1,1\right\rangle\\ a^\dagger a\lambda b\left|2,1,0;1,2\right\rangle\\ a^\dagger a\lambda b\left|2,1,1;1,1\right\rangle\end{bmatrix}=\omega_0\begin{bmatrix}0\\ 0\\ 1\times\lambda\times1\left|1,1,0;0,0\right\rangle\\ 1\times\lambda\times\sqrt{2}\left|1,1,1;0,0\right\rangle\\ 0\\ 0\\ 1\times\lambda\times1\left|1,1,0;2,1\right\rangle\\ 0\\ 1\times\lambda\times1\left|2,1,0;0,0\right\rangle\\ 1\times\lambda\times\sqrt{2}\left|2,1,1;0,0\right\rangle\\ 0\\ 0\\ 1\times\lambda\times1\left|2,1,0;1,1\right\rangle\end{bmatrix}\tag{2.31}$$

$$\hat{H}_{el-vib-con}\left|\psi_2\right\rangle=\omega_0\lambda^2\begin{bmatrix}a^\dagger a\left|0,0,0;0,0\right\rangle\\ a^\dagger a\left|1,1,0;0,0\right\rangle\\ a^\dagger a\left|1,1,1;0,0\right\rangle\\ a^\dagger a\left|1,1,2;0,0\right\rangle\\ a^\dagger a\left|1,1,0;2,1\right\rangle\\ a^\dagger a\left|1,1,0;2,2\right\rangle\\ a^\dagger a\left|1,1,1;2,1\right\rangle\\ a^\dagger a\left|2,1,0;0,0\right\rangle\\ a^\dagger a\left|2,1,1;0,0\right\rangle\\ a^\dagger a\left|2,1,2;0,0\right\rangle\\ a^\dagger a\left|2,1,0;1,1\right\rangle\\ a^\dagger a\left|2,1,0;1,2\right\rangle\\ a^\dagger a\left|2,1,1;1,1\right\rangle\end{bmatrix}=\omega_0\lambda^2\begin{bmatrix}0\times\left|0,0,0;0,0\right\rangle\\ 1\times\left|1,1,0;0,0\right\rangle\\ 1\times\left|1,1,1;0,0\right\rangle\\ 1\times\left|1,1,2;0,0\right\rangle\\ 1\times\left|1,1,0;2,1\right\rangle\\ 1\times\left|1,1,0;2,2\right\rangle\\ 1\times\left|1,1,1;2,1\right\rangle\\ 1\times\left|2,1,0;0,0\right\rangle\\ 1\times\left|2,1,1;0,0\right\rangle\\ 1\times\left|2,1,2;0,0\right\rangle\\ 1\times\left|2,1,0;1,1\right\rangle\\ 1\times\left|2,1,0;1,2\right\rangle\\ 1\times\left|2,1,1;1,1\right\rangle\end{bmatrix}\tag{2.32}$$

The orthogonality of the basis states results in most of the matrix elements in the Hamiltonian being 0. The non-zero terms for $\hat{H}_{el-vib-upper}$ come from basis states coupling with other basis states that have one more vibrational quantum. Similarly, for $\hat{H}_{el-vib-lower}$, non-zero terms come from basis states coupling with other basis states that have one fewer vibrational quantum. Like the monomer, the term $\hat{H}_{el-vib-con}$ does not change the state it is acting on and results in non-zero terms along the diagonal. Because of the $a^{\dagger}a$ term in all the vibronic terms, coupling will only occur between states that have the electronic excitation on the same molecule. A matrix representation of these terms is shown below in Eq. 2.33-2.35 and are summed together in Eq. 2.36.

$$\left\langle \psi_2 \left| \hat{H}_{el-vib-upper} \right| \psi_2 \right\rangle = \omega_0 \lambda \begin{bmatrix} 0 & 0 & 0 & 0 & 0 & 0 & 0 & 0 & 0 & 0 & 0 & 0 & 0 \\ 0 & 0 & 0 & 0 & 0 & 0 & 0 & 0 & 0 & 0 & 0 & 0 & 0 \\ 0 & 1 & 0 & 0 & 0 & 0 & 0 & 0 & 0 & 0 & 0 & 0 & 0 \\ 0 & 0 & \sqrt{2} & 0 & 0 & 0 & 0 & 0 & 0 & 0 & 0 & 0 & 0 \\ 0 & 0 & 0 & 0 & 0 & 0 & 0 & 0 & 0 & 0 & 0 & 0 & 0 \\ 0 & 0 & 0 & 0 & 1 & 0 & 0 & 0 & 0 & 0 & 0 & 0 & 0 \\ 0 & 0 & 0 & 0 & 0 & 0 & 0 & 0 & 0 & 0 & 0 & 0 & 0 \\ 0 & 0 & 0 & 0 & 0 & 0 & 1 & 0 & 0 & 0 & 0 & 0 & 0 \\ 0 & 0 & 0 & 0 & 0 & 0 & 0 & \sqrt{2} & 0 & 0 & 0 & 0 & 0 \\ 0 & 0 & 0 & 0 & 0 & 0 & 0 & 0 & 0 & 0 & 0 & 0 & 0 \\ 0 & 0 & 0 & 0 & 0 & 0 & 0 & 0 & 0 & 0 & 0 & 0 & 0 \\ 0 & 0 & 0 & 0 & 0 & 0 & 0 & 0 & 0 & 0 & 0 & 0 & 0 \\ 0 & 0 & 0 & 0 & 0 & 0 & 0 & 0 & 0 & 0 & 0 & 1 & 0 \end{bmatrix} \tag{2.33}$$

$$\left\langle \psi_2 \left| \hat{H}_{el-vib-lower} \right| \psi_2 \right\rangle = \omega_0 \lambda \begin{bmatrix} 0 & 0 & 0 & 0 & 0 & 0 & 0 & 0 & 0 & 0 & 0 & 0 & 0 \\ 0 & 0 & 1 & 0 & 0 & 0 & 0 & 0 & 0 & 0 & 0 & 0 & 0 \\ 0 & 0 & 0 & \sqrt{2} & 0 & 0 & 0 & 0 & 0 & 0 & 0 & 0 & 0 \\ 0 & 0 & 0 & 0 & 0 & 0 & 0 & 0 & 0 & 0 & 0 & 0 & 0 \\ 0 & 0 & 0 & 0 & 0 & 1 & 0 & 0 & 0 & 0 & 0 & 0 & 0 \\ 0 & 0 & 0 & 0 & 0 & 0 & 0 & 0 & 0 & 0 & 0 & 0 & 0 \\ 0 & 0 & 0 & 0 & 0 & 0 & 0 & 1 & 0 & 0 & 0 & 0 & 0 \\ 0 & 0 & 0 & 0 & 0 & 0 & 0 & 0 & \sqrt{2} & 0 & 0 & 0 & 0 \\ 0 & 0 & 0 & 0 & 0 & 0 & 0 & 0 & 0 & 0 & 0 & 0 & 0 \\ 0 & 0 & 0 & 0 & 0 & 0 & 0 & 0 & 0 & 0 & 0 & 0 & 0 \\ 0 & 0 & 0 & 0 & 0 & 0 & 0 & 0 & 0 & 0 & 0 & 0 & 0 \\ 0 & 0 & 0 & 0 & 0 & 0 & 0 & 0 & 0 & 0 & 0 & 0 & 1 \\ 0 & 0 & 0 & 0 & 0 & 0 & 0 & 0 & 0 & 0 & 0 & 0 & 0 \end{bmatrix} \tag{2.34}$$

$$\langle \psi_2 | \hat{H}_{el-vib-con} | \psi_2 \rangle = \omega_0 \lambda^2 \begin{bmatrix} 0 & 0 & 0 & 0 & 0 & 0 & 0 & 0 & 0 & 0 & 0 & 0 & 0 \\ 0 & 1 & 0 & 0 & 0 & 0 & 0 & 0 & 0 & 0 & 0 & 0 & 0 \\ 0 & 0 & 1 & 0 & 0 & 0 & 0 & 0 & 0 & 0 & 0 & 0 & 0 \\ 0 & 0 & 0 & 1 & 0 & 0 & 0 & 0 & 0 & 0 & 0 & 0 & 0 \\ 0 & 0 & 0 & 0 & 1 & 0 & 0 & 0 & 0 & 0 & 0 & 0 & 0 \\ 0 & 0 & 0 & 0 & 0 & 1 & 0 & 0 & 0 & 0 & 0 & 0 & 0 \\ 0 & 0 & 0 & 0 & 0 & 0 & 1 & 0 & 0 & 0 & 0 & 0 & 0 \\ 0 & 0 & 0 & 0 & 0 & 0 & 0 & 1 & 0 & 0 & 0 & 0 & 0 \\ 0 & 0 & 0 & 0 & 0 & 0 & 0 & 0 & 1 & 0 & 0 & 0 & 0 \\ 0 & 0 & 0 & 0 & 0 & 0 & 0 & 0 & 0 & 1 & 0 & 0 & 0 \\ 0 & 0 & 0 & 0 & 0 & 0 & 0 & 0 & 0 & 0 & 1 & 0 & 0 \\ 0 & 0 & 0 & 0 & 0 & 0 & 0 & 0 & 0 & 0 & 0 & 1 & 0 \\ 0 & 0 & 0 & 0 & 0 & 0 & 0 & 0 & 0 & 0 & 0 & 0 & 1 \end{bmatrix} \tag{2.35}$$

$$\langle \psi_2 | \hat{H}_{el-vib} | \psi_2 \rangle = \omega_0 \begin{bmatrix} 0 & 0 & 0 & 0 & 0 & 0 & 0 & 0 & 0 & 0 & 0 & 0 & 0 \\ 0 & \lambda^2 & \lambda & 0 & 0 & 0 & 0 & 0 & 0 & 0 & 0 & 0 & 0 \\ 0 & \lambda & \lambda^2 & \sqrt{2}\lambda & 0 & 0 & 0 & 0 & 0 & 0 & 0 & 0 & 0 \\ 0 & 0 & \sqrt{2}\lambda & \lambda^2 & 0 & 0 & 0 & 0 & 0 & 0 & 0 & 0 & 0 \\ 0 & 0 & 0 & 0 & \lambda^2 & \lambda & 0 & 0 & 0 & 0 & 0 & 0 & 0 \\ 0 & 0 & 0 & 0 & \lambda & \lambda^2 & 0 & 0 & 0 & 0 & 0 & 0 & 0 \\ 0 & 0 & 0 & 0 & 0 & 0 & \lambda^2 & \lambda & 0 & 0 & 0 & 0 & 0 \\ 0 & 0 & 0 & 0 & 0 & 0 & \lambda & \lambda^2 & \sqrt{2}\lambda & 0 & 0 & 0 & 0 \\ 0 & 0 & 0 & 0 & 0 & 0 & 0 & \sqrt{2}\lambda & \lambda^2 & 0 & 0 & 0 & 0 \\ 0 & 0 & 0 & 0 & 0 & 0 & 0 & 0 & 0 & \lambda^2 & 0 & 0 & 0 \\ 0 & 0 & 0 & 0 & 0 & 0 & 0 & 0 & 0 & 0 & \lambda^2 & 0 & 0 \\ 0 & 0 & 0 & 0 & 0 & 0 & 0 & 0 & 0 & 0 & 0 & \lambda^2 & \lambda \\ 0 & 0 & 0 & 0 & 0 & 0 & 0 & 0 & 0 & 0 & 0 & \lambda & \lambda^2 \end{bmatrix} \tag{2.36}$$

The final term of the Hamiltonian, $\hat{H}_J$, couples the electronic states between two molecules through Coulombic interactions. In general, $\hat{H}_J$ is defined as in Eq. 2.37, where $J_{m,n}$ is the strength of coupling between molecules n and m, and $a_m^\dagger$ (a_m) is the creation (annihilation) operator for the electronic quantum on molecule m.

$$\hat{H}_J = \sum_{n=1}^{N} \sum_{m \neq n}^{N} J_{m,n} \left(a_m^\dagger a_n + a_m a_n^\dagger \right) \tag{2.37}$$

In the case of a dimer, we can explicitly represent $\hat{H}_J$, shown in Eq. 2.38.

$$\hat{H}_J = J_{1,2} \left(a_1^\dagger a_2 + a_1 a_2^\dagger \right) \tag{2.38}$$

Like the vibronic term, we can separate this into terms called $\hat{H}_{J-1,2}$ and $\hat{H}_{J-2,1}$, and apply them to the basis states, as shown in Eq. 2.39 and Eq. 2.40.

$$\hat{H}_{J-1,2}\left|\psi_2\right\rangle = J_{1,2}\begin{bmatrix} a_1^\dagger a_2\left|0,0,0;0,0\right\rangle \\ a_1^\dagger a_2\left|1,1,0;0,0\right\rangle \\ a_1^\dagger a_2\left|1,1,1;0,0\right\rangle \\ a_1^\dagger a_2\left|1,1,2;0,0\right\rangle \\ a_1^\dagger a_2\left|1,1,0;2,1\right\rangle \\ a_1^\dagger a_2\left|1,1,0;2,2\right\rangle \\ a_1^\dagger a_2\left|1,1,1;2,1\right\rangle \\ a_1^\dagger a_2\left|2,1,0;0,0\right\rangle \\ a_1^\dagger a_2\left|2,1,1;0,0\right\rangle \\ a_1^\dagger a_2\left|2,1,2;0,0\right\rangle \\ a_1^\dagger a_2\left|2,1,0;1,1\right\rangle \\ a_1^\dagger a_2\left|2,1,0;1,2\right\rangle \\ a_1^\dagger a_2\left|2,1,1;1,1\right\rangle \end{bmatrix} = J_{1,2}\begin{bmatrix} 0 \\ 0 \\ 0 \\ 0 \\ 0 \\ 0 \\ 1\times\left|1,1,0;0,0\right\rangle \\ 1\times\left|1,1,1;2,1\right\rangle \\ 1\times\left|1,1,0;2,2\right\rangle \\ 1\times\left|1,1,1;0,0\right\rangle \\ 1\times\left|1,1,2;0,0\right\rangle \\ 1\times\left|1,1,1;2,1\right\rangle \end{bmatrix} \tag{2.39}$$

$$\hat{H}_{J-2,1}\left|\psi_2\right\rangle = J_{1,2}\begin{bmatrix} a_1 a_2^\dagger\left|0,0,0;0,0\right\rangle \\ a_1 a_2^\dagger\left|1,1,0;0,0\right\rangle \\ a_1 a_2^\dagger\left|1,1,1;0,0\right\rangle \\ a_1 a_2^\dagger\left|1,1,2;0,0\right\rangle \\ a_1 a_2^\dagger\left|1,1,0;2,1\right\rangle \\ a_1 a_2^\dagger\left|1,1,0;2,2\right\rangle \\ a_1 a_2^\dagger\left|1,1,1;2,1\right\rangle \\ a_1 a_2^\dagger\left|2,1,0;0,0\right\rangle \\ a_1 a_2^\dagger\left|2,1,1;0,0\right\rangle \\ a_1 a_2^\dagger\left|2,1,2;0,0\right\rangle \\ a_1 a_2^\dagger\left|2,1,0;1,1\right\rangle \\ a_1 a_2^\dagger\left|2,1,0;1,2\right\rangle \\ a_1 a_2^\dagger\left|2,1,1;1,1\right\rangle \end{bmatrix} = J_{1,2}\begin{bmatrix} 0 \\ 1\times\left|2,1,0;0,0\right\rangle \\ 1\times\left|2,1,0;1,1\right\rangle \\ 1\times\left|2,1,0;1,2\right\rangle \\ 1\times\left|2,1,1;0,0\right\rangle \\ 1\times\left|2,1,2;0,0\right\rangle \\ 1\times\left|2,1,1;1,1\right\rangle \\ 0 \\ 0 \\ 0 \\ 0 \\ 0 \\ 0 \end{bmatrix} \tag{2.40}$$

Each of the basis states will only couple with other states that have the same configuration of vibrational quanta, but with the electron excitation existing on different molecules. The matrix elements for $\hat{H}_J$ are shown in Eq. 2.41.

$$\langle \psi_2 | \hat{H}_J | \psi_2 \rangle = J_{1,2} \begin{bmatrix} 0 & 0 & 0 & 0 & 0 & 0 & 0 & 0 & 0 & 0 & 0 & 0 \\ 0 & 0 & 0 & 0 & 0 & 0 & 0 & 1 & 0 & 0 & 0 & 0 & 0 \\ 0 & 0 & 0 & 0 & 0 & 0 & 0 & 0 & 0 & 0 & 1 & 0 & 0 \\ 0 & 0 & 0 & 0 & 0 & 0 & 0 & 0 & 0 & 0 & 0 & 1 & 0 \\ 0 & 0 & 0 & 0 & 0 & 0 & 0 & 0 & 1 & 0 & 0 & 0 & 0 \\ 0 & 0 & 0 & 0 & 0 & 0 & 0 & 0 & 0 & 1 & 0 & 0 & 0 \\ 0 & 0 & 0 & 0 & 0 & 0 & 0 & 0 & 0 & 0 & 0 & 0 & 1 \\ 0 & 1 & 0 & 0 & 0 & 0 & 0 & 0 & 0 & 0 & 0 & 0 & 0 \\ 0 & 0 & 0 & 0 & 1 & 0 & 0 & 0 & 0 & 0 & 0 & 0 & 0 \\ 0 & 0 & 0 & 0 & 0 & 1 & 0 & 0 & 0 & 0 & 0 & 0 & 0 \\ 0 & 0 & 1 & 0 & 0 & 0 & 0 & 0 & 0 & 0 & 0 & 0 & 0 \\ 0 & 0 & 0 & 1 & 0 & 0 & 0 & 0 & 0 & 0 & 0 & 0 & 0 \\ 0 & 0 & 0 & 0 & 0 & 0 & 1 & 0 & 0 & 0 & 0 & 0 & 0 \end{bmatrix} \tag{2.41}$$

The sum of all the terms for the dimer can be shown using a color-coded grid, where blue show electronic terms, red shows vibrational terms, purple shows vibronic terms, and orange shows Coulombic coupling terms.

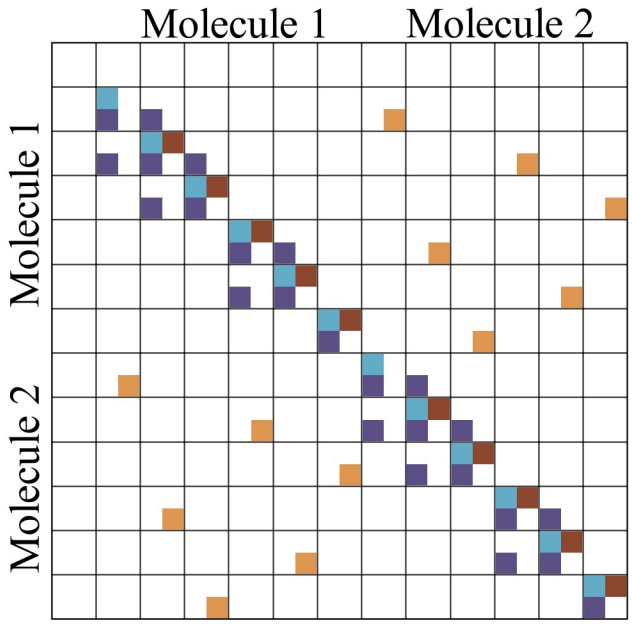

Figure 2.1. Color coded Hamiltonian for a molecular dimer with a single electronic quantum, and up to two vibrational quanta.

2.3 – The Impact of Parameters on Simulated Spectra

Upon construction of a Hamiltonian, the Hamiltonian is diagonalized to determine the eigenstates and eigenenergies. The eigenstates are a linear combination of the basis

states, with the weights of each basis state being determined upon the diagonalization of the Hamiltonian. The eigenenergies are the values along the diagonal after diagonalization, and report on the energy of each eigenstate. The intensity of a transition from the ground state to an eigenstate with a particular eigenenergy depends on the square of the matrix elements of the TDM that correspond to that transition. The equation used to generate the absorption spectrum is shown in Eq. 2.42, where $A(\omega)$ is the energy-dependent signal, $\langle G|$ is the ground state, $\hat{\mu}$ is the TDM operator, $\left|\varphi^{(\alpha)}\right\rangle$ is the α^{th} eigenstate, and $V_p\left(\omega-\omega^{(\alpha)}, f\right)$ is a pseudo-Voigt line shape, which depends on the eigenenergy, $\omega^{(\alpha)}$, and a broadening term, *f*. The pseudo-Voigt line shape is discussed in more detail in Section 2.4.

$$A(\omega) \propto \sum_{\alpha}\left|\langle G|\hat{\mu}\left|\varphi^{(\alpha)}\right\rangle\right|^2 V_p\left(\omega-\omega^{(\alpha)}, f\right) \tag{2.42}$$

The energy of the electronic (ε_0) and vibrational (ω_0) quanta, the Huang-Rhys factor (λ^2) and strength of Coulombic coupling (*J*) all impact the simulated spectrum in different ways. Changing the value of the electronic quantum simply shifts the energy of the overall spectrum, as shown in Figure 2.2. In the following figures, all spectra are broadened using a pseudo-Voigt line shape with a broadening parameter of $f = 150$ cm^{-1} and normalized. The broadening function used is discussed in more detail in Section 2.4.

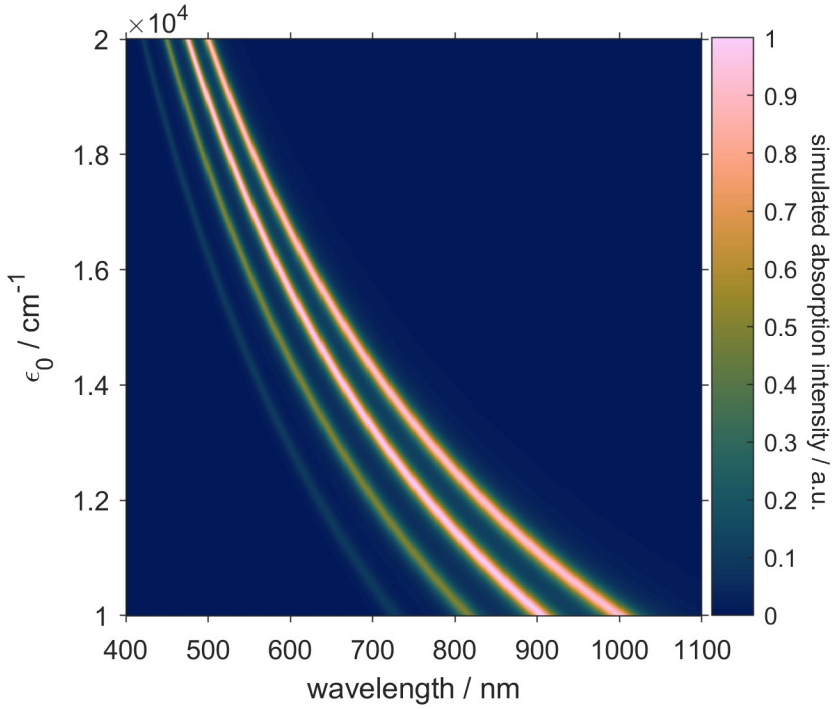

Figure 2.2. False colored linear absorption spectra for a monomer with varying values for ε_0 from 10000 cm^{-1} to 20000 cm^{-1}, in steps of 5 cm^{-1}. The values of the other parameters are ω_0 = 1000 cm^{-1} and $\lambda^2 = 1$.

As the energy of the electronic quantum increases, the absorption spectrum shifts to bluer wavelengths. The apparent decrease in energy between peaks is an artifact of representing the energy of the spectra in wavelength, as the wavelength scale is not linear in energy. Similarly, the impact of the vibrational quantum is shown in Figure 2.3.

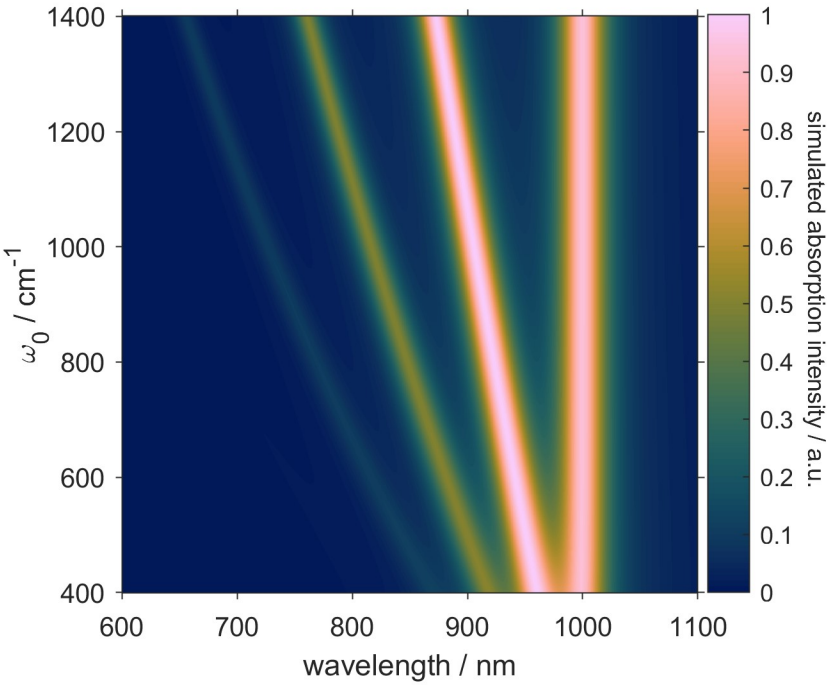

Figure 2.3. False colored linear absorption spectra for a monomer with varying values for ω_0 from 400 cm^{-1} to 1400 cm^{-1} in steps of 1 cm^{-1}. The values of the other parameters are ε_0 = 10000 cm^{-1} and λ^2 = 1.

Changing ω_0 results in different spacing between vibrational peaks. Like in Figure 2.2, at higher energies (not shown here), it appears the energy of the vibration peaks increases more than ω_0 would suggest. This, again, is an artifact of representing the energy of the spectra in wavelength. The final parameter that can change the spectrum of a monomer is λ^2, which is a measure of the displacement between the ground state and excited state potential energy surfaces. Varying λ^2 changes the simulated spectra in more subtle ways, as shown in Figure 2.4.

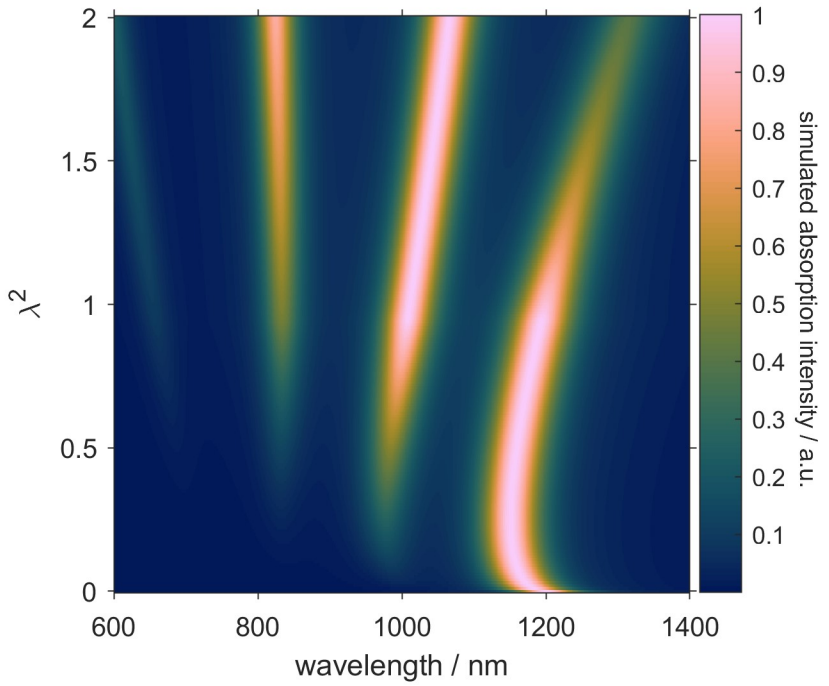

Figure 2.4. False colored linear absorption spectra for a monomer with varying values for λ^2 from 0 to 2 in steps of 0.01. The values of the other parameters are ε_0 = 10000 cm^{-1} and ω_0 = 1000 cm^{-1}.

The most noticeable difference in spectra with different λ^2 values is the change in the intensity ratio between the red-most peak and the second red-most peak. As λ^2 increases from 0 until 1, the second red-most peak become more intense. When $\lambda^2 = 1$, these two peaks have the same intensity. When λ^2 is larger than one, the second red-most peak becomes more intense than the red-most peak. When λ^2 is less than one, there is a slight blue-shift when compared to when $\lambda^2 = 0$ and $\lambda^2 = 1$. Values for λ^2 larger than ~2 are not typical for conjugated small organic molecules.

When the transition dipole moments of two molecules interact with each other an energy splitting can occur. This is known as Coulombic coupling (*J*) and can occur in dimers and larger aggregates. Depending on the sign of the coupling, either the lower energy state or higher energy state will have a non-zero transition dipole moment and be

bright, while the other state will be dark. Negative coupling results in a bright state that is lower in energy, whereas positive coupling results in a bright state that is overall higher in energy. As shown in Figure 2.5, the dominant feature when J is negative is an intense red-shifted peak when compared to the case of zero coupling. This is most evident when looking at the peaks around -1000 cm^{-1}. Conversely, large positive J values result in the most intense peak blue-shifting and increasing in intensity, with the intensity of the red-most peak greatly decreasing.

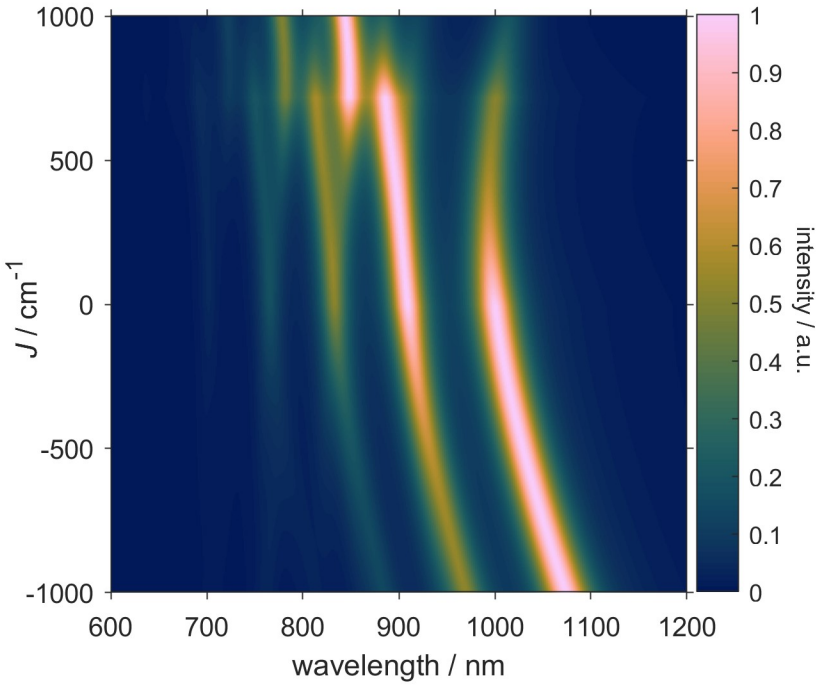

Figure 2.5. False colored linear absorption spectra for a linear dimer with varying values of J, from -1000 cm^{-1} to 1000 cm^{-1} in steps of 1 cm^{-1}. The values of the other parameters are ε_0 = 10000 cm^{-1}, ω_0 = 1000 cm^{-1}, and λ^2 = 1.

Increasing the size of aggregates exaggerates the effect of the Coulombic coupling on the spectrum. Figure 2.6 shows the absorption spectra of trimers with the same parameters as the dimers in Figure 2.5. At -1000 cm^{-1}, the red-most peak in the dimer is at approximately 1075 nm, whereas the same peak for the trimer occurs at a

longer wavelength. The relative intensity of the red-most peak is almost much larger in the trimer, as shown by the darker color scale. The spectra from trimers with positive coupling values also exhibit a larger spectral shift and change in intensity than dimers with the same parameters, though this impact is more subtle.

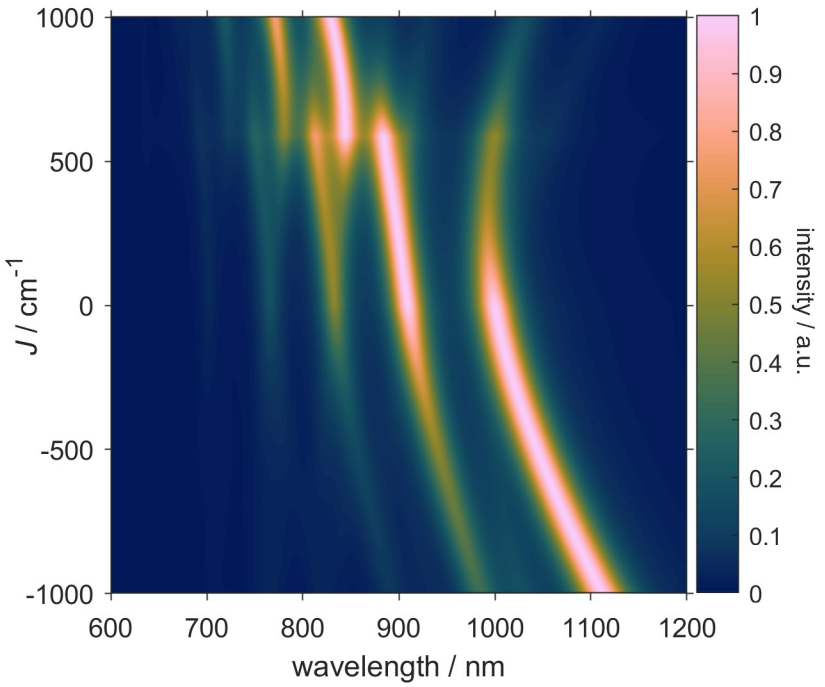

Figure 2.6. False colored linear absorption spectra for a linear trimer with varying values of J, from -1000 cm^{-1} to 1000 cm^{-1} in steps of 1 cm^{-1}. The values of the other parameters are ε_0 = 10000 cm^{-1}, ω_0 = 1000 cm^{-1}, and λ^2 = 1.

While the effect of changing the energy of the electronic and vibrational quanta is straight forward, changing the Huang-Rhys factor and the magnitude and sign of the Coulombic coupling can result in complicated changes in the intensity and energy of absorption peaks. A negative Coulombic coupling is most often associated with an intense, low energy peak, though similar peaks could arise from a small Huang-Rhys factor. Additionally, changing the size of an aggregate can increase or decrease the apparent magnitude of the Coulombic coupling. When analyzing an experimental

spectrum, it is important to consider that a range of values for the spectral parameters can result in similar simulated spectra.

2.4 – Spectral Broadening Using a Pseudo-Voigt Line Shape

As mentioned in Section 2.2, diagonalizing a Hamiltonian and applying the appropriate TDM will result in energies and intensities of allowed transitions. Due to various physical processes, a range of energies are involved in the transition and the peaks in the spectrum are broadened. In this section, we will discuss some of the sources of broadening, as well as introduce the broadening function used to broaden simulated spectra shown in this dissertation.

Spectral peaks have a width and can exhibit spectral shifts due to local and non-local processes. Fluctuations in the energy of the absorbed or emitted state can be categorized as being either “homogeneous” or “inhomogeneous”. In homogeneous broadening, a population of chromophores will all experience the same fluctuation. For example, due to the energy-time uncertainty principle, the lifetime of an excitation is related to the fluctuation in observable energies for that excitation. As a result, all chromophores responsible for that excitation will have the same intrinsic spectral broadening. Another common source of homogeneous broadening is known as pressure broadening or collision broadening. As the name suggests, this results from collisions between chromophores and surrounding molecules. When a collision occurs, an excitation can be emitted and absorbed by a nearby molecule, typically on a time scale much faster than the lifetime of the excitation. The overall lifetime of the excitation will be shorter, and due to the uncertainty principle, the broadening will be larger. Pressure broadening increases with temperature and pressure. Homogeneous broadening results in

a Lorentzian line shape. Inhomogeneous broadening occurs when each emitter or absorber exhibits a different fluctuation in energy. Inhomogeneous broadening is especially common in solids and heterogenous materials, as a change in the local environment can result in a change in energy or a change in the energy fluctuations. Inhomogeneous broadening results in a Gaussian line shape. If the sources of homogeneous and inhomogeneous broadening are independent, the total broadening is a convolution of a Gaussian and Lorentzian, known as a Voigt profile.

A Voigt profile can be simplified using a pseudo-Voigt profile, which uses a linear combination of Gaussian and Lorentzian line shapes. The broadening and relative intensity of the Gaussian and Lorentzian line shapes depend on a homogeneous broadening term (γ) and an inhomogeneous broadening term (σ). The general form of a pseudo-Voigt profile is shown in Eq. 2.43, where $L(\omega,f)$ is the Lorentzian line shape, $G(\omega,f)$ is the Gaussian line shape, η is the relative contribution of the two line shapes, ω is the energy coordinate along which the broadening is occurring, in this case wavenumber, f is the total full width at half maximum (FWHM), and d is a progressive broadening term.

$$V(\omega, f+d) = \eta \cdot L(\omega, f+d) + (1-\eta) \cdot G(\omega, f+d) \tag{2.43}$$

Both η and f depend on a Lorentzian (f_L) and Gaussian (f_G) FWHM, as shown in Eq. 2.44 and 2.45. This approximation for η and f is accurate to within 1%.[109]

$$f = \left[f_G^5 + 2.69269 f_G^4 f_L + 2.42843 f_G^3 f_L^2 + 0.07842 f_G f_L^4 + f_L^5 \right]^{1/5} \tag{2.44}$$

$$\eta = 1.36603\left(f_L/f\right) - 0.47719\left(f_L/f\right)^2 + 0.11116\left(f_L/f\right)^3 \tag{2.45}$$

As shown in Figure 2.7 and Figure 2.8, if either the Gaussian or Lorentzian FWHM is 0, the values of η and f reduce the pseudo-Voigt profile to either a Lorentzian or Gaussian line shape, respectively.

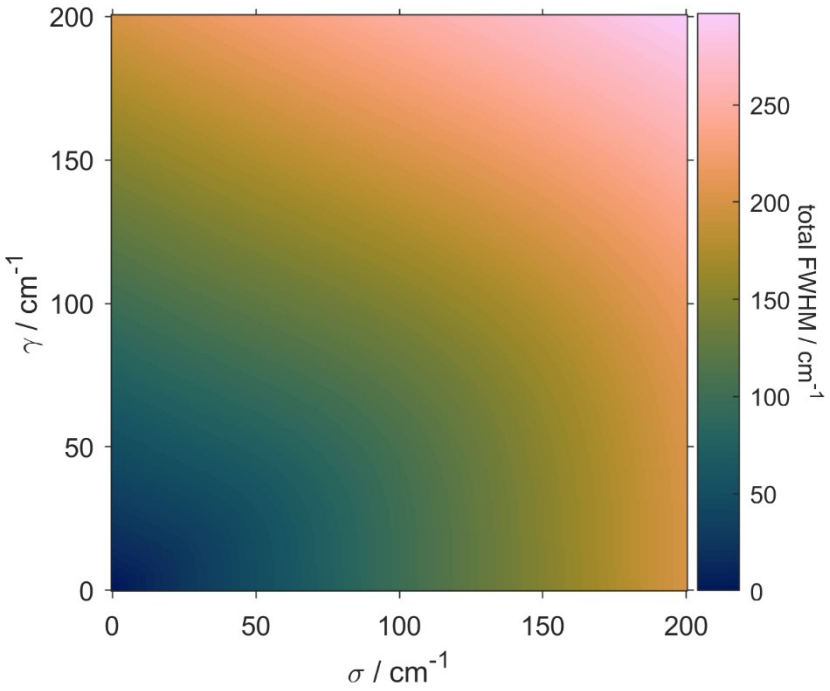

Figure 2.7. Calculated values for the total FWHM (*f*), as a function of the Lorentzian and Gaussian broadening terms.

The progressive broadening term in Eq. 2.43, *d*, scales linearly with energy, as shown in Eq. 2.46, where d_0 is the strength of the broadening, ω is the coordinate along which the broadening is occurring, ω_0 is the energy of the vibrational quantum, and ω^* is the energy at which no additional broadening occurs.

$$d = d_0 \left| \frac{\omega^* - \omega}{\omega_0} \right| \tag{2.46}$$

The pseudo-Voigt profile accounts for higher energy vibronic transitions that are not included in the model and decreased the intensity of other high energy vibronic peaks that have an artificially high intensity due to the approximations made in the basis set.

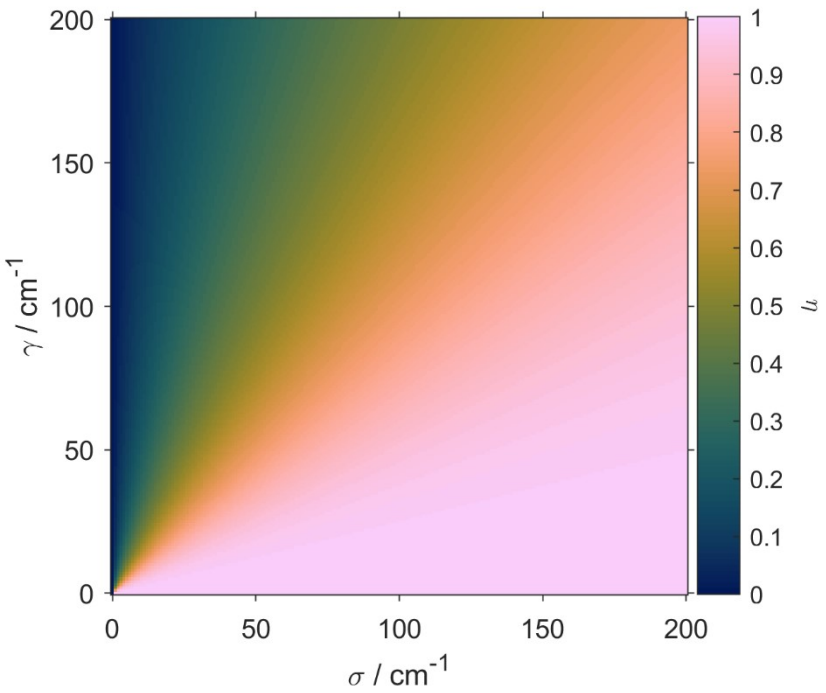

Figure 2.8. Calculated values for η in the pseudo-Voigt profile, as a function of the Lorentzian and Gaussian broadening terms.

2.5 – Comparison of Simulated Spectra to Experimental Spectra

Modeling a series of absorption spectra measured in situ during solution-deposition and film formation will greatly increase the number of calculations required when compared to simply modeling one experimental spectrum. As a result, reductions in computational time must be achieved, for example, by reducing the computational time required to compare a simulated spectrum and experimental spectrum. Additionally, fitting simulated spectra to an experimental spectrum is only feasible with rapid error calculations. Fitting requires a comparison between a simulated spectrum and an experimental spectrum, and having a large number of data points, ~1000 in the case of the experimental spectra shown here, results in error calculations that take a long time. The various parameters shown previously (ε_0 , ω_0 , etc.) can greatly impact the simulated spectrum, mostly affecting peak energy and intensity. As such, only a small number of

energies and intensities need to be considered when comparing an experimental and simulated spectrum to determine agreement between the two spectra. As so few data points are considered, it is especially important to properly sample the parameters space in order to find all possible sets of parameters that result in simulated spectra that agree with experimental spectra. In this section, I will describe a strategy of calculating spectral "metrics" that focus on the spectral features that are most sensitive to aggregate structure, namely the peak energies and relative peak intensities. Additionally, I will outline the procedure for sampling the parameter space, and how the initial sampling will determine which sets of parameters will undergo a least-squares fitting to the experimental spectrum.

Mean-squared error (MSE) between two sets of data can be used to quantify the difference between them. For example, MSE can be used to determine the error between a regression line and a data set. Typically, each data point is given the same importance or weight, though it is also possible to increase or decrease the weight for different parts of the data. In the case of absorption spectra, most of the data exists between peaks and at the red and blue tails of the spectrum. As shown in Section 2.3, changing the various parameters in the Hamiltonian often results in a shift in energy of peaks or in a change in the ratio of peak intensities. Because of this, any measure of the goodness of fit between a simulated spectrum and an experimental spectrum would need to strongly weight data near absorption peaks in the spectrum. Unnecessary error calculations are avoided by implementing an error calculation scheme that only depends on key spectral features we term the spectrum's "metrics". As such, the calculated error is called a "metrics error". The metrics error is a weighted sum based on the square of the difference between the

experimental spectrum and the simulated spectrum. Both the peak energies and intensities are dependent on the values of the parameters in the Hamiltonian, and both are included in the metrics error calculation. Eq. 2.47 shows the general form of a metrics error that depends on the energy and intensity of spectral peaks,

$$e_m = \sum_q^Q w_{E_q} \left(\frac{E_q^* - E_q}{E_q^*} \right)^2 + w_{I_q} \left(\frac{I_q^* - I_q}{I_q^*} \right)^2 \tag{2.47}$$

where e_m is the metrics error, w is the weight, E_q and E_q^* are the simulated and experimental energies of peak q, respectively, and I_q and I_q^* are the simulated and experimental intensities of peak n, respectively. Typically, the weight for the energy of a peak is larger in magnitude than the weight for the intensity simply due to the difference in scale of the two values.

The parameter space for the Hamiltonian depends on the length of an aggregate (n), the energy of the electronic quantum (ε_0), the energy of the vibrational quantum (ω_0), the Huang-Rhys factor (λ^2), and the Coulombic coupling strength (J) if the aggregate is larger than a monomer. Using the experimental spectrum for the monomer, values for ε_0 and ω_0 can be determined quickly by minimizing the MSE between the experimental and simulated spectra. As the monomer only has a length of one and has no Coulombic coupling, simulating and fitting to the experimental spectrum is not computationally expensive. In order to properly sample the parameter space, many spectra are simulated with various parameter values. If ε_0 and ω_0 can be determined from a monomer spectrum, the simulated spectra form a 3-dimensional grid in n-λ^2-J space. A metrics error is then evaluated for each of the simulated spectra, and those that

have an error below a given threshold undergo a least-squares fitting routine to further minimize the metrics error. Spectra with errors that are too large are likely unable to be fit to a local minimum during the least-squares fitting routine, so they are reasonable to discard to decrease the overall computational time.

2.6 – Summary

In this chapter, the theoretical framework for the simulation of absorption spectra was introduced. Using a single-particle basis set with a single electronic excitation and a maximum number of vibrational quanta for a monomer, a step-by-step method for determining the matrix elements of the Hamiltonian was shown. This was repeated using a two-particle approximation for the basis states for a dimer showing how the Hamiltonian changes with the inclusion of Coulombic coupling, and to give a sense of the scaling for the basis states and Hamiltonian as larger aggregates are considered. The process of going from a diagonalized Hamiltonian to an absorption spectrum was outlined. Each of the parameters in the Hamiltonian were varied and spectra were simulated, to give some intuition about how the various parameters will impact simulated spectra. These calculations are ultimately used with the purpose of modeling experimental spectra. A strategy for calculating error and fitting simulated spectra to an experimental spectrum with minimal computational cost was also discussed. In Chapter 3, these calculations will be demonstrated using the experimental spectrum of a well-studied organic semiconductor, pseudoisocyanine.

CHAPTER III

SIMULATION OF ABSORPTION SPECTRUM OF A MIXTURE OF AGGREGATES

The process of simulating absorption spectra to model experimental spectra is demonstrated in this chapter by using a well-studied organic semiconductor, pseudoisocyanine (PIC). Mixtures of aggregates are common in many real-life systems, such as protein complexes in cell membranes and organelles, bulk heterojunctions that can be used in photovoltaics, and in aggregates of small organic molecules. Heterogeneity in an aggregate mixture can change the behavior of the system, either beneficially or deleteriously, so it is important to develop methods to model aggregation in these kinds of mixtures. Mixtures of aggregates are rarely, if at all, studied in the literature. This is likely due to the large number of unknowns, which makes this a computationally challenging problem. For this dissertation, PIC delivers the perfect model system, as it is well-studied but still has an unclear aggregate structure. PIC exhibits distinct peaks in its line shape, as shown below, and forms a mixture of aggregates during thin film formation. I will demonstrate how a system with an evolving mixture of aggregates can be modeled with relatively little computational cost while fully sampling the parameter space. This can provide insight into the physical and electronic structure of a mixture of aggregates. This general strategy could be adapted to other systems and lead to the ability to understand aggregation in more complicated heterogeneous structures.

The primary obstacle to fitting simulated absorption spectra to an experimental spectrum is that a spectrum is typically comprised of ~1000 individual absorption measurements at ~1000 different energies. Minimizing the error between a single

calculated spectrum and an experimental spectrum would thus require 1000 separate calculations to determine the absolute difference between the two spectra, perhaps followed by further calculations to determine the mean squared error. After the error between a simulated spectrum and experimental spectrum has been calculated, the entire Hamiltonian used to calculate the simulated spectrum must be recalculated, TDMs applied, and broadened before having the error reevaluated. While these calculations are trivial when considered on the individual scale, a single simulated spectrum may be recalculated thousands of times before the error is minimized. Additionally, it is unlikely that a single set of initial parameters would adequately sample the parameter space and find all sets of parameters that produce adequate agreement between the simulated and experimental spectra. As a result, it is important to fit a large number of initial guesses to find as many minima as possible. Using the grid sizes outlined below in Section 3.5, a total of ~$8.6 \cdot 10^6$ possible binary mixtures of aggregates exist in this parameter space. If each of these spectra were compared to an experimental spectrum with 1000 points of energy resolution just once, that would ideally take a 2 GHz processor approximately 4 seconds to calculate. If an average fit requires 100 iterations, the error evaluation step to fit one experimentally measured spectrum would take about 7 minutes. If you repeat this for an in situ measurement with 1000 experimental spectra, the calculation would take five days. This does not take into account the time required to generate the spectra in the first place, nor does it consider that spectra would need to be generated during every iteration of a fitting routine. The strategy employed in this dissertation can sample the entire parameter space while also reducing the number of calculations required by well over 99% compared to brute-force sampling. This strategy could reduce the time to

calculate the error between one grid of parameters and 1000 experimental spectra to ~10 milliseconds. The drastic reduction in time needed for calculations makes modeling mixtures of aggregates during thin film deposition computationally feasible. The result of these calculations is that the evolving distribution of parameters can be shown. An additional level of nuance is added to the calculations by considering whether 2D aggregates or aggregates with charge transfer properties could model experimental spectra. Additionally, the use of two Huang-Rhys factors in the simulation, one for each type of aggregate present, was explored. Finally, these results demonstrate that in order to accurately model aggregates, the Huang-Rhys factor of a monomer should not be used.

3.1 – Experimental Spectrum of Pseudoisocyanine

A solution of PIC in acetone was prepared such that the maximum measured OD during an absorption measurement was approximately 1.0. The solution was drop-cast onto a glass slide placed on an aluminum block that was cooled to 12.5 °C using a recirculating chiller. The deposition stage was placed in a plexiglass container to limit air flow and maintain a 42% ambient humidity. A broadband light-emitting diode (Thorlabs, MNWHL4, 400-700 nm) was focused onto the sample and the transmitted light was collected by an optical fiber connected to a spectrometer (Ocean Optics Flame-T-VIS-NIR).

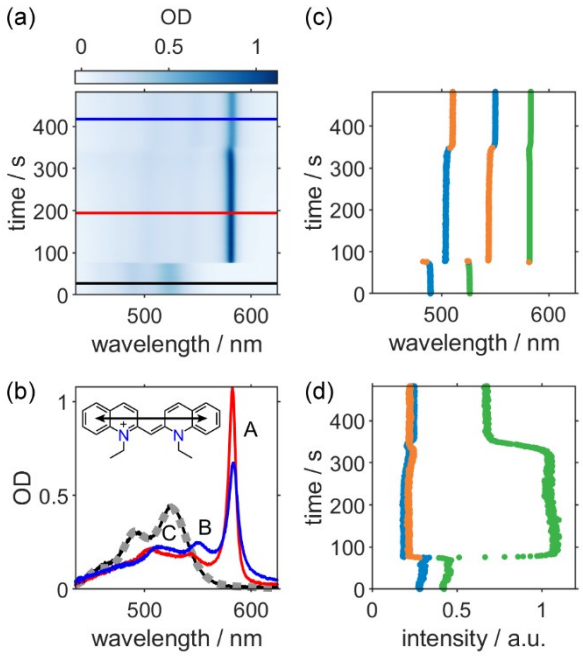

Figure 3.1. In situ absorption measurements during the solution-casting of PIC. (a) Absorption as a function of time after drop-casting a solution of PIC in acetone. Horizontal lines correspond to spectra in (b). (b) Measured absorption at times indicated in (a). Spectrum representative of measurements before 80 s while the molecules are in solution (black), and a simulated spectrum with parameters optimized to fit the solution spectrum (grey dashed). Spectra representative of measurements between 80 s and 350 s (red) and after 355 s (blue), referred to as the "intermediate" and "final" stages, respectively. Peaks A, B, and C are the three largest peaks in order of descending wavelength position. (c) Absorption peak energies. Colors show the peak intensity order (green > blue > orange). (d) Absorption peak intensities. Colors show the peak wavelength order, with green, blue, and orange corresponding to peaks A, B, and C, respectively. Structure and transition dipole moment orientation[69] of PIC shown in inset of (b).

The results of the in situ absorption measurements during molecular aggregation are shown in Figure 3.1. There are three distinct stages of film formation apparent in Figure 3.1a, which we term the solution, intermediate, and final stages. During the solution stage, from 0 s to 80 s, the spectrum is consistent with the spectrum of a dilute solution of PIC. The spectrum changes drastically at 80 s to exhibit three distinct peaks, which we label as peaks A, B, and C in order of ascending energy, as shown in Figure 3.1b. During the solution stage, the intensity of the peaks decreases with increasing

energy (A > B > C), which is typical for a dilute solution of semiconducting organic molecules. After the transition to the intermediate stage at 80 s, peak C becomes more intense than peak B, peak A becomes much more intense, and there is an overall red shift of the spectrum, when compared to the solution stage. The energy and intensity of the peaks remains steady until the transition to the final state at 350 s, as shown in Figure 3.1c,d. There is overall a slight blue shift in the spectrum in the final stage, and the intensity of the peaks revert to the ordering seen in the solution stage. The intense red peak is still present in the final stage, though the peak decreases slightly in intensity and becomes slightly broader.

3.2 – Metrics Error for PIC Spectrum

The changes in peak energies and intensities are indicative of a change in the electronic and physical structure of chromophores present during film formation. These changes are due to the formation of aggregates as solvent evaporates during film formation. The overall goal of this dissertation is to determine how the structure of aggregates changes during film formation using the Holstein Hamiltonian shown in Chapter 2. In order to quickly simulate the spectra from an in situ absorption measurement, the simulated spectra need to be quickly compared to the experimental spectra. This is achieved by comparing key spectral features in a simulated spectrum to an experimental spectrum, as described in Chapter 2. For the intermediate and final stages of PIC, the energies and intensities of peaks A, B, and C are used to determine the metrics error between simulated and experimental spectra. As explained further below, the energy and intensity of peaks A and C will be used to narrow down the possible sets of parameters for the simulated spectra. As such, we consider the absolute energy and

intensity of these two peaks in the metrics error calculation, while the energy and intensity of peak B relative to peak C is used in this calculation, as shown in Eq. 3.1, where variables are as described in Chapter 2.

$$e_m = \left(\frac{w_{E_A}\left|E_A - E_A^*\right|}{E_A^*}\right)^2 + \left(\frac{w_{I_A}\left|I_A - I_A^*\right|}{I_A^*}\right)^2 + \left(\frac{w_{E_C-E_B}\left|\left(E_C - E_B\right) - \left(E_C^* - E_B^*\right)\right|}{\left(E_C^* - E_B^*\right)}\right)^2 + \left(\frac{w_{I_B/I_C}\left|I_B/I_C - I_B^*/I_C^*\right|}{I_B^*/I_C^*}\right)^2 + \left(\frac{w_{E_C}\left|E_C - E_C^*\right|}{E_C^*}\right)^2 + \left(\frac{w_{I_C}\left|I_C - I_C^*\right|}{I_C^*}\right)^2 \quad (3.1)$$

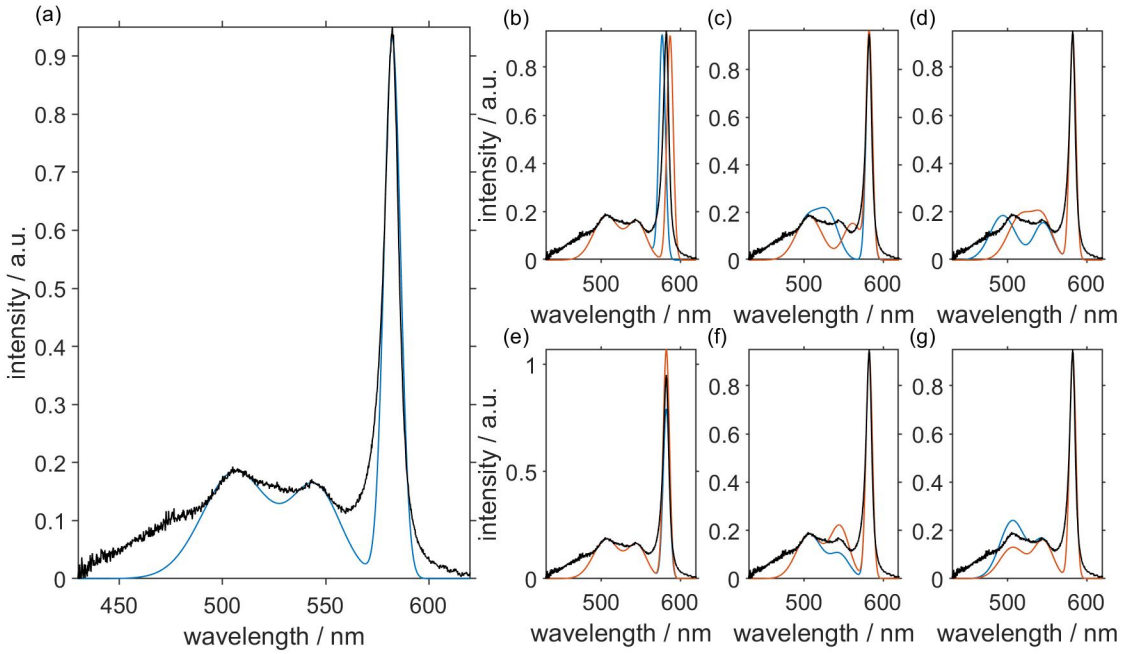

Figure 3.2. (a) The peak positions and intensities of an experimentally measured absorption spectrum (black) were fit using three Gaussians (blue). The six spectrum metrics, (b) E_A, (c) E_B-E_C, (d) E_C, (e) I_A, (f) I_B/I_C, and (g) I_C, were each changed while the other five metrics were held constant at their best-fit value. The varied metric was changed until the resulting spectrum had visibly poor agreement with the experimental spectrum. The upper (blue) and lower (orange) bounds for each metric are shown, overlaid with the experimental spectrum (black). The value of w_m was set such that a metrics error of 3 would result at each of these bounds, when all other metrics were held at their best-fit value.

A percent error of 1%-3% for the peak energies and 10%-30% for the peak intensities were chosen as a limit for the acceptable error for a simulated spectrum to have good agreement with the experimental spectrum. Weights for the metrics were

chosen such that if one metric was at its maximum percent error, as shown in Figure 3.2, the total metrics error would be three. The upper and lower bounds of acceptable metrics are shown in Figure 3.2.

3.3 – Mixture of Aggregates to Explain PIC Spectrum

While the appearance of the intense red peak in the intermediate and final stages is consistent with the formation of a J-aggregate, the change in the relative peak intensities is not consistent with either an H- or J-aggregate. As shown in Chapter 2, the intensity of absorption peaks in a J-aggregate decreases with increasing energy. For an H-aggregate, the intensity of peaks tends to first increase with increasing energy, then decrease. Based on the relative intensity of the peaks, the intermediate stage likely has a combination of H- and J-aggregates, with a J-aggregate being responsible for the intense peak A, an H-aggregate being responsible for peak C, and intensity from both the H- and J-aggregates contributing to peak B. To further justify using a mixture of aggregates, a spectrum from the intermediate stage was modeled using a single aggregate. A collection of spectra was simulated using a grid of values for the size of the aggregate ($1 \leq n \leq 10$), the Coulombic coupling values ($-1050\ \text{cm}^{-1} \leq J \leq 1050\ \text{cm}^{-1}$, in steps of $30\ \text{cm}^{-1}$), the Huang-Rhys factor ($0.2 \leq \lambda^2 \leq 1.0$, in steps of 0.05), and the angle between adjacent monomer units ($0° \leq \theta \leq 90°$, in steps of 15°). The spectrum with the best agreement had a metrics error of 11.9, and parameters for the aggregate size, λ^2, J, and θ of 6, 0.5, $-1050\ \text{cm}^{-1}$, and 0°, as shown in Figure 3.3. The poor agreement between the spectrum from the intermediate stage and the simulated single aggregate spectrum further motivates the use of two aggregates to model experimental spectra.

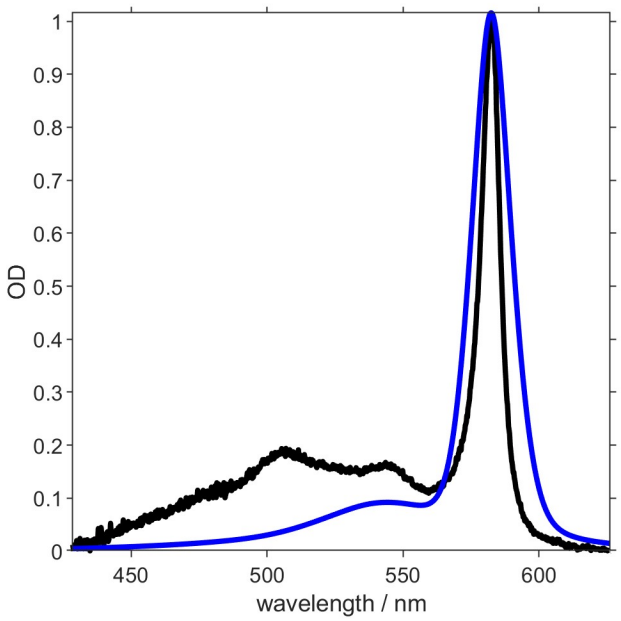

Figure 3.3. The simulated spectrum (blue) that best agrees with the experimental spectrum (black) during the intermediate stage. The calculated spectrum has an error of 11.9, and parameters for the aggregate size, λ^2, J, and θ of 6, 0.5, -1050 cm^{-1}, and 0°.

3.4 – Charge Transfer Aggregates

It is also possible that a single type of aggregate could fit the experimental spectrum if we also include charge transfer states. To investigate this possibility, absorption spectra of aggregates that exhibit both Frenkel excitons and charge transfer (CT) states were calculated for aggregates ranging from 1 to 5 molecules. The Hamiltonian for these states is a combination of CT and Frenkel components, as shown in Eq. 3.2,

$$\begin{aligned}\hat{H} = {} & \varepsilon_0 \sum_{n=1}^{N} a_n^{\dagger} a_n + \omega_0 \sum_{n=1}^{N} b_n^{\dagger} b_n + \sum_{n=1}^{N} \sum_{m \neq n}^{N-1} J_{m,n} (a_m^{\dagger} a_n + a_m a_n^{\dagger}) + \omega_0 \sum_{n=1}^{N} a_n^{\dagger} a_n \left[\lambda \left(b_n^{\dagger} + b_n \right) + \lambda^2 \right] \\ & + \sum_{n=1}^{N} \left\{ t_e c_n^{\dagger} c_{n+1} + t_h d_n^{\dagger} d_{n+1} \right\} - \sum_{n=1}^{N} \sum_{s \neq 0} V_{CT}(x) c_n^{\dagger} c_n d_{n+s}^{\dagger} d_{n+s} \\ & + \omega_0 \sum_{n=1}^{N} \sum_{s \neq 0} \left\{ \lambda_- \left(b_n^{\dagger} + b_n \right) + \lambda_+ \left(b_{n+s}^{\dagger} + b_{n+s} \right) + \lambda_-^2 + \lambda_+^2 \right\} \times c_n^{\dagger} c_n d_{n+s}^{\dagger} d_{n+s}\end{aligned} \tag{3.2}$$

where $c_n^\dagger(c_n)$ and $d_n^\dagger(d_n)$ are the creation (annihilation) operators for the electron and hole, respectively. A multiparticle site-based basis set (Eq. 3.3), consisting of one- and two-particle FE states and two-particle CT states is used,

$$\left|\psi^{(\alpha)}\right\rangle = \sum_{n,v} c_{n,v}^{(\alpha)} \left|n,v\right\rangle_{FE} + \sum_{n,v}\sum_{n',v'} c_{n,v;n',v'}^{(\alpha)} \left|n,v;n',v'\right\rangle_{FE} + \sum_{n_+,v_+}\sum_{n_-,v_-} c_{n_+,v_+;n_-,v_-}^{(\alpha)} \left|n_+,v_+;n_-,v_-\right\rangle_{CT} \quad (3.3)$$

with a vibronic excitation on molecule n with v vibrational quanta, an additional v' vibrational quanta on molecule n', a hole with v_+ vibrational quanta on molecule n_+, and an electron with v_- vibrational quanta on molecule n_-.

Similar to the H- and J-aggregate calculations, a grid of parameters for the CT states were calculated, varying the electron and hole transfer integrals ($-100\ \text{cm}^{-1} \le t_e, t_h \le 100^{-1}$ in steps of 25 cm^{-1}), Huang-Rhys factors for the electron and hole ($0.3 \le \lambda^2_-, \lambda^2_+ \le 1.5$ in steps of 0.3), and electrostatic potential energy between nearest neighbors ($100 \le V_{CT}(x) \le 2000\ \text{cm}^{-1}$ in steps of 100 cm^{-1}), where x is the distance between adjacent molecules. These CT parameters are in addition to Frenkel exciton (FE) parameters, where the Coulombic coupling ($-1050\ \text{cm}^{-1} \le J \le 0\ \text{cm}^{-1}$ in steps of 250 cm^{-1}), Huang-Rhys factor for the exciton ($0 \le \lambda^2 \le 1.0$ in steps of 0.15), and aggregate size ($1 \le n \le 5$) were varied.

Mean-squared error was used to determine the agreement between an experimental spectrum and simulated spectra. Figure 3.4 shows the spectrum with the smallest error. Compared to the combination of H- and J-aggregates, the best-fit spectrum with a single aggregate type and CT states shows very poor agreement to the experimental spectrum. Thus, even with the addition of CT states, a single electronic coupling value is not sufficient to fit the experimental spectrum, and a second coupling value must be considered.

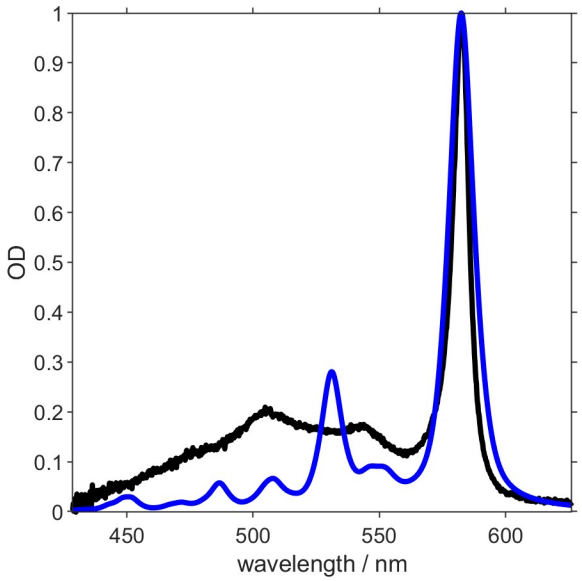

Figure 3.4. Experimental (black) and calculated spectrum with CT states using a single aggregate (blue). The parameters for this spectrum are n = 5, ε_0 = 19000 cm^{-1}, ω_0 = 1370 cm^{-1}, J = -1050 cm^{-1}, λ^2 = 0.9, $V_{CT}(x)$ = 600/s cm^{-1}, t_e = 25 cm^{-1}, t_h = -100 cm^{-1}, λ^2_- = 1.5, λ^2_+ = 0.9.

3.5 – Grid Formation and Fitting of Simulated Spectra

While it would be possible to evaluate the metrics error for every combination of parameters for two aggregates, a large number of the resulting spectra would not have good agreement with experimental spectra, as shown below. In order to make the process of simulating the large number of spectra from the in situ measurement time efficient, we need to limit the total number of calculations. In this section, the construction of two grids that will be used to generate simulated spectra will be outlined, as well as how the total number of spectra that need to be evaluated are limited based on the experimental spectrum. Finally, I will go over the metrics error cutoff that is used to further limit the number of spectra that undergo a least-squares fit to optimize the agreement between experimental and simulated spectra.

Two 10 x 71 x 17 grids were generated using a range of aggregate sizes (n_H, n_J = 1-10), Coulombic couplings (J_H, J_J = -1050 cm^{-1} to 1050 cm^{-1} in steps of 30 cm^{-1}), and

Huang-Rhys factors (λ^2 = 0.2 to 1.0 in steps of 0.05). One of these grids was used to generate spectra for what we assume is a J-aggregate, and the other was used to generate spectra for an H-aggregate. The number of molecules in an aggregate was limited to 10, as longer aggregates show little change in spectral features. For similar reasons, the maximum number of vibrational quanta was limited to 4. Sets of parameters that generate pairs of simulated aggregate spectra that, when summed, have reasonably close agreement to the experimental spectrum will be used as initial guesses for a fit. This ensures that the entire parameter space is considered and that all possible sets of parameters that can yield a good fit of the measured spectra are found.

To consider all possible binary mixtures of H- and J-aggregates, each calculated H-aggregate spectrum must be paired to each calculated J-aggregate spectrum, where λ^2 is assumed to be the same for both aggregates, resulting in a 10 x 10 x 71 x 71 x 17 grid of calculated spectra. Pairing of H- and J-aggregate spectra requires a significant fraction of computational time. This computational cost is reduced by eliminating some sets of parameters by comparing the energies (E) and intensities (I) of peaks A, B, and C in Figure 3.1, with those of the vibronic progression in simulated spectra. We denote the experimentally measured peak energies and intensities with an asterisk and letter (E^*_A, I^*_A, etc.), the energy and intensity of peaks in individual simulated H- and J-aggregate spectra with numbers corresponding to vibronic transitions ($E_{0\text{-}0}$, $I_{0\text{-}0}$, etc.), and the energies and intensities of peaks in the sum of the simulated H- and J-aggregate spectra with letters (E_A, I_A, etc.).

To limit the number of H- and J-aggregate spectra that must be paired, a few assumptions are made. First, we assume the intensity of peak A arises from the J-

aggregate, due to its red-shifted and intense peak, characteristic of J-aggregates. Similarly, we assume peak C arises from the H-aggregate spectrum, as H-aggregates can have $I_{0\text{-}1}$ that is more intense than $I_{0\text{-}0}$, whereas the intensity of the higher energy vibronic peaks decreases for J-aggregates. The calculated H-aggregate spectra that could possibly contribute to the measured spectra are limited by considering only parameter sets that yield $I_{0\text{-}0}/I_{0\text{-}1}$ that are smaller than the largest experimental I^*_B/I^*_C. While we assume intensity of peak C mostly comes from the H-aggregate spectrum, peak B could have contributions from both H- and J-aggregates. Because of this, I^*_B/I^*_C can only be larger than $I_{0\text{-}0}/I_{0\text{-}1}$ in the H-aggregate alone. Similarly, only parameter sets that yield J-aggregate spectra with $I_{0\text{-}0}/I_{0\text{-}1}$ greater than the smallest I^*_A/I^*_B are retained.

To account for the substantial red-shift in the evolving experimental aggregate spectra after the J-aggregate peak first forms at 80 s, we consider a solution-to-crystal shift. The shift is due to increasing stabilization of the electronic states from solution to crystal, like a gas-to-crystal shift. The solution-to-crystal shift is calculated using each calculated H-aggregate spectrum, such that $E_{0\text{-}1}$ of the simulated H-aggregate spectrum coincides with E^*_C, as peak C should have the smallest contribution from the J-aggregates of the three analyzed peaks. Each remaining J-aggregate spectrum is paired with an H-aggregate and the solution-to-crystal shift is applied. If the shifted $E_{0\text{-}0}$ does not lie within an acceptable error of E^*_A, that set of parameters is discarded. All the reductions described above are performed once for the entire set of measured spectra to reduce the original 10 x 10 x 71 x 71 x 17 grid of possible parameter sets by > 99%. To finish constructing the simulated spectrum, the intensity of the H-aggregate spectrum is scaled

to I^*_C, the J-aggregate spectrum is scaled to I^*_A, and the two spectra are summed together, as shown in Eq. 3.4.

$$A_{total}(\omega) = I_J A_J(\omega) + I_H A_H(\omega) \tag{3.4}$$

The metrics error is calculated using Eq. 3.1 for each of the summed spectra generated by the remaining sets of parameters, and those with an error of three or less undergo a least-squares fit for the values of J_H, J_J, λ^2, I_H, and I_J, with the Hamiltonian recalculated for each iteration of the fit. The solution-to-crystal shift is recalculated and applied to the H- and J-aggregate eigenvalues and a spectrum is generated. An example of the result of this process is shown in Figure 3.5. The green and blue stripe in Figure 3.5a corresponds to the sets of parameters that met all of the criteria described above. To further decrease the total computation time, fitting is only performed for parameter sets that result in a spectrum with a metrics error of less than three. Parameter sets that are not fit are shown in blue in Figure 3.5a. A comparison with Figure 3.5b shows that the fitting procedure results in calculated spectra with a smaller metrics error.

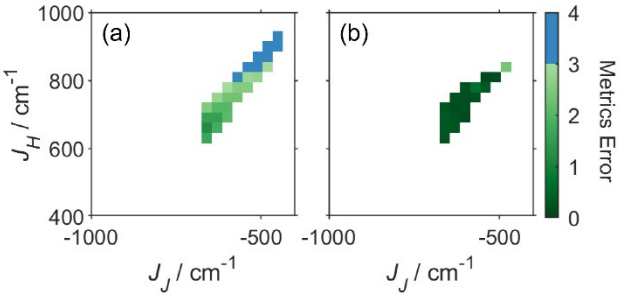

Figure 3.5. Error in peak metrics between calculated spectra and an experimental spectrum measured at 277.5 s. (a) Metrics error for spectra calculated using various J_J and J_H values where n_H, n_J, and λ^2 are 2, 10, and 0.4, respectively. Sets of parameters that result in a metrics error above three are not fit to the experimental spectrum and are shown in blue. (b) The metrics error after fitting by optimizing the values of J_J, J_H, λ^2, and scaling for the H- and J-aggregate spectra to minimize the metrics error.

3.6 – Results

Figure 3.6a shows the spectrum calculated using one set of parameters as an initial guess and the spectrum calculated after those parameters are optimized using the fitting procedure, both overlaid on the experimental spectrum measured at 280 s. The spectra calculated using the initial guess and the fitted parameters result in a metrics error of 2.37 and 0.07, respectively, using Eq. 3.1. An analogous example is presented in Figure 3.6b for an experimental spectrum measured at 405 s, with a metrics error of 2.94 and 0.09 for the spectra calculated using the initial guess and final fit parameters, respectively.

Calculated spectra with error values less than 0.5 are virtually indistinguishable by eye. When all the initial guess values are optimized using the fitting procedure, many parameter sets yield calculated spectra with error values < 0.5 and are considered good fits. Starting from 4379 and 5226 sets of initial parameter values that met the metrics error cutoff, applying the fitting procedure yields 1112 and 1696 good fits for the measured spectra shown in Figure 3.6a,b, respectively.

Histograms of the parameters that produce good fits are shown in Figure 3.6c,e,g and Figure 3.6d,f,h, respectively. There are only subtle differences between the fit J- and H-aggregate sizes (n_J and n_H) for the intermediate and final spectra, but a clear change is observed in the coupling values for the J- and H-aggregates (J_J and J_H), with the coupling values fit to the intermediate spectrum being larger in magnitude than the coupling values fit to the final spectrum. The values for λ^2 become larger in the final stage of aggregation, which will be further discussed below.

All sets of initial guesses that met the error cutoff were fit for the series of spectra measured in situ during film formation. The evolution of the distribution of parameters that produce good fits is shown in Figure 3.7. The distribution of parameters of well-fit spectra does not change significantly during the intermediate stage of aggregation between 80 s and ~300 s. At this point, the J_J value that most frequently results in a good fit starts to decrease in magnitude from ~-600 cm^{-1} at 300 s to ~-500 cm^{-1} at 355 s. Similar changes are found for the values of J_H and λ^2 that most often yield good fits, though J_H and λ^2 change more quickly, primarily between 345 s and 355 s.

Interestingly, there are two subsets of parameters that yield good fits, with one being much more populated than the other. This can be seen in the histograms for J_J, and J_H, where the less populated subset of parameters has larger magnitude couplings. The two subsets of J_H values that produce good fits are isolated and the resulting histograms are shown in Figure 3.8 and Figure 3.9. The subset with larger J_H values, shown in Figure 3.8, is entirely comprised of H-aggregate dimers, while most of the parameter sets that generated good fits required smaller J_H values, shown in Figure 3.9, and H-aggregate dimers are not present in this subset. Additional DFT calculations could determine whether feasible dimer orientations exist that yield these large coupling values.

The value of λ^2 is much smaller than the monomer value of 0.605 in the histograms for all spectra measured after the formation of aggregates. After the transition from the intermediate stage to the final stage, the decrease in the magnitude of the J_J and J_H values coincides with an increase in λ^2. This is consistent with electronic energy transfer theory,[110] which predicts that a larger magnitude electronic coupling will result in

smaller nuclear displacements in symmetric vibrational modes of molecules in an aggregate upon excitation, resulting in a smaller λ^2.

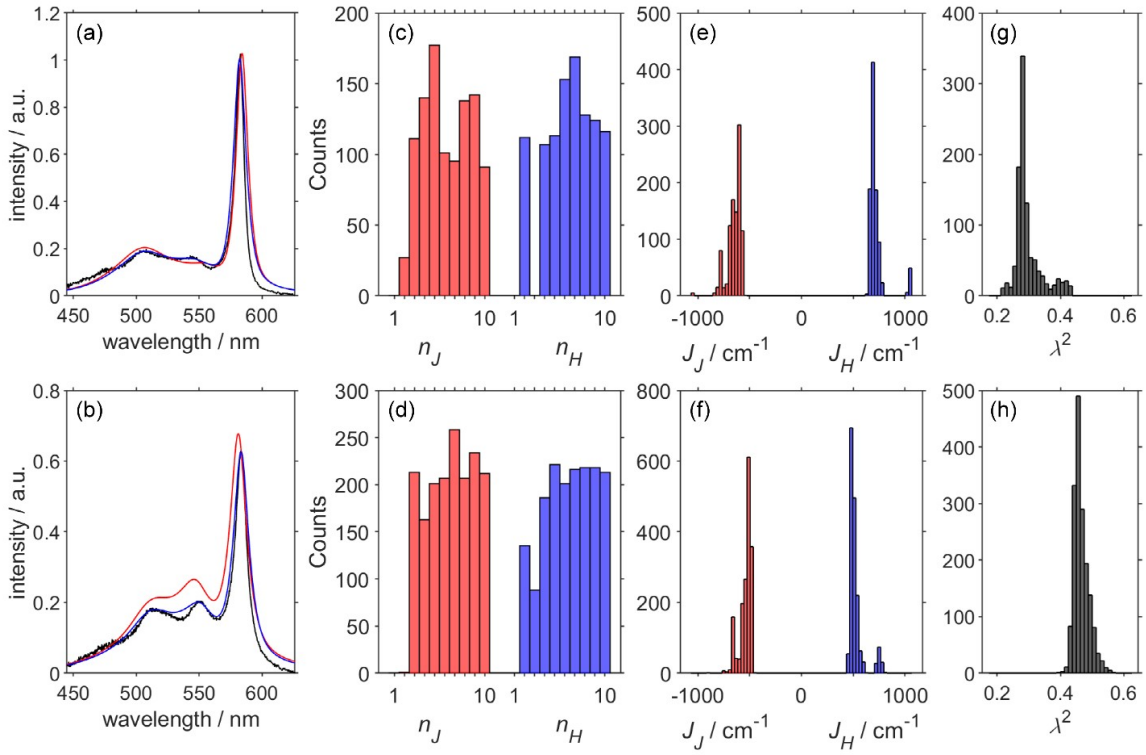

Figure 3.6. Fits of PIC spectra measured during the intermediate (top) and final (bottom) stages of film formation. (a, b) Measured spectrum (black), spectrum calculated with an initial guess (red), and fit spectrum (blue). Distributions of fit values that resulted in a metrics error of < 0.5 for n_J and n_H (c, d), J_J and J_H (e, f), and λ^2 (g, h). The parameters for the initial guess (fit) parameters for the intermediate stage spectrum are $n_H = 10$, $n_J = 5$, $\lambda^2 = 0.25$ (0.27), $J_J = -600$ cm^{-1} (-650 cm^{-1}), $J_H = 780$ cm^{-1} (670 cm^{-1}), and for the final stage spectrum are $n_H = 3$, $n_J = 3$, $\lambda^2 = 0.40$ (0.44), $J_J = -690$ cm^{-1} (-695 cm^{-1}), $J_H = 510$ cm^{-1} (590 cm^{-1}).

To consider the validity of using a single value for the Huang-Rhys factor to simulate these spectra, we also used separate λ^2 values for the H- and J-aggregates. The distribution of parameters that results in simulated spectra with low error for the spectrum measured at 390 s is shown in Figure 3.10. Similar to the single λ^2 fits, there are two subsets of values of J_J and J_H that result in spectra with low error. The aggregate sizes seen in each of the sub-distributions in J_J and J_H are like those seen in the single λ^2 fits,

where the larger magnitude coupling values arise solely from dimers, as shown in Figure 3.6, though the individual distributions are different. Contrary to exciton theory, the H-aggregates with larger coupling values result in a λ^2 that is closer to that of the PIC monomer than the λ^2 from the aggregates with smaller coupling values. As discussed further below, this implies that it is unlikely that the two J_H distributions exist at the same time, though both fit the spectrum equally well. The opposite is true for the J-aggregates, where the overall distribution of λ^2 values shift to slightly smaller values with larger coupling values.

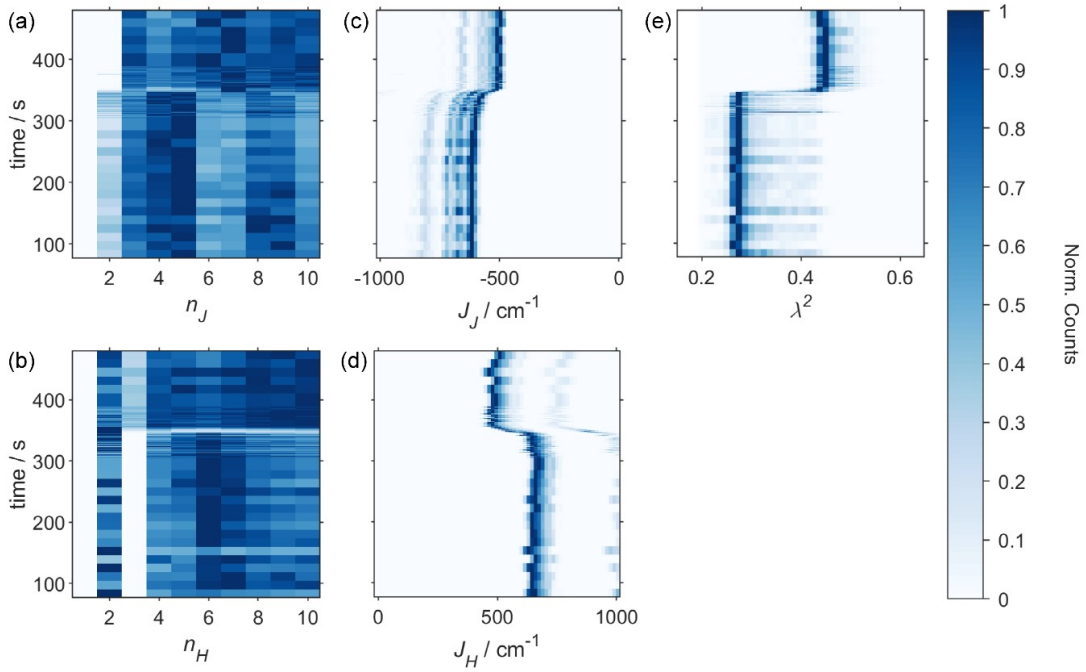

Figure 3.7. Time resolved normalized histograms of fit values for calculated spectra that have an error of < 0.5 for n_J and n_H (a, b), J_J and J_H (c, d), and λ^2 (e).

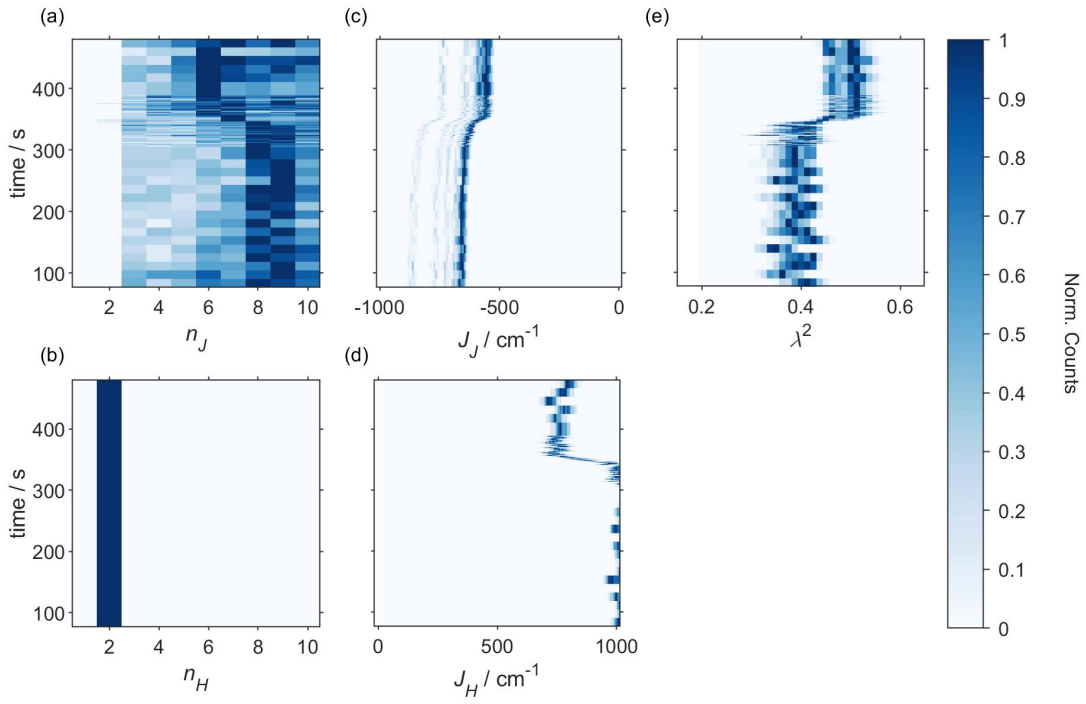

Figure 3.8. Time resolved histograms of the fit parameters for calculated spectra from Figure 3.7, only showing the larger J_H coupling values.

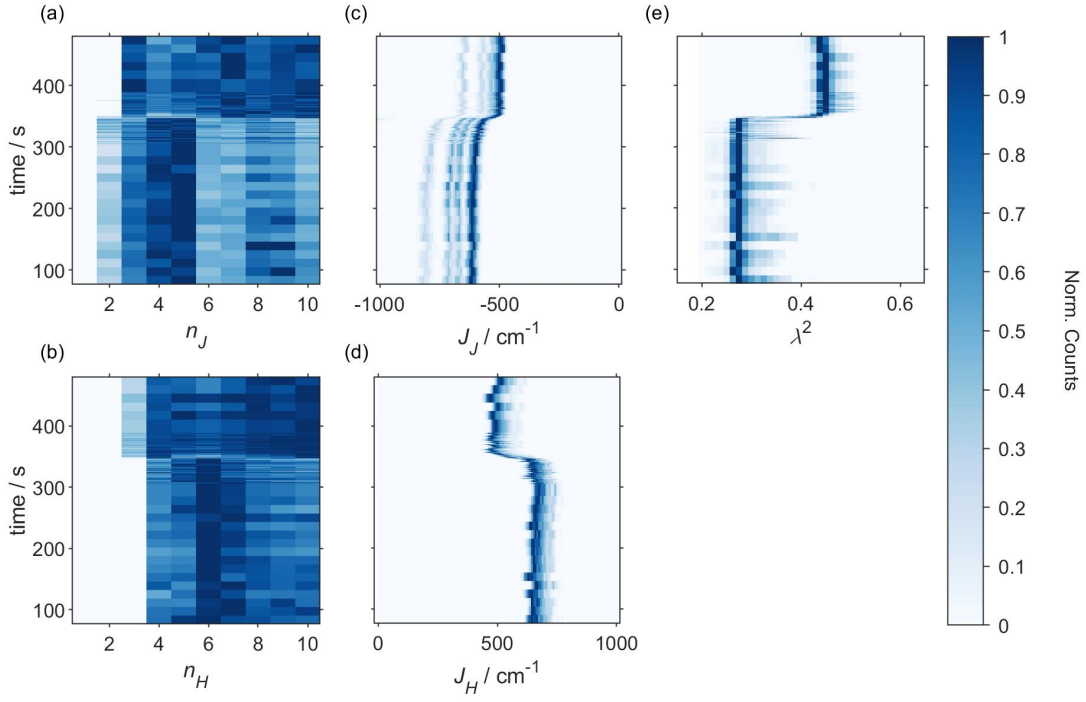

Figure 3.9. Time resolved histograms of the fit parameters for calculated spectra from Figure 3.7, but only showing the smaller J_H coupling values.

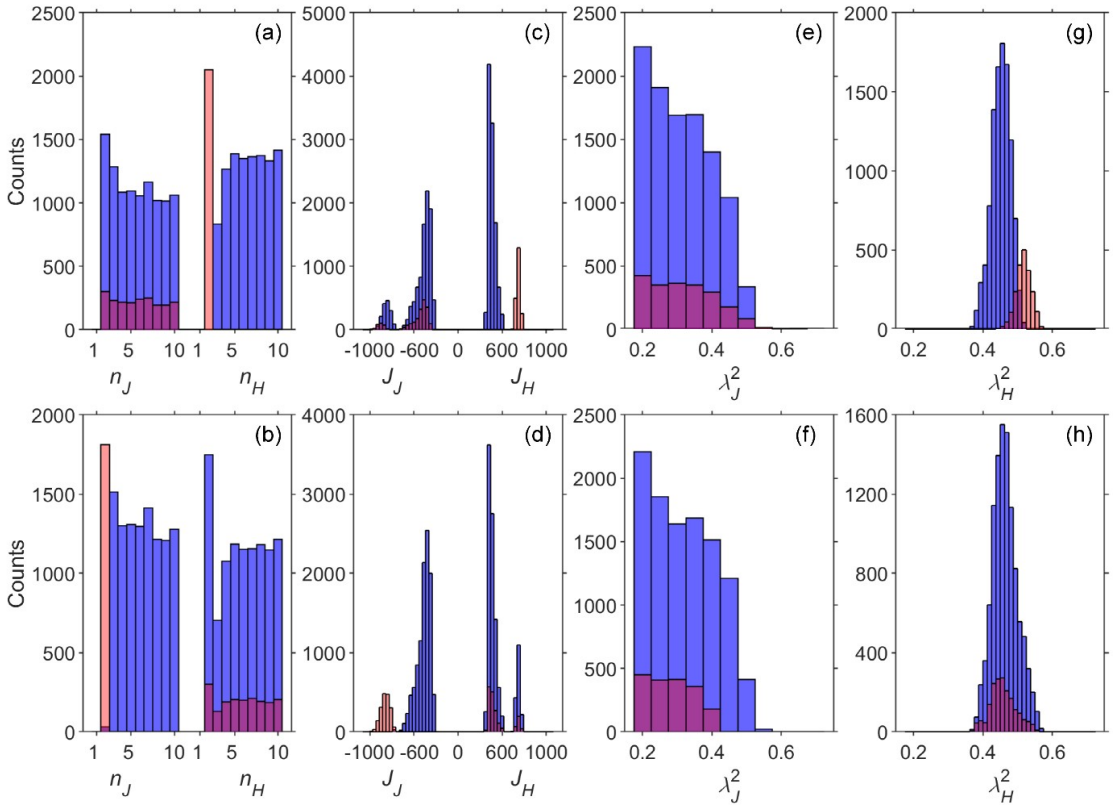

Figure 3.10. Histograms of fit parameters that result in an error < 0.5 for the PIC spectrum measured at 390 s for n_J and n_H (a, b), J_J and J_H (c, d), λ^2_J (e, f), and λ^2_H (g, h). Two Huang-Rhys factors are considered, λ^2_H and λ^2_J for the H- and J-aggregates, respectively. The top panels (a, c, e, g) show a separation in the distributions based on the J_H coupling values, with the red and blue bars corresponding to the subset of parameters that include the larger and smaller magnitude J_H coupling values, respectively. The bottom panels (b, d, f, h) show the analogous separation based on the magnitude of the J_J coupling values. Red and blue bars are overlaid to show parameters that are present in both coupling distributions.

Time resolved histograms from simulated spectra with two λ^2 values (Figure 3.11) show characteristics like those observed in Figure 3.7. Both exhibit J_J and J_H values that decrease in magnitude after the transition to the final aggregation stage, after ~355 s. The Huang-Rhys factor for the H-aggregate increases after the transition to the final aggregation stage and is similar to the single λ^2 histograms. The J-aggregate Huang-Rhys factor does not seem to change from the intermediate to final stage of aggregation.

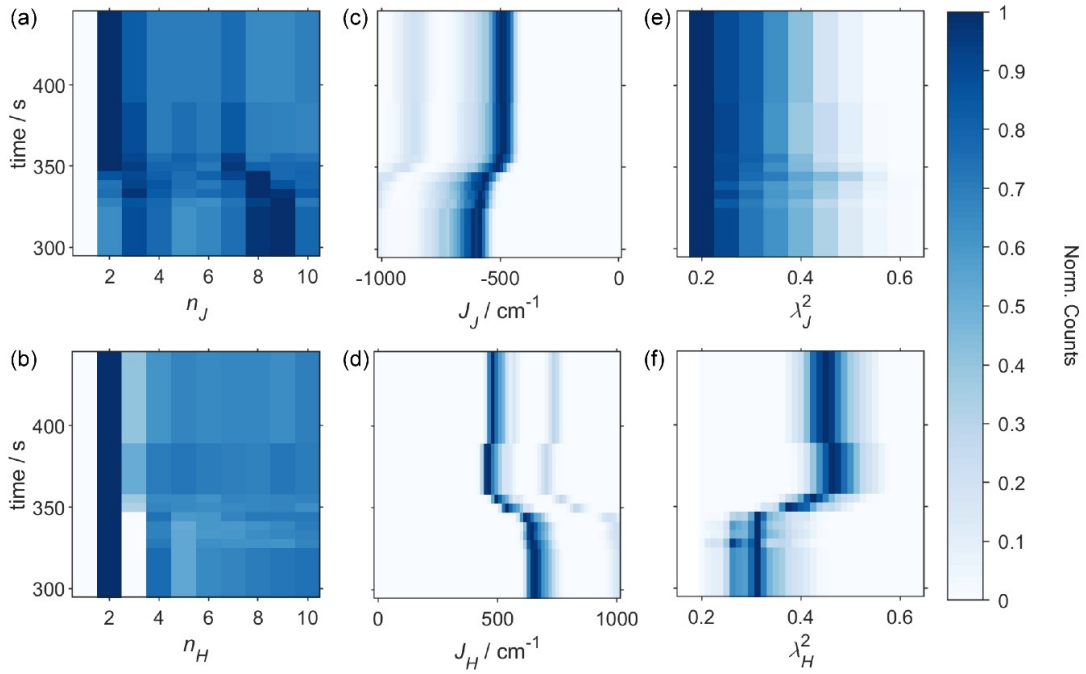

Figure 3.11. Time resolved normalized histogram of fit parameters with error < 0.5 for n_J and n_H (a, b), J_J and J_H (c, d), and λ^2_J and λ^2_H (e, f) when using separate Huang-Rhys factors for the H- and J-aggregates. The y-axis focuses on the transition from the intermediate stage to the final stage.

3.7 – 2D Brickwork Aggregates as a Possible Alternative to Mixture of Aggregates

The result showing that the absorption spectrum of PIC aggregates can be fit to a mixture of H- and J-aggregates raises the question of whether the measured spectra could also arise from two-dimensional aggregates with electronic couplings that result in spectral characteristics of both H- and J-aggregates. Two-dimensional (2D) aggregates can take many forms such as bricklayer or herringbone structures, and the overall structure dictates the sign and magnitude of electronic coupling between neighboring molecules. When the TDMs of all molecules in the aggregate are colinear, the

assumption in this work, a brick-layer structure is possible. Given a particular molecular width, a, and aspect ratio, A, the arrangement of a 2D aggregate can be defined by the slip, s, between layers of molecules, as illustrated in Figure 3.12a. The Coulombic coupling in 2D aggregates can be estimated using the electrostatic interaction between two dipoles,

$$J_{nm} = C\frac{\vec{\mu}_n \cdot \vec{\mu}_m - 3(\vec{\mu}_n \cdot \hat{r}_{nm})(\vec{\mu}_m \cdot \hat{r}_{nm})}{r_{nm}^3} \tag{3.5}$$

where $\hat{\mu}_n$ is the transition dipole vector for molecule n, $\hat{r}_{nm}$ is the unit vector from the center of mass of molecule n to molecule m, r_{nm} is the distance between the two centers of mass, and C is a constant that scales the magnitude of the coupling.

Molecules aligned along the long axis of the molecule will have negative coupling and have the properties of a J-aggregate. Relative to the central molecule represented by the white block in Figure 3.12a, coupling to the molecules represented by red blocks would result in J-aggregate coupling.

$$J_J = \frac{-2C\mu^2}{a^3A^3} \tag{3.6}$$

Along the short axis of the molecule there are two nearest neighbor molecules, shown in blue and green in Figure 3.12a. The coupling between the central molecule and each of these two molecules can be either positive or negative, depending on the slip value. This coupling is expressed as a function of the structural parameters in Eq. 3.7.

$$\begin{aligned} J_H &= \frac{C\mu^2(1-3\cos(\theta))}{(a^2+s^2A^2a^2)^{3/2}} \\ J_H &= \frac{C\mu^2\left(1-3\dfrac{s^2A^2}{1+s^2A^2}\right)}{a^3(1+s^2A^2)^{3/2}} \end{aligned} \tag{3.7}$$

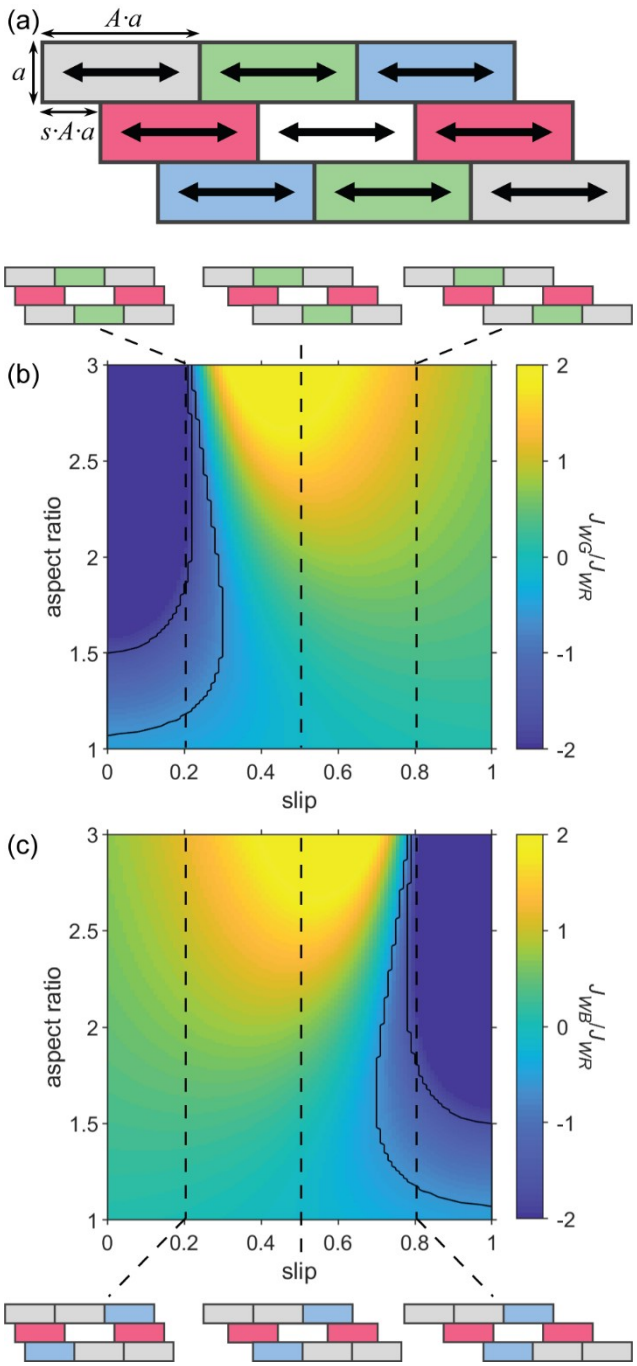

Figure 3.12. (a) Generalized brickwork structure for a 2D aggregate, where the aggregate is defined by the length of the short axis of the molecule, a, the aspect ratio of the molecule, A, and the slip between layers, s, where s is a value that ranges from 0 to 1. Black arrows show the orientation of the transition dipole moments. Red molecules have a negative coupling with the white molecule. Green and blue molecules may have either negative or positive coupling with the white molecule, depending on the slip. Calculated ratio of (b) J_{WG} and J_{WR} and (c) J_{WB} and J_{WR} values using electrostatic dipole-dipole interactions. Coupling was calculated relative to a constant J_{WR} of -500 cm^{-1}. Cartoons show molecular arrangement using different slip values.

We set the J-aggregate coupling between the white and red molecules (J_{WR}) to be -500 cm^{-1} and used Eq. 3.7 to calculate the coupling values between the white and green molecules (J_{WG}) using a range of aspect ratios and slip values. The ratio of J_{WR} (which is always negative) and J_{WG} (which may be either positive or negative) is displayed in Figure 3.12b. This ratio was found to be independent of the size of the molecule, and only depend on the angle between dipoles, which is affected by the slip and aspect ratio. The value of J_{WG}/J_{WR} was compared to the ratio between J_H and J_J values in the simulated spectra that resulted in good agreement with experimental spectra. Values of J_H/J_J from well-fit simulated spectra fell within a window of -1.695 and -0.625.

The combinations of aspect ratio and slip value that result in a J_{WG}/J_{WR} in this window are outlined in black in Figure 3.12b, and analogous calculations for J_{WB}/J_{WR} are shown in Figure 3.12c. Based on the molecular geometry of PIC, the aspect ratio is likely between 2 and 3, so a small range of brick-layer structures with $s \approx 0.2$-0.3 and 0.7-0.8 could yield a ratio of coupling values that agree with those in calculated spectra that well-fit the experimental spectra. However, these so-called "HJ-aggregates"[111–113] do not exhibit absorption spectra that are a simple weighted sum of its constituent H- and J-aggregates, but instead will appear similar to spectra with a single dominant Coulombic coupling value. To illustrate this, we calculated an absorption spectrum with the simulation parameters that yielded a good fit of a final stage spectrum in Figure 3.6b, but used the Hamiltonian in Eq. 2.5 for a 3-by-3 brick-layer HJ-aggregate with a 1-particle approximation, Eq. 2.2. The linear aggregate has non-zero coupling only between nearest neighbor molecules in one direction, whereas the 3-by-3 brick-layer aggregate has non-zero coupling between adjacent molecules in two directions.

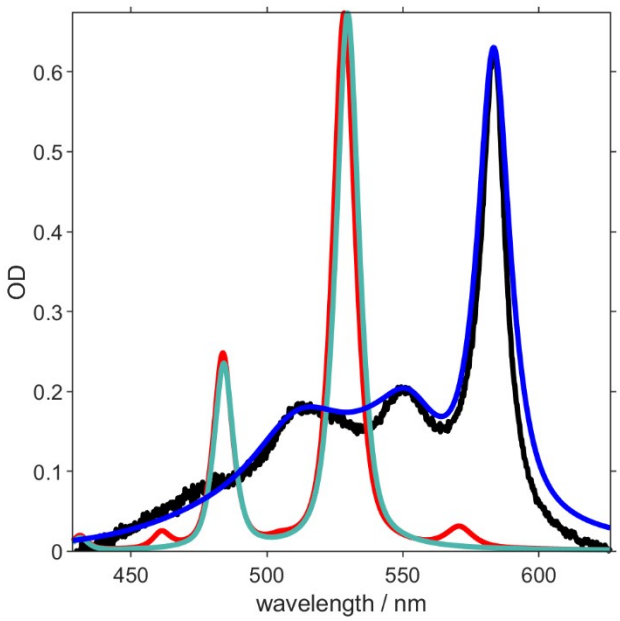

Figure 3.13. Comparison of simulated absorption spectra calculated using the same electronic coupling values for a brick-layer aggregate and a sum of linear aggregates. Calculated spectrum for a weighted sum of linear H- and J-aggregates (blue) that best-fits the measured absorption spectrum at 405 s (black), calculated using the parameters n_H = 3, n_J = 3, λ^2 = 0.44, J_J = -695 cm^{-1}, J_H = 590 cm^{-1}. The calculated spectrum for a 3-by-3 aggregate using parameters λ^2 = 0.44, J_J = -695 cm^{-1}, J_H = 590 cm^{-1} (red). Calculated spectrum for a linear trimer with parameters λ^2 = 0.44, J = -105 cm^{-1} (teal).

The calculated spectrum, Figure 3.13, is clearly different from the calculated spectrum in Figure 3.6b which uses a weighted sum of J-aggregate and H-aggregate trimers and does not fit the experimental spectrum. The ratio of peak intensities does not

appear to be that of a mixture of H- and J-aggregates, but instead is similar to that of a linear trimer with J = -105 cm^{-1}, the sum of the two coupling values used in the simulation. Thus, we conclude that the peak intensity ratios observed in situ during PIC aggregation result from a mixture of H- and J- aggregates and not from HJ-aggregates.

3.8 – Discussion

In this chapter, we introduced a method for determining possible compositions of a mixture of PIC aggregates during the process of film formation. By focusing on the fit of spectral signatures of aggregation, spectra resulting from many combinations of J- and

H-aggregates can be compared to an experimental spectrum at low computational cost compared to other methods such as MD and DFT. As a result, dozens of experimental spectra can be simulated in a few days, unlocking the ability to monitor aggregate formation.

This method is sensitive only to optically active transitions and is really a measure of the number of molecules over which an exciton is delocalized. Modeling absorption spectra of "ideal" H- and J-aggregates can be performed using a site-based basis, as is the case in this dissertation, or can involve dressing the site-based eigenstates in an exciton basis and by assuming zero disorder, periodic boundary conditions, and translational symmetry.[81,114] By not using periodic boundary conditions arbitrarily shaped aggregates can be considered. In either case, the spectrum loses sensitivity to exciton size when delocalization extends over many molecules. We limited our calculation to aggregates up to 10 molecules in size since we observe minimal spectral changes for larger aggregates, and this limitation allows an absorption spectrum to be fit on a standard desktop computer in ~ 1 hour. Figure 3.8 indicates that the J-aggregate excitons may localize from eight or nine molecules during the intermediate stage to a dimer upon formation of the final PIC film. This type of exciton localization was also found to occur in PIC J-aggregates in a layered polymer film owing to disorder.[115] This sensitivity to the evolving structural disorder is particularly advantageous for monitoring the formation of organic films since exciton self-trapping caused by disorder is the main mechanism by which the electronic properties of a film deviate from those of an idealized bulk organic crystal.

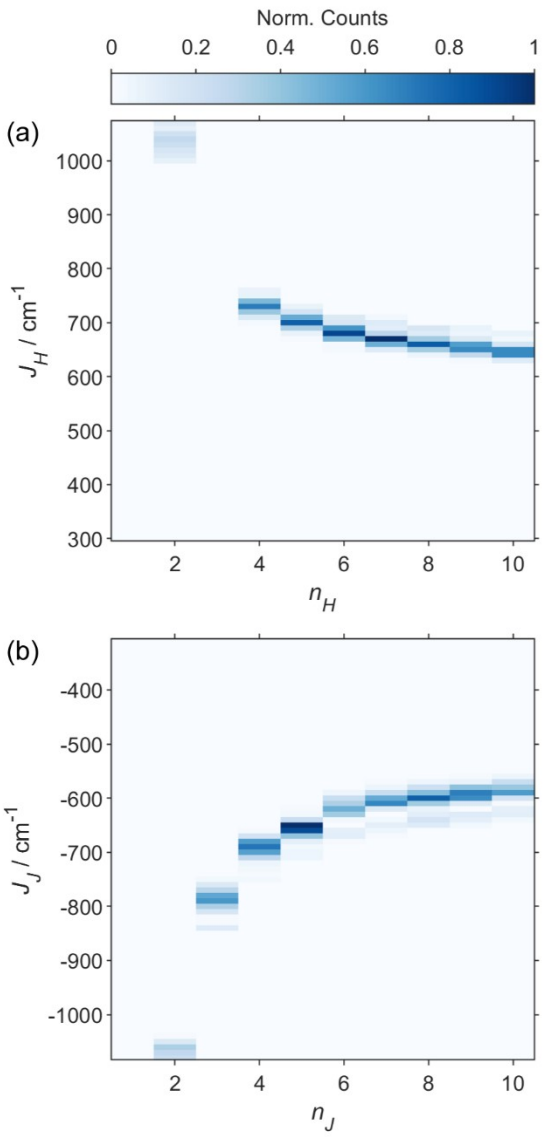

Figure 3.14. Normalized distribution of H- (a) and J-aggregate (b) sizes and corresponding coupling values for simulated spectra that fit the PIC spectrum measured at 305 s.

The softness in the fit of aggregate size also results in uncertainty in the Coulombic coupling values, as shown in Figure 3.14. Each possible aggregate size corresponds to a narrow range of Coulombic coupling values for both the H- and J-aggregates. As expected, simulated spectra with increasing aggregate size can only well-fit the experimental spectrum when the Coulombic coupling decreases. This change is most evident in smaller aggregates and begins to converge to a narrow range of coupling

values with larger aggregate sizes, as shown in Figure 3.14. The narrow range of coupling values for each size means that if computations can provide a range of possible coupling values for realistic molecular orientations, these simulations would be able to provide greater insight into the size of the aggregate. For example, if there was no realistic molecular orientation that could yield a coupling value of 1000 cm^{-1}, the possibility of H-aggregate dimers could be discarded. There is no clear correlation in the size of H- and J-aggregates, as shown in Figure 3.15.

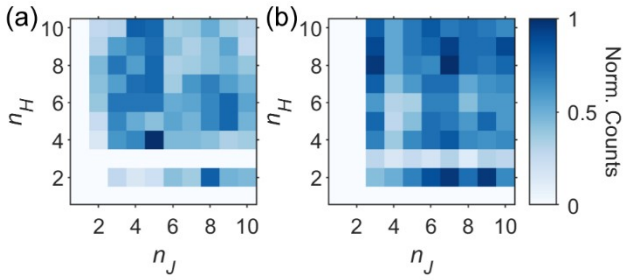

Figure 3.15. Normalized distribution of the correlation of H- and J-aggregate sizes for simulated spectra that fit the PIC spectrum measured at 305 s (a) and 470 s (b).

Both the fit broadening parameters and the calculated solution-to-crystal (STC) shifts exhibit a similar time dependence as J_J, J_H, and λ^2, with a distinct change occurring at the transition from the intermediate to the final aggregate stage, as shown in Figure 3.16 and Figure 3.17, respectively. The STC shift is ~820 cm^{-1} during the intermediate stage, but when the aggregates transition to the final film at ~355 s, the STC quickly increases to ~1150 cm^{-1}. The increase in stabilization is consistent with a decrease in degrees of freedom, as molecules are no longer able to move in solvent.[116]

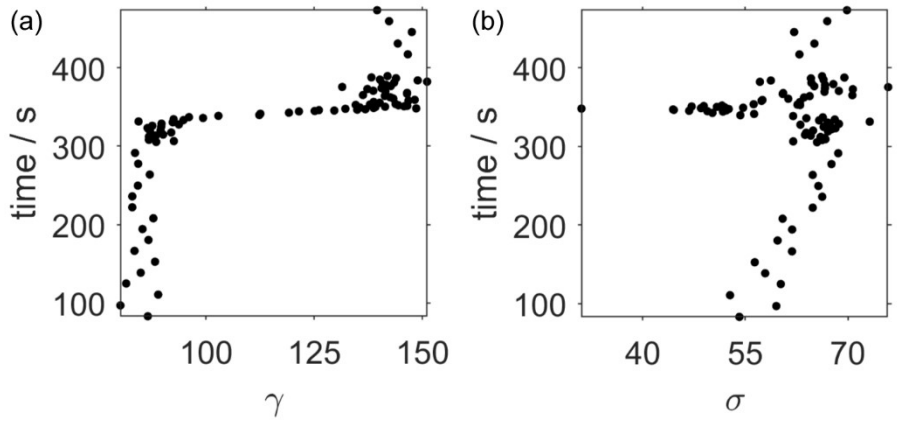

Figure 3.16. Homogeneous (a) and inhomogeneous (b) broadening determined by fitting peak A from experimental spectra. These parameters were used in calculated spectra.

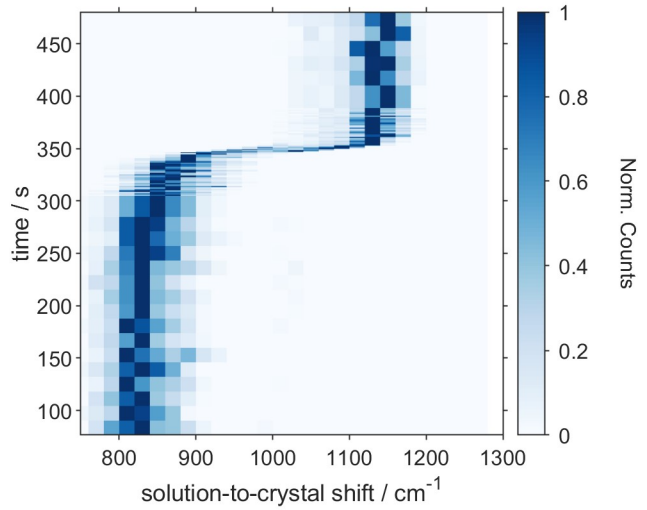

Figure 3.17. Normalized histograms of calculated STC shifts for calculated spectra with an error < 0.5. This STC red-shift was applied to calculated spectra such that $E_{0\text{-}1}$ from the H-aggregate coincided with E_C of the experimental spectrum.

The sharp STC shift increase indicates that the monomer site energies have changed as a result of a different electrostatic environment. This can affect the Huang-Rhys factor in a manner that may or may not be correlated with site energy, as has been shown in measurements of chromophores in proteins[117–119] and small molecules in glasses.[120] The Huang-Rhys factor can also change significantly with molecular geometry. In rubrene, subtle changes in bond length and dihedral angle resulted in large

variations in the Huang-Rhys factor.[121] Additionally, increased delocalization, the result of increased electronic coupling, is known to decrease the Huang-Rhys factor.[110] Considering that (1) the electrostatic environment changes significantly during aggregation, (2) PIC geometry may slightly change upon aggregation, and (3) intermolecular coupling changes during aggregation, we expect that the Huang-Rhys factor for PIC aggregates to be different from that of a monomer. Thus, it is unsurprising that our simulations of PIC absorption spectra did not result in any well-fit aggregate spectra calculated with a λ^2 value that agreed with that of the monomer. All modeled λ^2 are smaller in aggregates in all simulated spectra, consistent with theory, though the dimers seen in Figure 3.9 with large coupling values have a much larger λ^2 than the larger aggregates with smaller coupling values. It is not immediately clear which of these sets of parameters is correct, but it is unlikely that these two subsets of aggregate fits coexist since exciton theory[110] dictates that a larger coupling value should result in a smaller Huang-Rhys factor. There are no arguments in the literature explaining why the Huang-Rhys factor should be the same in both aggregates and monomers, but this assumption is commonly used.[102,114] While using different Huang-Rhys factors to model aggregates increases the computational time, spectra of PIC aggregates cannot be modeled using the Huang-Rhys factor of the monomer, Figure 3.18.

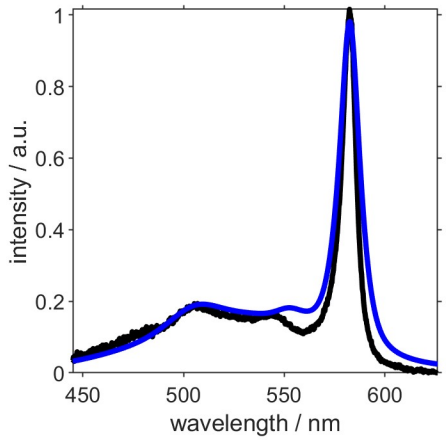

Figure 3.18. Experimental absorption spectrum for the PIC spectrum measured at 305 s (black), and best fit spectrum using the Huang-Rhys factor of the monomer in solution, λ^2 = 0.605 (blue). Other parameters are n_H = 2, n_J = 9, J_H = 960 cm^{-1}, J_J = -580 cm^{-1}. The error for this fit is 1.64, which is above the cutoff of 0.5 used to signify a well-fit spectrum. All calculated spectra with an error less than 0.5 have Huang-Rhys factors that are substantially smaller than that of the monomer. The main source of the higher error is the disagreement in the energy and intensity of peak B. The higher intensity of peak B also causes peak A to appear broader than is seen in well-fit spectra.

Aggregate spectra are modeled with an additional level of nuance by considering two Huang-Rhys factors, revealing a larger number of variable sets that generate calculated spectra that well-fit the experimental spectra. However, the overall physical picture of molecular aggregation provided by these simulations is not strongly impacted by using two separate Huang-Rhys factors. A similar bimodal distribution is seen in the coupling values as in the single λ^2 fits, with the magnitude of the coupling values decreasing during the transition from the intermediate to final stage of aggregation. The decrease in electronic coupling could be a result of a change in relative orientation or separation between molecules.

The parameters identified in this dissertation are those that could possibly fit the in situ measured absorption spectra. The point of this simulation is to quickly narrow down the possible parameter space, such that a number of other types of computations or

measurements could further refine these values. For example, the range of possible aggregate sizes and Huang Rhys factors could be limited by knowledge of possible Coulombic coupling values as determined by time-dependent DFT (TD-DFT) calculations for realistic molecular orientations. Another possibility is the structural measurement of aggregates in the static film that results from the final stage of aggregation using TEM or AFM. This would refine the possible Coulombic coupling values present in the final film, since there is a clear correlation between n_J (n_H) and J_J (J_H), as shown in Figure 3.14. Knowledge of molecular spacing within the final aggregate using XRD or GIXS would also inform the range of possible Coulombic coupling values when paired with TD-DFT calculations. Starting with the Coulombic couplings inferred from ex situ structural measurements of the final film, the evolving coupling values could be followed backwards as a function of time (e.g. in Figure 3.7). This would refine the possible aggregate parameters identified in the simulations of in situ absorption measurements presented here, and thus inform our understanding of the process of aggregate formation.

This technique of using in situ absorption measurements and simulations to monitor the formation of an organic film can be complemented with other experimental methods that allow for in situ measurement. GIWAXS can report on aggregate structure during a deposition using typical conditions for film formation, though this requires a beamline.[122,123] Single-shot transient absorption (SSTA) methods can measure the excited state dynamics of evolving material systems, such as during the deposition of a film.[124–127] Previous SSTA measurements during PIC film formation at ambient conditions revealed the development of a fast quenching process in the final film that is not present

during the intermediate stage of aggregation.[125] The measurements and analysis presented here suggest that the appearance of the quenching process is concomitant with a decrease in electronic coupling between molecules in the aggregates. In concert with the presented technique, these types of computations and measurements could yield further insight into the evolving electronic and physical structure of molecular aggregates during film formation.

CHAPTER IV

OUTLOOK

This dissertation has presented a computationally inexpensive method for modeling the absorption spectrum of a mixture of aggregates. Chapter 1 provides an overview of the importance of organic semiconducting molecules and highlighted the dependence of the electronic structure and properties on the physical structures of aggregates. A variety of deposition techniques can be employed to make organic thin films, and different methods tend to result in different film morphologies. The physical and electronic structure of molecular aggregates present in thin films can be probed with a wide array of experimental techniques. Linear absorption is used in this dissertation as it can be performed in situ during thin film deposition and provides an indirect probe for physical structure. A Holstein Hamiltonian is used to simulate absorption spectra of molecular aggregates of PIC, which has an unclear aggregate structure, despite being a well-studied molecule. Overall, Chapter 1 provides theoretical and experimental context for simulating absorption spectra and highlights the importance of modeling mixtures of aggregates of organic molecules.

Chapter 2 outlines the mathematical framework used to calculate simulated absorption spectra. Specifically, this chapter provides a guide for constructing a Holstein Hamiltonian for a monomer and a dimer. This is both to provide readers with a resource to do similar calculations and to help build intuition for how states couple together when using a two-particle approximation, which may be helpful when constructing Hamiltonians for larger aggregates. The impact of each of the parameters used to model a spectrum on the spectral features is shown. Most importantly, a computationally

inexpensive method for comparing experimental and simulated spectra is introduced. By comparing only key spectral features, the duration of error calculations can be reduced by over 99%.

Chapter 3 demonstrates that in situ absorption spectra can be modeled as a mixture of aggregates in a way that makes it computationally feasible on a typical desktop computer. PIC is the perfect model system for this, as it has well-resolved vibronic peaks whose relative intensities cannot be explained using a single kind of aggregate. The addition of charge transfer states to a model using only one type of aggregate still could not model the experimentally measured absorption spectrum of PIC. The results show there is a distribution of possible parameter sets that produce indistinguishable spectra. The distributions change during thin film deposition, implying the physical and electronic structure of the aggregates are also changing. Two-dimensional brickwork aggregates were also used to model experimental spectra but could not reproduce the results observed in the simulated spectrum of a mixture of aggregates. Finally, the results from this dissertation show that molecular aggregates cannot be accurately modeled when using the same Huang-Rhys factor as the monomer, though this is a common assumption when simulating absorption spectra of aggregates. The strategies introduced here may lead to the ability to understand more complex heterogeneous mixtures, especially if scaled to more powerful computers.

The next logical future work using this method of modeling mixtures of aggregates would be to use simulated fluorescence spectra to give additional insight into changes in the physical and electronic structure. Such work could also be performed on PIC, as it exhibits a fluorescence signal that changes in energy and intensity during the

formation of molecular aggregates. Possible aggregate structures could be determined by calculating geometries that result in the Coulombic coupling values shown here. Finally, this dissertation has only considered aggregates made from one kind of monomer. The strategies outlined here could allow mixtures of monomers to be researched, such as mixtures of electron donating and accepting molecules.

REFERENCES CITED

(1) Cox, P. A. *The Electronic Structure and Chemistry of Solids*; Oxford science publications; Oxford University Press: Oxford [Oxfordshire] ; New York, 1987.

(2) Sirringhaus, H.; Brown, P. J.; Friend, R. H.; Nielsen, M. M.; Bechgaard, K.; Langeveld-Voss, B. M. W.; Spiering, A. J. H.; Janssen, R. A. J.; Meijer, E. W.; Herwig, P.; de Leeuw, D. M. Two-Dimensional Charge Transport in Self-Organized, High-Mobility Conjugated Polymers. *Nature* **1999**, *401* (6754), 685–688. https://doi.org/10.1038/44359.

(3) Burroughes, J. H.; Bradley, D. D. C.; Brown, A. R.; Marks, R. N.; Mackay, K.; Friend, R. H.; Burns, P. L.; Holmes, A. B. Light-Emitting Diodes Based on Conjugated Polymers. *Nature* **1990**, *347* (6293), 539–541. https://doi.org/10.1038/347539a0.

(4) Bao, Z.; Dodabalapur, A.; Lovinger, A. J. Soluble and Processable Regioregular Poly(3-hexylthiophene) for Thin Film Field-effect Transistor Applications with High Mobility. *Appl. Phys. Lett.* **1996**, *69* (26), 4108–4110. https://doi.org/10.1063/1.117834.

(5) Wang, C.; Dong, H.; Hu, W.; Liu, Y.; Zhu, D. Semiconducting π-Conjugated Systems in Field-Effect Transistors: A Material Odyssey of Organic Electronics. *Chem. Rev.* **2012**, *112* (4), 2208–2267. https://doi.org/10.1021/cr100380z.

(6) Katz, H. E. Organic Molecular Solids as Thin Film Transistor Semiconductors. *J. Mater. Chem.* **1997**, *7* (3), 369–376. https://doi.org/10.1039/a605274f.

(7) Anthony, J. E. Functionalized Acenes and Heteroacenes for Organic Electronics. *Chem. Rev.* **2006**, *106* (12), 5028–5048. https://doi.org/10.1021/cr050966z.

(8) Yamada, H.; Okujima, T.; Ono, N. Organic Semiconductors Based on Small Molecules with Thermally or Photochemically Removable Groups. *Chem. Commun.* **2008**, No. 26, 2957. https://doi.org/10.1039/b719964c.

(9) Scott, J. C. Metal–Organic Interface and Charge Injection in Organic Electronic Devices. *Journal of Vacuum Science & Technology A: Vacuum, Surfaces, and Films* **2003**, *21* (3), 521–531. https://doi.org/10.1116/1.1559919.

(10) Najafov, H.; Biaggio, I.; Podzorov, V.; Calhoun, M. F.; Gershenson, M. E. Primary Photoexcitations and the Origin of the Photocurrent in Rubrene Single Crystals. *Phys. Rev. Lett.* **2006**, *96* (5), 056604. https://doi.org/10.1103/PhysRevLett.96.056604.

(11) Horowitz, P.; Hill, W. *The Art of Electronics*, 2nd ed.; Cambridge University Press: Cambridge [England] ; New York, 1989.

(12) Wang, Y.; Kumashiro, R.; Nouchi, R.; Komatsu, N.; Tanigaki, K. Influence of Interface Modifications on Carrier Mobilities in Rubrene Single Crystal Ambipolar Field-Effect Transistors. *Journal of Applied Physics* **2009**, *105* (12), 124912. https://doi.org/10.1063/1.3153946.

(13) Tan, L.; Jiang, W.; Jiang, L.; Jiang, S.; Wang, Z.; Yan, S.; Hu, W. Single Crystalline Microribbons of Perylo[1,12-b,c,d]Selenophene for High Performance Transistors. *Appl. Phys. Lett.* **2009**, *94* (15), 153306. https://doi.org/10.1063/1.3120769.

(14) Ebata, H.; Izawa, T.; Miyazaki, E.; Takimiya, K.; Ikeda, M.; Kuwabara, H.; Yui, T. Highly Soluble [1]Benzothieno[3,2- *b*]Benzothiophene (BTBT) Derivatives for High-Performance, Solution-Processed Organic Field-Effect Transistors. *J. Am. Chem. Soc.* **2007**, *129* (51), 15732–15733. https://doi.org/10.1021/ja074841i.

(15) Kelley, T. W.; Muyres, D. V.; Baude, P. F.; Smith, T. P.; Jones, T. D. High Performance Organic Thin Film Transistors. *MRS Proc.* **2003**, *771*, L6.5. https://doi.org/10.1557/PROC-771-L6.5.

(16) Su, Y.-W.; Lan, S.-C.; Wei, K.-H. Organic Photovoltaics. *Materials Today* **2012**, *15* (12), 554–562. https://doi.org/10.1016/S1369-7021(13)70013-0.

(17) Kumavat, P. P.; Sonar, P.; Dalal, D. S. An Overview on Basics of Organic and Dye Sensitized Solar Cells, Their Mechanism and Recent Improvements. *Renewable and Sustainable Energy Reviews* **2017**, *78*, 1262–1287. https://doi.org/10.1016/j.rser.2017.05.011.

(18) Tang, C. W.; VanSlyke, S. A. Organic Electroluminescent Diodes. *Appl. Phys. Lett.* **1987**, *51* (12), 913–915. https://doi.org/10.1063/1.98799.

(19) Ingram, G. L.; Lu, Z.-H. Design Principles for Highly Efficient Organic Light-Emitting Diodes. *J. Photon. Energy* **2014**, *4* (1), 040993. https://doi.org/10.1117/1.JPE.4.040993.

(20) Thejo Kalyani, N.; Dhoble, S. J. Organic Light Emitting Diodes: Energy Saving Lighting Technology—A Review. *Renewable and Sustainable Energy Reviews* **2012**, *16* (5), 2696–2723. https://doi.org/10.1016/j.rser.2012.02.021.

(21) Sanvito, S. Molecular Spintronics. *Chem. Soc. Rev.* **2011**, *40* (6), 3336. https://doi.org/10.1039/c1cs15047b.

(22) Wolf, S. A. Spintronics: A Spin-Based Electronics Vision for the Future. *Science* **2001**, *294* (5546), 1488–1495. https://doi.org/10.1126/science.1065389.

(23) Blanchard-Desce, M.; Alain, V.; Bedworth, P. V.; Marder, S. R.; Fort, A.; Runser, C.; Barzoukas, M.; Lebus, S.; Wortmann, R. Large Quadratic Hyperpolarizabilities with Donor–Acceptor Polyenes Exhibiting Optimum Bond Length Alternation: Correlation Between Structure and Hyperpolarizability. *Chem. Eur. J.* **1997**, *3* (7), 1091–1104. https://doi.org/10.1002/chem.19970030717.

(24) de la Torre, G.; Vázquez, P.; Agulló-López, F.; Torres, T. Role of Structural Factors in the Nonlinear Optical Properties of Phthalocyanines and Related Compounds. *Chem. Rev.* **2004**, *104* (9), 3723–3750. https://doi.org/10.1021/cr030206t.

(25) Ray, P. C. Size and Shape Dependent Second Order Nonlinear Optical Properties of Nanomaterials and Their Application in Biological and Chemical Sensing. *Chem. Rev.* **2010**, *110* (9), 5332–5365. https://doi.org/10.1021/cr900335q.

(26) Pierson, H. O.; Pierson, H. O. *Handbook of Chemical Vapor Deposition*, 2nd ed.; Noyes Publications: Norwich, NY, 1999.

(27) Wang, C.; Zhang, H.; Wang, T. H.; Ciszek, T. F. A Continuous Czochralski Silicon Crystal Growth System. *Journal of Crystal Growth* **2003**, *250* (1–2), 209–214. https://doi.org/10.1016/S0022-0248(02)02241-8.

(28) Diao, Y.; Shaw, L.; Bao, Z.; Mannsfeld, S. C. B. Morphology Control Strategies for Solution-Processed Organic Semiconductor Thin Films. *Energy Environ. Sci.* **2014**, *7* (7), 2145–2159. https://doi.org/10.1039/C4EE00688G.

(29) Zheng, Z.; Yim, K.-H.; Saifullah, M. S. M.; Welland, M. E.; Friend, R. H.; Kim, J.-S.; Huck, W. T. S. Uniaxial Alignment of Liquid-Crystalline Conjugated Polymers by Nanoconfinement. *Nano Lett.* **2007**, *7* (4), 987–992. https://doi.org/10.1021/nl070022k.

(30) Kim, S.-S.; Na, S.-I.; Kang, S.-J.; Kim, D.-Y. Annealing-Free Fabrication of P3HT:PCBM Solar Cells via Simple Brush Painting. *Solar Energy Materials and Solar Cells* **2010**, *94* (2), 171–175. https://doi.org/10.1016/j.solmat.2009.08.017.

(31) Cavallini, M.; Stoliar, P.; Moulin, J.-F.; Surin, M.; Leclere, P.; Lazzaroni, R.; Breiby, D. W.; Andreasen, J. W.; Nielsen, M. M.; Sonar, P.; Grimsdale, A. C.; Mu, K. Field-Effect Transistors Based on Self-Organized Molecular Nanostripes. *Nano Lett.* **2005**, *5* (12), 4.

(32) Chen, C.-Y.; Chang, H.-W.; Chang, Y.-F.; Chang, B.-J.; Lin, Y.-S.; Jian, P.-S.; Yeh, H.-C.; Chien, H.-T.; Chen, E.-C.; Chao, Y.-C.; Meng, H.-F.; Zan, H.-W.; Lin, H.-W.; Horng, S.-F.; Cheng, Y.-J.; Yen, F.-W.; Lin, I.-F.; Yang, H.-Y.; Huang, K.-J.; Tseng, M.-R. Continuous Blade Coating for Multi-Layer Large-Area Organic Light-Emitting Diode and Solar Cell. *Journal of Applied Physics* **2011**, *110* (9), 094501. https://doi.org/10.1063/1.3636398.

(33) Rogowski, R. Z.; Dzwilewski, A.; Kemerink, M.; Darhuber, A. A. Solution Processing of Semiconducting Organic Molecules for Tailored Charge Transport Properties. *J. Phys. Chem. C* **2011**, *115* (23), 11758–11762. https://doi.org/10.1021/jp201219h.

(34) Sirringhaus, H.; Kawase, T.; Friend, R. H.; Shimoda, T.; Inbasekaran, M.; Wu, W.; Woo, E. P. High-Resolution Inkjet Printing of All-Polymer Transistor Circuits. *Science* **2000**, *290* (5499), 2123–2126. https://doi.org/10.1126/science.290.5499.2123.

(35) Kasha, M.; Rawls, H. R.; Ashraf El-Bayoumi, M. The Exciton Model in Molecular Spectroscopy. *Pure and Applied Chemistry* **1965**, *11* (3–4). https://doi.org/10.1351/pac196511030371.

(36) McRae, E. G.; Kasha, M. Enhancement of Phosphorescence Ability upon Aggregation of Dye Molecules. *The Journal of Chemical Physics* **1958**, *28* (4), 721–722. https://doi.org/10.1063/1.1744225.

(37) Kasha, M. Energy Transfer Mechanisms and the Molecular Exciton Model for Molecular Aggregates. *Radiation Research* **1963**, *20* (1), 55. https://doi.org/10.2307/3571331.

(38) Kasha, M. Characterization of Electronic Transitions in Complex Molecules. *Discuss. Faraday Soc.* **1950**, *9*, 14. https://doi.org/10.1039/df9500900014.

(39) Philpott, M. R. Theory of the Coupling of Electronic and Vibrational Excitations in Molecular Crystals and Helical Polymers. *The Journal of Chemical Physics* **1971**, *55* (5), 2039–2054. https://doi.org/10.1063/1.1676371.

(40) Fulton, R. L.; Gouterman, M. Vibronic Coupling. I. Mathematical Treatment for Two Electronic States. *The Journal of Chemical Physics* **1961**, *35* (3), 1059–1071. https://doi.org/10.1063/1.1701181.

(41) Spano, F. C. The Spectral Signatures of Frenkel Polarons in H- and J-Aggregates. *Accounts of Chemical Research* **2010**, *43* (3), 429–439. https://doi.org/10.1021/ar900233v.

(42) Merrifield, R. E. Ionized States in a One-Dimensional Molecular Crystal. *The Journal of Chemical Physics* **1961**, *34* (5), 1835–1839. https://doi.org/10.1063/1.1701086.

(43) Hernandez, J. P.; Choi, S. Optical Absorption by Charge-Transfer Excitons in Linear Molecular Crystals. *The Journal of Chemical Physics* **1969**, *50* (4), 1524–1532. https://doi.org/10.1063/1.1671237.

(44) Hennessy, M. H.; Pascal, R. A.; Soos, Z. G. Vibronic Structure of Frenkel and Charge-Transfer Excitons in PTCDA. *Molecular Crystals and Liquid Crystals Science and Technology. Section A. Molecular Crystals and Liquid Crystals* **2001**, *355* (1), 41–63. https://doi.org/10.1080/10587250108023653.

(45) Gisslén, L.; Scholz, R. Crystallochromy of Perylene Pigments: Interference between Frenkel Excitons and Charge-Transfer States. *Phys. Rev. B* **2009**, *80* (11), 115309. https://doi.org/10.1103/PhysRevB.80.115309.

(46) Yamagata, H.; Maxwell, D. S.; Fan, J.; Kittilstved, K. R.; Briseno, A. L.; Barnes, M. D.; Spano, F. C. HJ-Aggregate Behavior of Crystalline 7,8,15,16-Tetraazaterrylene: Introducing a New Design Paradigm for Organic Materials. *J. Phys. Chem. C* **2014**, *118* (49), 28842–28854. https://doi.org/10.1021/jp509011u.

(47) Yamagata, H.; Spano, F. C. Interplay between Intrachain and Interchain Interactions in Semiconducting Polymer Assemblies: The HJ-Aggregate Model. *The Journal of Chemical Physics* **2012**, *136* (18), 184901. https://doi.org/10.1063/1.4705272.

(48) Pichler, K.; Halliday, D. A.; Bradley, D. D. C.; Burn, P. L.; Friend, R. H.; Holmes, A. B. Optical Spectroscopy of Highly Ordered Poly(p-Phenylene Vinylene). *J. Phys.: Condens. Matter* **1993**, *5* (38), 7155–7172. https://doi.org/10.1088/0953-8984/5/38/011.

(49) Oatley, C. W.; Nixon, W. C.; Pease, R. F. W. Scanning Electron Microscopy. In *Advances in Electronics and Electron Physics*; Elsevier, 1966; Vol. 21, pp 181–247. https://doi.org/10.1016/S0065-2539(08)61010-0.

(50) Wang, Z. L. Transmission Electron Microscopy of Shape-Controlled Nanocrystals and Their Assemblies. *J. Phys. Chem. B* **2000**, *104* (6), 1153–1175. https://doi.org/10.1021/jp993593c.

(51) Harazi, S.; Kapon, O.; Sharoni, A.; Tischler, Y. R. Direct Formation of Carbocyanine J-Aggregates in Organic Solvent. *J. Phys. Chem. C* **2019**, 7.

(52) Friedl, C.; Renger, T. Structure Prediction of Self-Assembled Dye Aggregates from Cryogenic Transmission Electron Microscopy, Molecular Mechanics, and Theory of Optical Spectra. *J. Phys. Chem. C* **2016**, 18.

(53) Chen, C.-Y.; Sano, T.; Tsuda, T.; Ui, K.; Oshima, Y.; Yamagata, M.; Ishikawa, M.; Haruta, M.; Doi, T.; Inaba, M.; Kuwabata, S. In Situ Scanning Electron Microscopy of Silicon Anode Reactions in Lithium-Ion Batteries during Charge/Discharge Processes. *Sci Rep* **2016**, *6* (1), 36153. https://doi.org/10.1038/srep36153.

(54) Taheri, M. L.; Stach, E. A.; Arslan, I.; Crozier, P. A.; Kabius, B. C.; LaGrange, T.; Minor, A. M.; Takeda, S.; Tanase, M.; Wagner, J. B.; Sharma, R. Current Status and Future Directions for in Situ Transmission Electron Microscopy. *Ultramicroscopy* **2016**, *170*, 86–95. https://doi.org/10.1016/j.ultramic.2016.08.007.

(55) Ramachandramoorthy, R.; Bernal, R.; Espinosa, H. D. Pushing the Envelope of *In Situ* Transmission Electron Microscopy. *ACS Nano* **2015**, *9* (5), 4675–4685. https://doi.org/10.1021/acsnano.5b01391.

(56) Bottomley, L. A. Scanning Probe Microscopy. *Anal. Chem.* **1998**, *70* (12), 425–476. https://doi.org/10.1021/a1980011o.

(57) Kline, R. J.; McGehee, M. D.; Kadnikova, E. N.; Liu, J.; Fréchet, J. M. J.; Toney, M. F. Dependence of Regioregular Poly(3-Hexylthiophene) Film Morphology and Field-Effect Mobility on Molecular Weight. *Macromolecules* **2005**, *38* (8), 3312–3319. https://doi.org/10.1021/ma047415f.

(58) Korolkov, V. V.; Summerfield, A.; Murphy, A.; Amabilino, D. B.; Watanabe, K.; Taniguchi, T.; Beton, P. H. Ultra-High Resolution Imaging of Thin Films and Single Strands of Polythiophene Using Atomic Force Microscopy. *Nat Commun* **2019**, *10* (1), 1537. https://doi.org/10.1038/s41467-019-09571-6.

(59) Widjonarko, N. Introduction to Advanced X-Ray Diffraction Techniques for Polymeric Thin Films. *Coatings* **2016**, *6* (4), 54. https://doi.org/10.3390/coatings6040054.

(60) Rivnay, J.; Noriega, R.; Kline, R. J.; Salleo, A.; Toney, M. F. Quantitative Analysis of Lattice Disorder and Crystallite Size in Organic Semiconductor Thin Films. *Phys. Rev. B* **2011**, *84* (4), 045203. https://doi.org/10.1103/PhysRevB.84.045203.

(61) Renaud, G.; Lazzari, R.; Leroy, F. Probing Surface and Interface Morphology with Grazing Incidence Small Angle X-Ray Scattering. *Surface Science Reports* **2009**, *64* (8), 255–380. https://doi.org/10.1016/j.surfrep.2009.07.002.

(62) Tang, C.; Tracz, A.; Kruk, M.; Zhang, R.; Smilgies, D.-M.; Matyjaszewski, K.; Kowalewski, T. Long-Range Ordered Thin Films of Block Copolymers Prepared by Zone-Casting and Their Thermal Conversion into Ordered Nanostructured Carbon. *J. Am. Chem. Soc.* **2005**, *127* (19), 6918–6919. https://doi.org/10.1021/ja0508929.

(63) Manley, E. F.; Strzalka, J.; Fauvell, T. J.; Jackson, N. E.; Leonardi, M. J.; Eastham, N. D.; Marks, T. J.; Chen, L. X. In Situ GIWAXS Analysis of Solvent and Additive Effects on PTB7 Thin Film Microstructure Evolution during Spin Coating. *Adv. Mater.* **2017**, *29* (43), 1703933. https://doi.org/10.1002/adma.201703933.

(64) Czajka, A.; Armes, S. P. *In Situ* SAXS Studies of a Prototypical RAFT Aqueous Dispersion Polymerization Formulation: Monitoring the Evolution in Copolymer Morphology during Polymerization-Induced Self-Assembly. *Chem. Sci.* **2020**, *11* (42), 11443–11454. https://doi.org/10.1039/D0SC03411H.

(65) Niu, M.; Zheng, F.; Yang, X.; Bi, P.; Feng, L.; Hao, X. Molecular Packing Correlated Fluorescence in TIPS-Pentacene Films. *Organic Electronics* **2017**, *49*, 340–346. https://doi.org/10.1016/j.orgel.2017.07.007.

(66) Furube, A.; Murai, M.; Tamaki, Y.; Watanabe, S.; Katoh, R. Effect of Aggregation on the Excited-State Electronic Structure of Perylene Studied by Transient Absorption Spectroscopy. *J. Phys. Chem. A* **2006**, *110* (20), 6465–6471. https://doi.org/10.1021/jp060649b.

(67) Son, M.; Park, K. H.; Shao, C.; Würthner, F.; Kim, D. Spectroscopic Demonstration of Exciton Dynamics and Excimer Formation in a Sterically Controlled Perylene Bisimide Dimer Aggregate. *J. Phys. Chem. Lett.* **2014**, *5* (20), 3601–3607. https://doi.org/10.1021/jz501953a.

(68) Wilson, K. S.; Wong, C. Y. In Situ Measurement of Exciton Dynamics During Thin-Film Formation Using Single-Shot Transient Absorption. *J. Phys. Chem. A* **2018**, *122* (31), 6438–6444. https://doi.org/10.1021/acs.jpca.8b06248.

(69) Haverkort, F.; Stradomska, A.; Knoester, J. First-Principles Simulations of the Initial Phase of Self-Aggregation of a Cyanine Dye: Structure and Optical Spectra. *J. Phys. Chem. B* **2014**, *118* (29), 8877–8890. https://doi.org/10.1021/jp5049277.

(70) Yap, J. H.; To, T. T.; Adams, S. Monte Carlo Morphological Modelling of a P3HT:PCBM Bulk Heterojunction Organic Solar Cell. *J. Polym. Sci. Part B: Polym. Phys.* **2015**, *53* (4), 270–279. https://doi.org/10.1002/polb.23627.

(71) Mima, T.; Kinjo, T.; Yamakawa, S.; Asahi, R. Study of the Conformation of Polyelectrolyte Aggregates Using Coarse-Grained Molecular Dynamics Simulations. *Soft Matter* **2017**, *13* (35), 5991–5999. https://doi.org/10.1039/C7SM01196B.

(72) Holstein, T. Studies of Polaron Motion. *Annals of Physics* **1959**, *8* (3), 325–342. https://doi.org/10.1016/0003-4916(59)90002-8.

(73) Fulton, R. L.; Gouterman, M. Vibronic Coupling. II. Spectra of Dimers. *The Journal of Chemical Physics* **1964**, *41* (8), 2280–2286. https://doi.org/10.1063/1.1726260.

(74) Merrifield, R. E. Vibronic States of Dimers. *Radiation Research* **1963**, *20* (1), 154. https://doi.org/10.2307/3571343.

(75) Merrifield, R. E. Theory of the Vibrational Structure of Molecular Exciton States. *The Journal of Chemical Physics* **1964**, *40* (2), 445–450. https://doi.org/10.1063/1.1725135.

(76) Scherer, P. O. J.; Fischer, S. F. On the Theory of Vibronic Structure of Linear Aggregates. Application to Pseudoisocyanin (PIC). *Chemical Physics* **1984**, *86* (3), 269–283. https://doi.org/10.1016/0301-0104(84)80015-4.

(77) Hoffmann, M.; Soos, Z. G. Optical Absorption Spectra of the Holstein Molecular Crystal for Weak and Intermediate Electronic Coupling. *Phys. Rev. B* **2002**, *66* (2), 024305. https://doi.org/10.1103/PhysRevB.66.024305.

(78) Pochas, C. M.; Kistler, K. A.; Yamagata, H.; Matsika, S.; Spano, F. C. Contrasting Photophysical Properties of Star-Shaped vs Linear Perylene Diimide Complexes. *J. Am. Chem. Soc.* **2013**, *135* (8), 3056–3066. https://doi.org/10.1021/ja3087449.

(79) Oleson, A.; Zhu, T.; Dunn, I. S.; Bialas, D.; Bai, Y.; Zhang, W.; Dai, M.; Reichman, D. R.; Tempelaar, R.; Huang, L.; Spano, F. C. Perylene Diimide-Based Hj- and HJ-Aggregates: The Prospect of Exciton Band Shape Engineering in Organic Materials. *J. Phys. Chem. C* **2019**, *123* (33), 20567–20578. https://doi.org/10.1021/acs.jpcc.9b04429.

(80) Pochas, C. M.; Spano, F. C. New Insights on the Nature of Two-Dimensional Polarons in Semiconducting Polymers: Infrared Absorption in Poly(3-Hexylthiophene). *The Journal of Chemical Physics* **2014**, *140* (24), 244902. https://doi.org/10.1063/1.4882696.

(81) Spano, F. C. Absorption and Emission in Oligo-Phenylene Vinylene Nanoaggregates: The Role of Disorder and Structural Defects. *The Journal of Chemical Physics* **2002**, *116* (13), 5877–5891. https://doi.org/10.1063/1.1446034.

(82) Spano, F. C. The Fundamental Photophysics of Conjugated Oligomer Herringbone Aggregates. *The Journal of Chemical Physics* **2003**, *118* (2), 981–994. https://doi.org/10.1063/1.1521933.

(83) Iwase, M.; Suzuki, A.; Akiyama, T.; Oku, T. Fabrication and Characterization of Phthalocyanine-Based Organic Solar Cells. *MSA* **2014**, *05* (05), 278–284. https://doi.org/10.4236/msa.2014.55033.

(84) Ma, L.; Zhang, K.; Kloc, C.; Sun, H.; Michel-Beyerle, M. E.; Gurzadyan, G. G. Singlet Fission in Rubrene Single Crystal: Direct Observation by Femtosecond Pump–Probe Spectroscopy. *Phys. Chem. Chem. Phys.* **2012**, *14* (23), 8307. https://doi.org/10.1039/c2cp40449d.

(85) Gierschner, J.; Park, S. Y. Luminescent Distyrylbenzenes: Tailoring Molecular Structure and Crystalline Morphology. *J. Mater. Chem. C* **2013**, *1* (37), 5818. https://doi.org/10.1039/c3tc31062k.

(86) Ostroverkhova, O.; Shcherbyna, S.; Cooke, D. G.; Egerton, R. F.; Hegmann, F. A.; Tykwinski, R. R.; Parkin, S. R.; Anthony, J. E. Optical and Transient Photoconductive Properties of Pentacene and Functionalized Pentacene Thin Films: Dependence on Film Morphology. *Journal of Applied Physics* **2005**, *98* (3), 033701. https://doi.org/10.1063/1.1949711.

(87) Wilson, T. M.; Tauber, M. J.; Wasielewski, M. R. Toward an N-Type Molecular Wire: Electron Hopping within Linearly Linked Perylenediimide Oligomers. *J. Am. Chem. Soc.* **2009**, *131* (25), 8952–8957. https://doi.org/10.1021/ja902258g.

(88) Margulies, E. A.; Shoer, L. E.; Eaton, S. W.; Wasielewski, M. R. Excimer Formation in Cofacial and Slip-Stacked Perylene-3,4:9,10-Bis(Dicarboximide) Dimers on a Redox-Inactive Triptycene Scaffold. *Phys. Chem. Chem. Phys.* **2014**, *16* (43), 23735–23742. https://doi.org/10.1039/C4CP03107E.

(89) Myong, M. S.; Zhou, J.; Young, R. M.; Wasielewski, M. R. Charge-Transfer Character in Excimers of Perylenediimides Self-Assembled on Anodic Aluminum Oxide Membrane Walls. *J. Phys. Chem. C* **2020**, *124* (8), 4369–4377. https://doi.org/10.1021/acs.jpcc.9b10805.

(90) *Advanced Fluorescence Reporters in Chemistry and Biology I: Fundamentals and Molecular Design*; Demchenko, A. P., Callis, P. R., Eds.; Springer series on fluorescence; Springer: Heidelberg ; New York, 2010.

(91) Eachus, R. S.; Marchetti, A. P.; Muenter, A. A. The Photophysics of Silver Halide Imaging Materials. *Annu. Rev. Phys. Chem.* **1999**, *50* (1), 117–144. https://doi.org/10.1146/annurev.physchem.50.1.117.

(92) Carreon, J. R.; Stewart, K. M.; Mahon, K. P.; Shin, S.; Kelley, S. O. Cyanine Dye Conjugates as Probes for Live Cell Imaging. *Bioorganic & Medicinal Chemistry Letters* **2007**, *17* (18), 5182–5185. https://doi.org/10.1016/j.bmcl.2007.06.097.

(93) Funabiki, K.; Mase, H.; Hibino, A.; Tanaka, N.; Mizuhata, N.; Sakuragi, Y.; Nakashima, A.; Yoshida, T.; Kubota, Y.; Matsui, M. Synthesis of a Novel Heptamethine–Cyanine Dye for Use in near-Infrared Active Dye-Sensitized Solar Cells with Porous Zinc Oxide Prepared at Low Temperature. *Energy Environ. Sci.* **2011**, *4* (6), 2186. https://doi.org/10.1039/c1ee01141c.

(94) Dempsey, G. T.; Bates, M.; Kowtoniuk, W. E.; Liu, D. R.; Tsien, R. Y.; Zhuang, X. Photoswitching Mechanism of Cyanine Dyes. *J. Am. Chem. Soc.* **2009**, *131* (51), 18192–18193. https://doi.org/10.1021/ja904588g.

(95) von Berlepsch, H.; Kirstein, S.; Böttcher, C. Supramolecular Structure of J-Aggregates of a Sulfonate Substituted Amphiphilic Carbocyanine Dye in Solution: Methanol-Induced Ribbon-to-Tubule Transformation. *J. Phys. Chem. B* **2004**, *108* (48), 18725–18733. https://doi.org/10.1021/jp046546f.

(96) v. Berlepsch, H.; Böttcher, C. Supramolecular Structure of TTBC J-Aggregates in Solution and on Surface. *Langmuir* **2013**, *29* (16), 4948–4958. https://doi.org/10.1021/la400417d.

(97) Clark, K. A.; Krueger, E. L.; Vanden Bout, D. A. Direct Measurement of Energy Migration in Supramolecular Carbocyanine Dye Nanotubes. *J. Phys. Chem. Lett.* **2014**, *5* (13), 2274–2282. https://doi.org/10.1021/jz500634f.

(98) Birkan, B.; Gülen, D.; Özçelik, S. Controlled Formation of the Two-Dimensional TTBC J-Aggregates in an Aqueous Solution. *J. Phys. Chem. B* **2006**, *110* (22), 10805–10813. https://doi.org/10.1021/jp0573846.

(99) Walker, B. J.; Bulović, V.; Bawendi, M. G. Quantum Dot/J-Aggregate Blended Films for Light Harvesting and Energy Transfer. *Nano Lett.* **2010**, *10* (10), 3995–3999. https://doi.org/10.1021/nl1018639.

(100) Walker, B. J.; Nair, G. P.; Marshall, L. F.; Bulović, V.; Bawendi, M. G. Narrow-Band Absorption-Enhanced Quantum Dot/J-Aggregate Conjugates. *J. Am. Chem. Soc.* **2009**, *131* (28), 9624–9625. https://doi.org/10.1021/ja902813q.

(101) Jelley, E. E. Spectral Absorption and Fluorescence of Dyes in the Molecular State. *Nature* **1936**, *138* (3502), 1009–1010. https://doi.org/10.1038/1381009a0.

(102) Kopainsky, B.; Hallermeier, J. K.; Kaiser, W. The First Step of Aggregation of PIC: The Dimerization. *Chemical Physics Letters* **1981**, *83* (3), 498–502. https://doi.org/10.1016/0009-2614(81)85509-1.

(103) Kopainsky, B.; Kaiser, W. Ultrafast Transient Processes of Monomers, Dimers, and Aggregates of Pseudoisocyanine Chloride (PIC). *Chemical Physics Letters* **1982**, *88* (4), 357–361. https://doi.org/10.1016/0009-2614(82)83025-X.

(104) Scherer, P. O. J.; Fischer, S. F. On the Theory of Vibronic Structure of Linear Aggregates. Application to Pseudoisocyanin (PIC). *Chemical Physics* **1984**, *86* (3), 269–283. https://doi.org/10.1016/0301-0104(84)80015-4.

(105) von Berlepsch, H.; Böttcher, C.; Dähne, L. Structure of J-Aggregates of Pseudoisocyanine Dye in Aqueous Solution. *J. Phys. Chem. B* **2000**, *104* (37), 8792–8799. https://doi.org/10.1021/jp000085q.

(106) Fidder, H. Absorption and Emission Studies on Pure and Mixed J-Aggregates of Pseudoisocyanine. *Chemical Physics* **2007**, *341* (1–3), 158–168. https://doi.org/10.1016/j.chemphys.2007.06.016.

(107) Haverkort, F.; Stradomska, A.; de Vries, A. H.; Knoester, J. Investigating the Structure of Aggregates of an Amphiphilic Cyanine Dye with Molecular Dynamics Simulations. *J. Phys. Chem. B* **2013**, *117* (19), 5857–5867. https://doi.org/10.1021/jp4005696.

(108) Bricker, W. P.; Banal, J. L.; Stone, M. B.; Bathe, M. Molecular Model of J-Aggregated Pseudoisocyanine Fibers. *The Journal of Chemical Physics* **2018**, *149* (2), 024905. https://doi.org/10.1063/1.5036656.

(109) Ida, T.; Ando, M.; Toraya, H. Extended Pseudo-Voigt Function for Approximating the Voigt Profile. *J Appl Crystallogr* **2000**, *33* (6), 1311–1316. https://doi.org/10.1107/S0021889800010219.

(110) Cina, J. A.; Kiessling, A. J. Nuclear Wave-Packet Dynamics in Two-Dimensional Interferograms of Excitation-Transfer Systems. In *Coherent Multidimensional Spectroscopy*; Cho, M., Ed.; Springer Series in Optical Sciences; Springer Singapore: Singapore, 2019; Vol. 226, pp 51–85. https://doi.org/10.1007/978-981-13-9753-0_3.

(111) Spano, F. C.; Silva, C. H- and J-Aggregate Behavior in Polymeric Semiconductors. *Annu. Rev. Phys. Chem.* **2014**, *65* (1), 477–500. https://doi.org/10.1146/annurev-physchem-040513-103639.

(112) Deshmukh, A. P.; Koppel, D.; Chuang, C.; Cadena, D. M.; Cao, J.; Caram, J. R. Design Principles for Two-Dimensional Molecular Aggregates Using Kasha's Model: Tunable Photophysics in Near and Short-Wave Infrared. *J. Phys. Chem. C* **2019**, *123* (30), 18702–18710. https://doi.org/10.1021/acs.jpcc.9b05060.

(113) Dijkstra, A. G.; Duan, H.-G.; Knoester, J.; Nelson, K. A.; Cao, J. How Two-Dimensional Brick Layer J-Aggregates Differ from Linear Ones: Excitonic Properties and Line Broadening Mechanisms. *The Journal of Chemical Physics* **2016**, *144* (13), 134310. https://doi.org/10.1063/1.4944980.

(114) Spano, F. C. Absorption in Regio-Regular Poly(3-Hexyl)Thiophene Thin FIlms: Fermi Resonances, Interband Coupling and Disorder. *Chemical Physics* **2006**, 14.

(115) Sorokin, A. V.; Pereverzev, N. V.; Grankina, I. I.; Yefimova, S. L.; Malyukin, Y. V. Evidence of Exciton Self-Trapping in Pseudoisocyanine J-Aggregates Formed in Layered Polymer Films. *J. Phys. Chem. C* **2015**, *119* (49), 27865–27873. https://doi.org/10.1021/acs.jpcc.5b09940.

(116) Megow, J.; Körzdörfer, T.; Renger, T.; Sparenberg, M.; Blumstengel, S.; Henneberger, F.; May, V. Calculating Optical Absorption Spectra of Thin Polycrystalline Organic Films: Structural Disorder and Site-Dependent van Der Waals Interaction. *J. Phys. Chem. C* **2015**, *119* (10), 5747–5751. https://doi.org/10.1021/acs.jpcc.5b01587.

(117) Rätsep, M.; Pieper, J.; Irrgang, K.-D.; Freiberg, A. Excitation Wavelength-Dependent Electron−Phonon and Electron−Vibrational Coupling in the CP29 Antenna Complex of Green Plants. *J. Phys. Chem. B* **2008**, *112* (1), 110–118. https://doi.org/10.1021/jp075170d.

(118) Skandary, S.; Hussels, M.; Konrad, A.; Renger, T.; Müh, F.; Bommer, M.; Zouni, A.; Meixner, A. J.; Brecht, M. Variation of Exciton-Vibrational Coupling in Photosystem II Core Complexes from *Thermosynechococcus Elongatus* As Revealed by Single-Molecule Spectroscopy. *J. Phys. Chem. B* **2015**, *119* (11), 4203–4210. https://doi.org/10.1021/jp510631x.

(119) Lee, M. K.; Huo, P.; Coker, D. F. Semiclassical Path Integral Dynamics: Photosynthetic Energy Transfer with Realistic Environment Interactions. *Annu. Rev. Phys. Chem.* **2016**, *67* (1), 639–668. https://doi.org/10.1146/annurev-physchem-040215-112252.

(120) Lin, C.; Renge, I.; Jankowiak, R. Fluorescence Line-Narrowing Difference Spectra: Dependence of Huang–Rhys Factor on Excitation Wavelength. *Chemical Physics Letters* **2013**, *576*, 15–20. https://doi.org/10.1016/j.cplett.2013.05.017.

(121) Hu, Y.; Wang, C.-W.; Zhu, C.; Gu, F.; Lin, S.-H. Franck–Condon Simulation for Unraveling Vibronic Origin in Solvent Enhanced Absorption and Fluorescence Spectra of Rubrene. *RSC Adv.* **2017**, *7* (20), 12407–12418. https://doi.org/10.1039/C7RA00417F.

(122) Smilgies, D.-M.; Li, R.; Giri, G.; Chou, K. W.; Diao, Y.; Bao, Z.; Amassian, A. Look Fast: Crystallization of Conjugated Molecules during Solution Shearing Probed *in-Situ* and in Real Time by X-Ray Scattering. *Phys. Status Solidi RRL* **2013**, *7* (3), 177–179. https://doi.org/10.1002/pssr.201206507.

(123) Wan, J.; Li, Y.; Ulbrandt, J. G.; Smilgies, D.-M.; Hollin, J.; Whalley, A. C.; Headrick, R. L. Transient Phases during Fast Crystallization of Organic Thin Films from Solution. *APL Materials* **2016**, *4* (1), 016103. https://doi.org/10.1063/1.4939464.

(124) Yang, J.; Zhou, W.; Wang, F.; Deng, K.; Yi, T.; Shen, L.; Fang, Y.; Yang, Y.; Song, Y. Single-Shot Pump-Probe Technique Using Mirror Array. *Appl. Phys. B* **2020**, *126* (5), 98. https://doi.org/10.1007/s00340-020-07446-z.

(125) Wilson, K. S.; Wong, C. Y. In Situ Measurement of Exciton Dynamics During Thin-Film Formation Using Single-Shot Transient Absorption. *J. Phys. Chem. A* **2018**, *122* (31), 6438–6444. https://doi.org/10.1021/acs.jpca.8b06248.

(126) Kobayashi, M.; Minami, Y.; Johnson, C. L.; Salmans, P. D.; Ellsworth, N. R.; Takeda, J.; Johnson, J. A.; Katayama, I. High-Acquisition-Rate Single-Shot Pump-Probe Measurements Using Time-Stretching Method. *Scientific Reports* **2016**, *6*, 37614. https://doi.org/10.1038/srep37614.

(127) Fourkas, J. T.; Dhar, L.; Nelson, K. A.; Trebino, R. Spatially Encoded, Single-Shot Ultrafast Spectroscopies. *J. Opt. Soc. Am. B* **1995**, *12* (1), 155. https://doi.org/10.1364/JOSAB.12.000155.